Software Development for the Analysis of Exotic Beam Experiments and Study of the Neutron-Deficient Nuclei ^{98}Cd and ^{98}Ag

Inaugural-Dissertation
zur
Erlangung des Doktorgrades
der Mathematisch-Naturwissenschaftlichen Fakultät
der Universität zu Köln

vorgelegt von
Norbert Braun
aus Berlin

Köln 2013

Berichterstatter:	Prof. Dr. J. Jolie Prof. Dr. P. Reiter
Tag der mündlichen Prüfung:	14.12.2012

All science is either physics or stamp collecting.

— Ernest Rutherford

Abstract

In this thesis, results of an experiment to study exotic nuclei in the ^{100}Sn region are presented. ^{100}Sn is the heaviest doubly-magic, self-conjugate nucleus. The nucleus and its neighbourhood are an important testing ground for the nuclear shell model, giving input on topics such as the single particle structure or the $\pi\nu$ residual interaction. In addition, as the rapid proton capture (rp) process involves nuclei in the region, it is of interest for nuclear astrophysics.

Recently, modern exotic beam facilities have made it possible to study nuclei very far from stability, such as the region around ^{100}Sn. Thus, the questions from above can finally be addressed experimentally, and the evolution of nuclear structure can be tracked over a much larger region than previously possible.

The experimental work for this thesis was performed at the FRS (FRagment Separator) instrument at GSI Helmholtzzentrum für Schwerionenforschung in Darmstadt, Germany. Exotic nuclei were produced by fragmentation of an 850 MeV/u ^{128}Xe beam on a ^{9}Be target. After being separated in the fragment separator they were brought to rest in an active stopper. The RISING high-purity germanium array with 15 EUROBALL cluster detectors was used to record γ rays and $\gamma\gamma$ coincidences emitted by isomeric states in the fragmentation products and daughter nuclei from their subsequent β decay. For the daughter nuclei, the active stopper allowed identification via implantation-decay correlation.

I present results for ^{98}Cd and ^{98}Ag. In ^{98}Cd, a previously unknown excited state with an energy slightly below the known (12^+) state was discovered, and assigned a tentative spin/parity of (10^+). Previous theoretical calculations had predicted this state to lie above the (12^+) state. Tentative explanations hint at either a reversal of the neutron $\nu d_{5/2}$ and the $\nu g_{7/2}$ single particle orbitals, or an increased proton strength.

In ^{98}Ag, evidence for a reversed ordering of the transitions from the two lowest-lying excited states was found. This would change energy and tentative spin assignment for the first (lowest-lying) excited state. In addition, the lifetime of the first excited state was determined. In both cases, reproducing the new results by theoretical calculations yields new insights into nuclear structure in this region.

Zusammenfassung

In dieser Arbeit werden Ergebnisse eines Experiments aus der Region um ^{100}Sn vorgestellt. ^{100}Sn ist der schwerste, doppelt-magische Kern mit gleicher Protonen- und Neutronenzahl. Der Kern und die umliegende Massenregion sind ein wichtiges Testgebiet für Theorierechnungen im Rahmen des Schalenmodells, z. B. für die Einteilchenstruktur oder die $\pi\nu$ Restwechselwirkung. Ferner involviert der *rapid proton* (rp) Prozess Kerne in dieser Region, weswegen sie auch für die nukleare Astrophysik von Interesse sind.

In jüngerer Vergangenheit haben moderne Forschungseinrichtungen zum Studium exotischer Strahlen es möglich gemacht, auch Kerne weit abseits des Tals der Stabilität zu untersuchen, beispielsweise die Region um ^{100}Sn. Dadurch können die oben aufgeworfenen Fragen experimentell behandelt werden und die Evolution der Kernstruktur kann über eine viel größere Region verfolgt werden, als es bisher möglich war.

Das Experiment wurde am FRS (FRagment Separator) Aufbau am GSI Helmholtzzentrum für Schwerionenforschung in Darmstadt durchgeführt. Die exotischen Kerne wurden durch Fragmentierung eines 850 MeV/u ^{128}Xe-Strahls an einem ^{9}Be-Target erzeugt. Nach der Trennung im Fragmentseparator wurden sie in einem aktiven Stopper gestoppt. Mit Hilfe des RISING-Germaniumspektrometers wurden γ-Strahlung und $\gamma\gamma$-Koinzidenzen aufgezeichnet, die von isomeren Zuständen in den Fragmentierungsprodukten und deren Tochterkernen ausgesandt wurden. Im Falle der Tochterkerne wurde eine Identifizierung durch Implantierungs-Zerfalls-Korrelation mittels des aktiven Stoppers ermöglicht.

Ich stelle Ergebnisse für die Kerne ^{98}Cd und ^{98}Ag vor. In ^{98}Cd wurde ein bisher unbekannter Zustand mit einer Energie knapp unterhalb des bekannten (12^+)-Zustands entdeckt. Diesem Zustand wird eine vorläufiger Spin/Parität von (10^+) zugewiesen. Theorierechnungen, die vor dem Experiment durchgeführt wurden, haben den (10^+)-Zustand knapp oberhalb des (12^+)-Zustands vorhergesagt. Die experimentellen Ergebnisse können durch eine Vertauschung der Neutronen- $\nu d_{5/2}$ und $\nu g_{7/2}$ Einteilchen-Orbitale oder durch eine erhöhte Stärke der Protonenwechselwirkung erklärbar sein.

In ^{98}Ag wurden Hinweise auf eine vertauschte Reihenfolge der Übergänge von den zwei niedrigstliegenden angeregten Zuständen gefunden. Dadurch würden sich Energie und vermutlicher Spin/Parität des ersten (niedrigstliegenden) angeregten Zustands ändern. Außerdem wurde die Lebensdauer des ersten angeregten Zustands bestimmt. In beiden Fällen liefert die Reproduktion der experimentellen Ergebnisse in Theorierechnungen neue Einsichten in die Kernstruktur dieser Gegend.

Contents

1 Introduction

In recent years, the study of highly exotic nuclei has become a major focus of nuclear physics. By "highly exotic" we mean nuclei that are so far off the valley of stability that they cannot be produced in low-energy nuclear reactions with stable nuclei. There are two major techniques to produce them: fragment separation, as used in the experiment described in this thesis, and on-line isotope mass separation.

Studies on exotic nuclei are being carried out in a number of facilities around the world, including CERN in Switzerland/France, ILL in France, RIKEN in Japan and the NSCL in the United States. The experiment described in this thesis took place at the GSI Helmholtzzentrum für Schwerionenforschung in Darmstadt, Germany, using the FRS (FRagment Separator) instrument. Furthermore, upgraded facilities will become available in the future. An example is the SuperFRS instrument under construction at GSI as a part of FAIR.

One question that drives the study of these nuclei is the evolution of the nuclear shell structure. In the nuclear shell model, there are "magic" numbers of protons and neutrons, roughly analogous to the noble gases in the electronic theory of the atom. The magic numbers manifest themselves as gaps in the single particle energies.

In this thesis, an experiment to study nuclei close to ^{100}Sn is described. ^{100}Sn is the heaviest nucleus that is both doubly-magic (i.e. has a magic number of protons and a magic number of neutrons) and self-conjugate (i.e. it has the same number of protons and neutrons). To understand nuclear structure in the ^{100}Sn region, it is of interest to investigate the neighbouring nuclei, as the nuclear shell model describes them as a ^{100}Sn core with additional nucleons or nucleon holes.

An additional motivation to study these highly exotic nuclei comes from the fact that they are involved in the rapid proton capture scenario of nucleosynthesis. Given that present-day theories of nuclear structure are still largely phenomenological in nature, ad-hoc predictions of nuclear properties far from experimentally explored areas are virtually impossible. Therefore, to advance our understanding of nucleosynthesis, experimental access to the regions of the nuclear chart involved in these scenarios is necessary.

^{100}Sn and the neighbouring nuclei have been subject of a large research effort in the past (see, for example, [1], and many others).

In this experiment, several exotic nuclei in the region around ^{100}Sn were studied. Given the size of this effort, the experiment was done in a large collaboration. For this thesis work, I analyzed data pertaining to the nuclei ^{98}Cd and ^{98}Ag.

The rest of this text is organized as follows:

- **Chapter 2** discusses the experimental setup (accelerators and detectors) in more detail. The detectors used can be divided into three major groups: FRS detectors (particle identification), HPGe detectors (γ-ray spectroscopy) and silicon detectors (active stopper, decay product spectroscopy).
- **Chapter 3** reviews the various steps needed to reduce the raw data to experimental results. The chapter presents the R2D2 analysis software in more detail and discusses the steps needed to calibrate the HPGe and silicon detectors.
- **Chapter 4** presents the experimental results on ^{98}Cd and ^{98}Ag.
- **Chapter 5** compares the experimental results to theory. The nuclear shell model is introduced and two possible explanations for the results on ^{98}Cd are discussed. In addition, first shell model results on ^{98}Ag are shown.

2 Experimental setup

2.1 Introduction

As mentioned in the general introduction, there are two major techniques for producing exotic nuclei. The first one is on-line isotope mass separation, of which the ISOLDE facility at CERN is a major example. At ISOLDE, a beam of protons is accelerated to an energy of the order of 1 GeV and impacted on a uranium target. Inside the target, spallation, fission, and fragmentation reactions produce a wide range of exotic nuclei, which end up at rest. They are removed from the target by thermal diffusion at high temperatures (above 1000°C) and fed into a mass separator, where again the isotope of interest is selected for further study. It is possible to re-accelerate the exotic nuclei to study them in nuclear reactions, using the post-accelerator REX. It is not essential to use a proton beam; other ISOL facilities have used heavy ions. As the ISOL technique did not play any role for this thesis, it will not be described in further detail.

For this work, the fragment separation technique was used. In this method, a beam of stable, heavy nuclei is accelerated to high energies (hundreds of MeV per nucleon for our experiment) and impacted on a fragmentation target consisting of light nuclei. In the fragmentation target, the heavy nuclei split up into a cocktail of fragmentation products with a wide range of possible proton and neutron numbers. These fragmentation products are still travelling at a large fraction of their original speed. They are then sorted by their deflection in magnetic fields and studied.

The experiment took place at the FRS fragment separator at GSI (*Gesellschaft für Schwerionenforschung*). A primary beam of ^{128} Xe was accelerated to an energy of 850 MeV per nucleon and then fragmented on a ^{9}Be target with a thickness of 4 g/cm^2. The fragments were sorted using the FRS (fragment separator), then slowed down and finally stopped in an active stopper (active means that the stopper itself is a detector, see below).

The separation of the fragments happens on two levels. The first level is the FRS. However, the FRS is not setup to pass only a single isotope. Instead, various detectors inside the FRS enable us to identity every particle individually. By sorting the events electronically, we can thus run studies on various isotopes at once.

The fragmentation reaction produces the fragment nuclei in a highly excited state. Unfortunately, the typical lifetime of these excited states is small compared to the travel time through the FRS (roughly 300 ns). Therefore, nuclei only have a chance to arrive at the stopper in an excited state if they have long-lived (isomeric) states with a lifetime

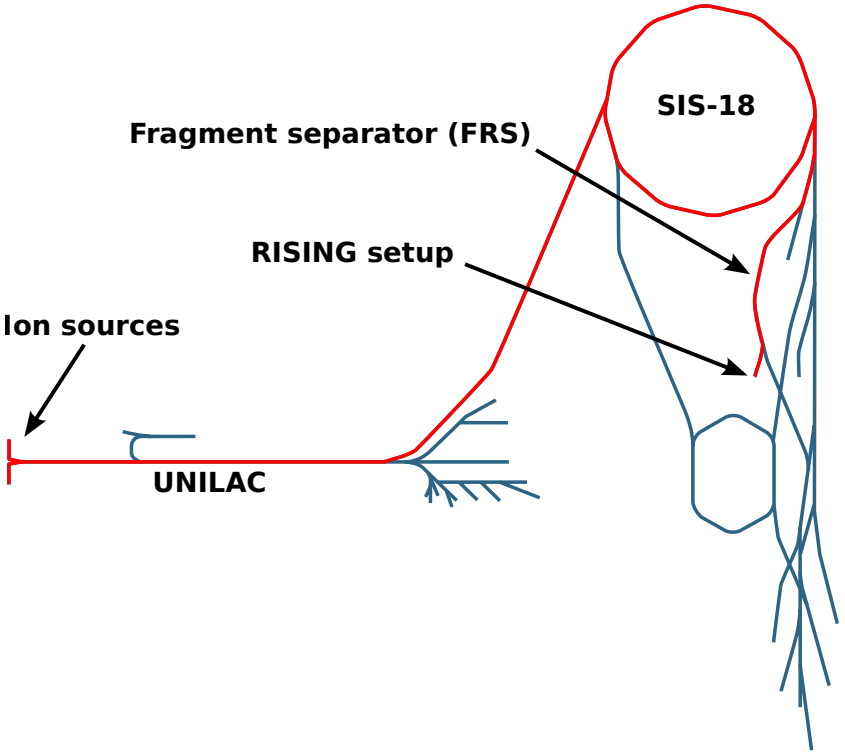

Figure 2.1: Schematic view of the GSI accelerator complex. The beam path relevant for our experiment is highlighted in red.

larger than or comparable to the travel time through the FRS. To study the γ decay of these isomeric states, the active stopper is surrounded by a large array of HPGe (high-purity germanium) detectors, the RISING array.

Eventually, the nuclei inside the stopper will decay. The stopper is formed by a silicon detector, so the decay products can be measured. Usually, the particle decay will populate excited states in the daughter nucleus, the γ decay of which can also be measured with the Ge array.

2.2 GSI accelerator complex

The GSI is a large nuclear/particle physics research facility located near Darmstadt, Germany. Nuclear physics research topics include exotic nuclei, super-heavy nuclei and high-precision mass measurements.

GSI started with a linear accelerator called UNILAC. Later, the heavy ion synchrotron SIS-18 was added. Accelerator beamtime is shared between the experiments. The fragment separator FRS uses the beam from the SIS-18.

A schematic overview of the beam path from its source to the experiment is shown in

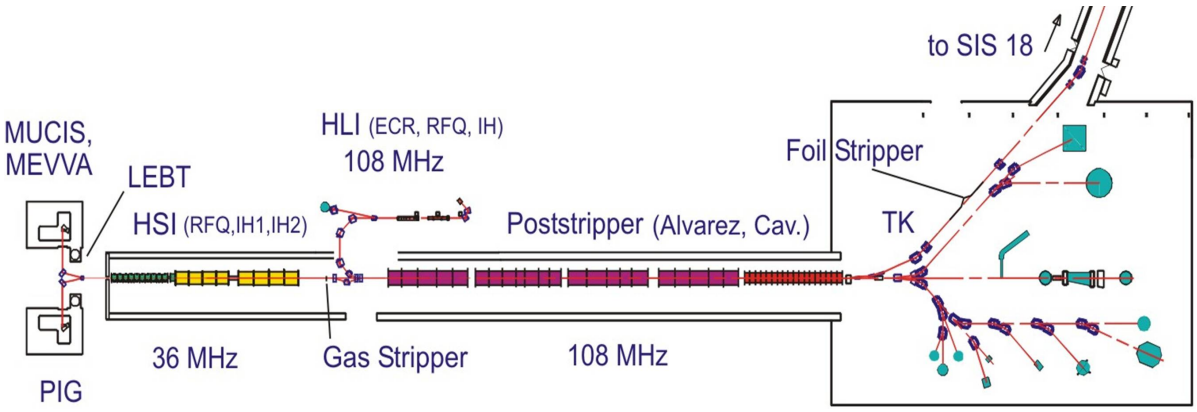

Figure 2.2: The UNILAC linear accelerator at GSI (from [2]).

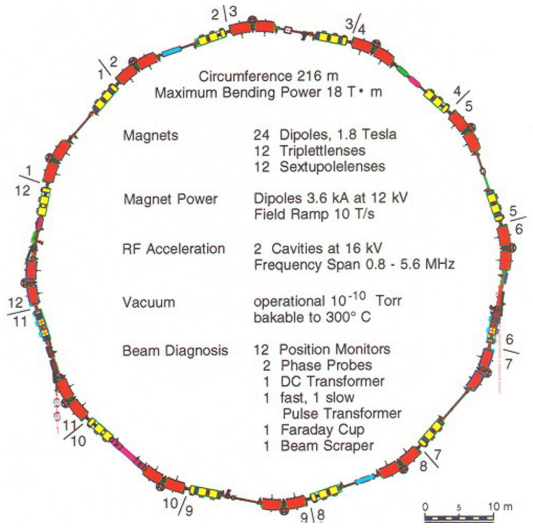

Figure 2.3: The SIS18 synchrotron at GSI (from [4]).

fig. 2.1. At the beginning of the acceleration process, an ion source produces positively charged ions from neutral xenon gas. The entire source setup is on high potential with respect to ground, which accelerates the exiting ions to the injection energy of 2.2 keV/u. The ions then enter the UNILAC linear accelerator (fig. 2.2 and [2]), which accelerates the ions to an energy of 11.4 MeV/u (standard value, from [3]). Inside the UNILAC, a gas stripper removes further electrons from the already accelerated ions, thus increasing their charge and enabling higher energy gains in the following UNILAC section. After the UNILAC, the ions pass a second (foil) stripper. At this point, their energy is high enough for the stripper to remove all (or almost all) remaining electrons.

The major share of the acceleration, from 11.4 MeV/u to 850 MeV/u, happens in the SIS-18 (from German: *Schwerionensynchrotron*; fig. 2.3 and [4]). The SIS-18 is a 216 m

circumference synchrotron. The particles are injected, then accelerated, and finally fed to the production target. The ejection of a bunch of particles onto the production target is called a spill. A spill has a typical duration of the order of one second, with spills being of the order of seconds apart. A fast spill repetition rate requires the magnetic field strength in the SIS to vary quickly, which needs large power supplies (tens of MWs) to remove and supply the energy stored in the magnets.

Between the injection of particles into the SIS, the UNILAC would normally be idle. There are, however, a number of experiments for which the UNILAC energy is sufficient. By quickly switching ion sources at the entrance and beam lines at the exit, these experiments can share the UNILAC with the SIS. Therefore, a UNILAC-only and a SIS experiment will typically run in parallel.

2.3 FRS fragment separator

The high-energy xenon ions can now be fragmented to produce the exotic nuclei of interest. It is clear that the fragmentation is a stochastic process, producing a large number of possible fragments. In order to study a specific nucleus of interest, it is required to identify them. While electronic event-by-event particle identification is employed in our experiment (see detailed description below), the production rates for fragments near the valley of stability are so much greater than those for highly exotic fragments that no reasonable system could handle the total event rate required. Therefore, a two-step process is employed where the fragment stream is first filtered by a system of magnets and slits and event-by-event particle identification is only used on the part of the fragments that remain.

Fig. 2.4 shows a simplified overview of the FRS. The primary xenon beam enters from the left and hits the fragmentation target. The fragments then enter the first sorting stage, consisting of two dipole magnets.

To understand the sorting process, consider the motion of a relativistic particle in a constant magnetic field with the field vector perpendicular to the particle velocity [5]. The resulting motion is circular, with the radius ρ given by

$$\gamma m \frac{v^2}{\rho} = qvB \tag{2.1}$$

where m and q are the particle mass and charge, v is the magnitude of its velocity, c is the speed of light, B is the magnitude of the magnetic field and

$$\beta = \frac{v}{c} \text{ and } \gamma = \frac{1}{\sqrt{1-\beta^2}} \tag{2.2}$$

as usual. Let us assume that all fragments are fully stripped nuclei. Their charge is then given by $q = eZ$, where e is the elementary charge and Z is the number of protons in the

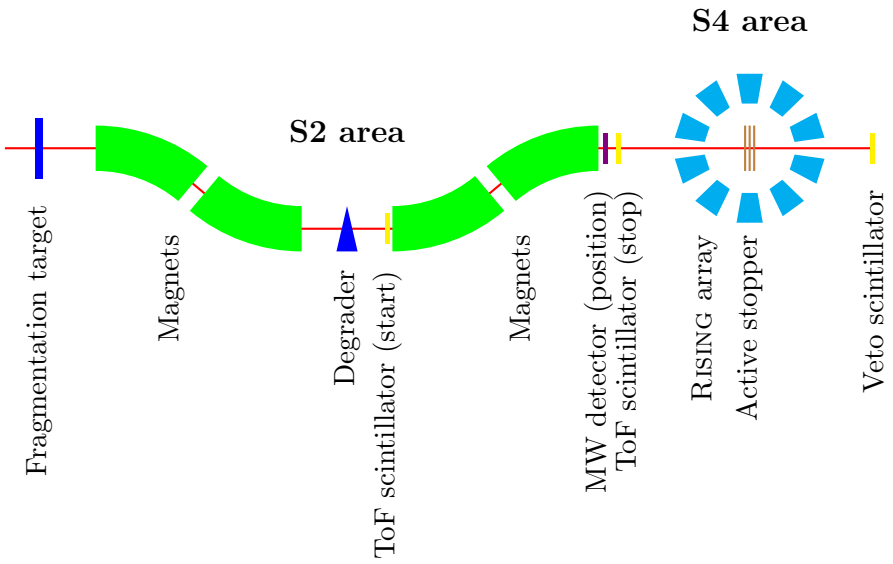

Figure 2.4: FRS overview (simplified).

nucleus. For the mass, we get $m = m_0 A$, where $m_0 = m_p \approx m_n$ is the proton/neutron mass and A is the mass number of the nucleus.

Equation 2.1 can now be rewritten to read

$$B\rho = \frac{m_0 c}{e} \frac{\beta}{\sqrt{1-\beta^2}} \frac{A}{Z} = \text{const} \cdot \frac{A}{Z} \tag{2.3}$$

which implies that the deflection in a magnetic field can be used to sort fragments with equal velocity by their A/Z ratio. This alone is not sufficient, so a sorting step by Z is required next.

By the Bloch equation, the energy loss ΔE of charged particles passing through matter is

$$\Delta E \propto Z^2 f(\beta) \tag{2.4}$$

A piece of matter in the beam (degrader) after the A/Z sorting step will therefore slow down the fragments depending on their Z. In the next pair of magnets, A/Z is now constant, but v (and therefore β) is now dependent on Z, so that the radius effectively depends on Z. This allows for the desired sorting based on Z.

Details on the FRS may be found in [6].

2.4 FRS detectors

In order to further enable the event-by-event electronic particle identification, the FRS is equipped with various detectors. Fig. 2.4 gives a coarse overview. Fig. 2.5 shows the

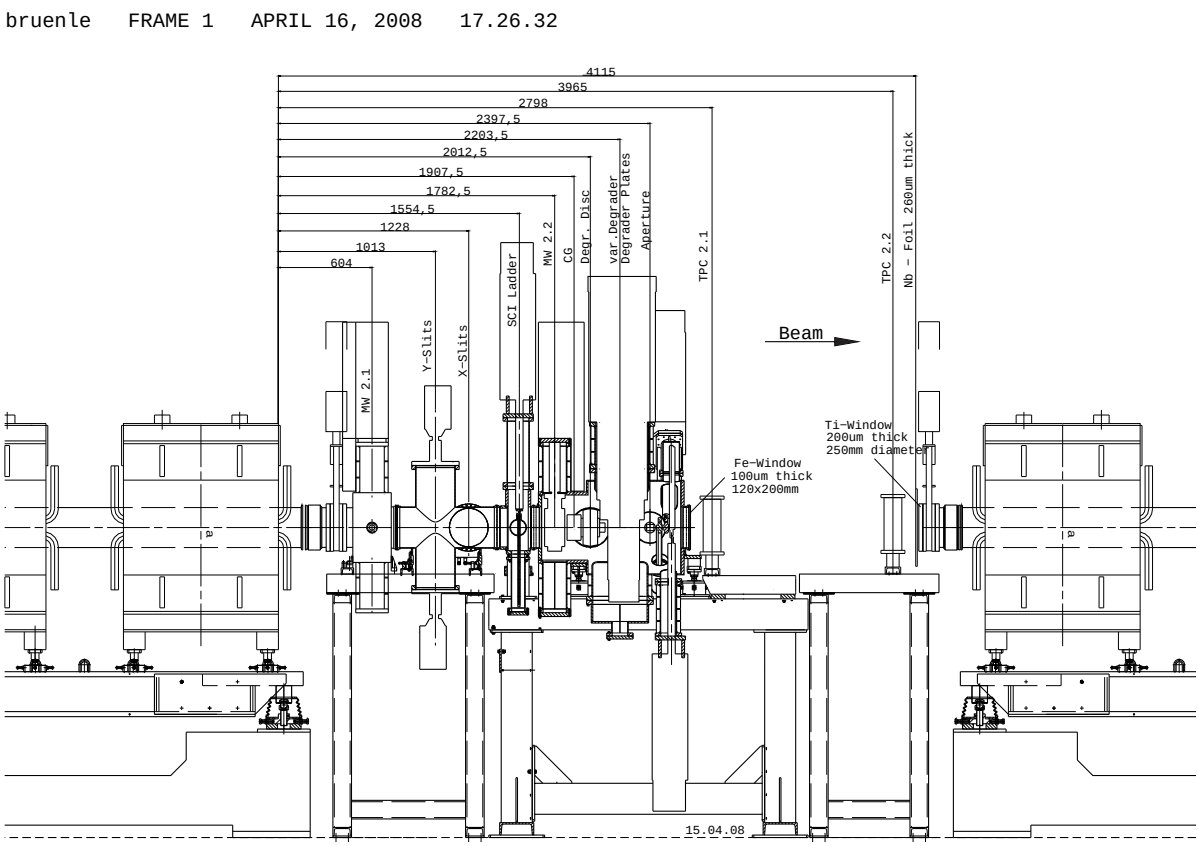

Figure 2.5: Setup of the S2 area of the FRS [7].

exact setup of detectors (as used in this experiment) in the area between the magnet pairs (S2 area, refer to fig. 2.4) and fig. 2.6 shows the detectors at the exit of the FRS (S4 area).

The electronic particle identification is explained in detail in section 3.1.5. The measurements needed include precise timings for time-of-flight (ToF), giving access to the particle velocity, position measurements, giving access to the path of the particle through the magnet and thus the curvature radius, and energy loss measurements, giving access to the particle charge via the Bethe-Bloch equation. The various types of detectors used will now be described in detail.

2.4.1 Scintillators

Scintillator detectors are based on materials that emit light when charged particles pass through them and deposit energy. The light is then detected, typically by using

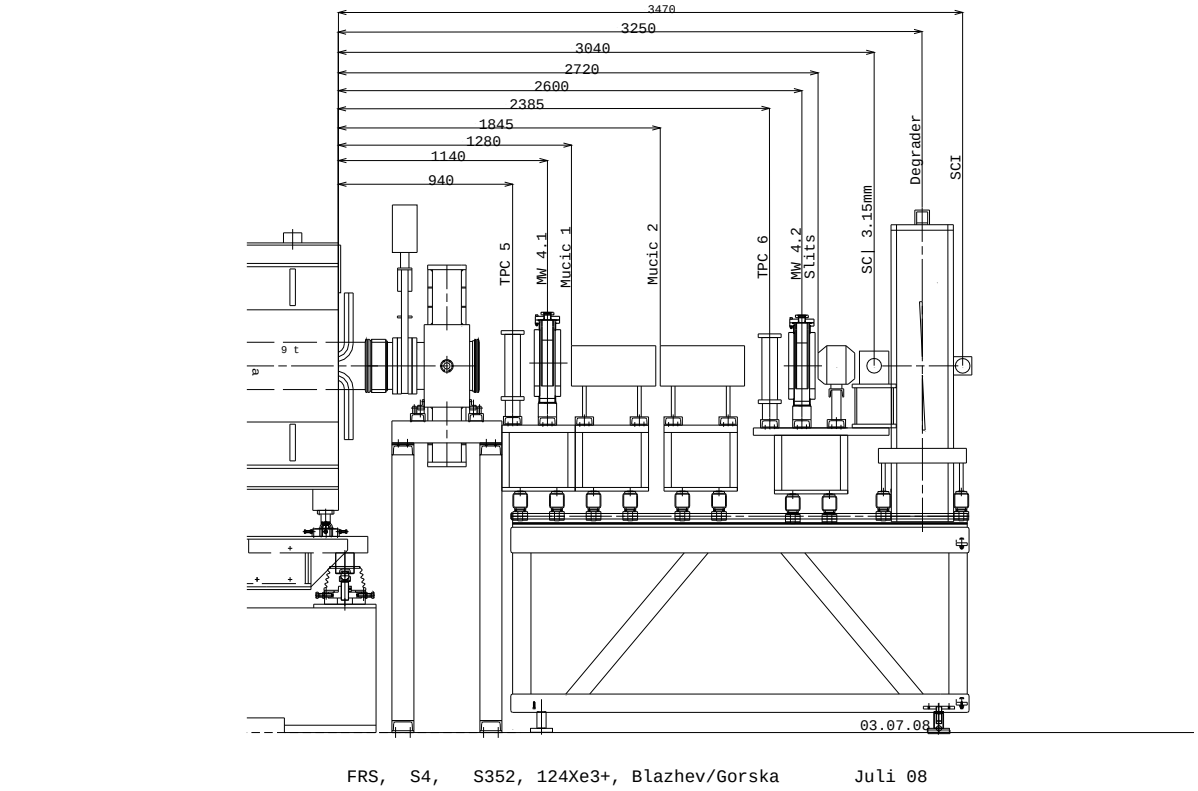

Figure 2.6: Setup of the S4 area of the FRS [7].

photomultiplier tubes.

The amount of light generated is proportional to the energy deposited, so the detectors can be used for energy loss measurements. The energy resolution is limited by the number of photons reaching the photomultiplier tube and the resulting counting noise. Scintillator detectors are fast (FWHM timings of the order of tens of ps). By using photomultiplier tubes on either side of the scintillator, they can also be made position sensitive (FWHM of the order of a few mm).

2.4.2 Time projection chambers (TPCs)

Time projection chambers are gas-filled chambers where charged particles leave tracks of ionized gas. A high electric field separates the charges and transports them to the end plates, where they are detected. The position along the electric field is determined from the time of flight, whereas the position tangential to the electric field can be determined via segmented detectors at the end plates.

2.4.3 Multiwire proportional counters (MWs)

The multiwire proportional counter is a position sensitive detector. Particles passing through the gas-filled detector create ions which then drift in an electric field and are amplified via an avalanche effect. Finally, the avalanche hits the anode. Close to the anode, two sets of perpendicular cathode wires are located. The avalanche hitting the anode induces a current pulse on the nearest cathode wires. The difference in charge collected on either end of the cathode wire gives the position of the avalanche along that wire. As there are two perpendicular sets of cathode wires, an (x,y) position can be reconstructed.

2.4.4 Multi-sampling ionization chambers (MUSICs)

The Multi-Sampling ionization chamber is used to measure the charge of the particles. It consists of a gas-filled chamber where the beam particles cause ionization as they pass through. There are eight anodes in the chamber, each collecting charge from a defined region. Thus, the MUSIC produces eight signals. In the analysis, they are combined by rejecting two outliers and averaging the six remaining measurements.

In order to keep the load on the extremely thin entry and exit windows of the MUSIC as low as possible, the gas inside the detector is at ambient pressure. For longer experiments, this implies that the gas pressure (and thus the gas particle density) varies over time.

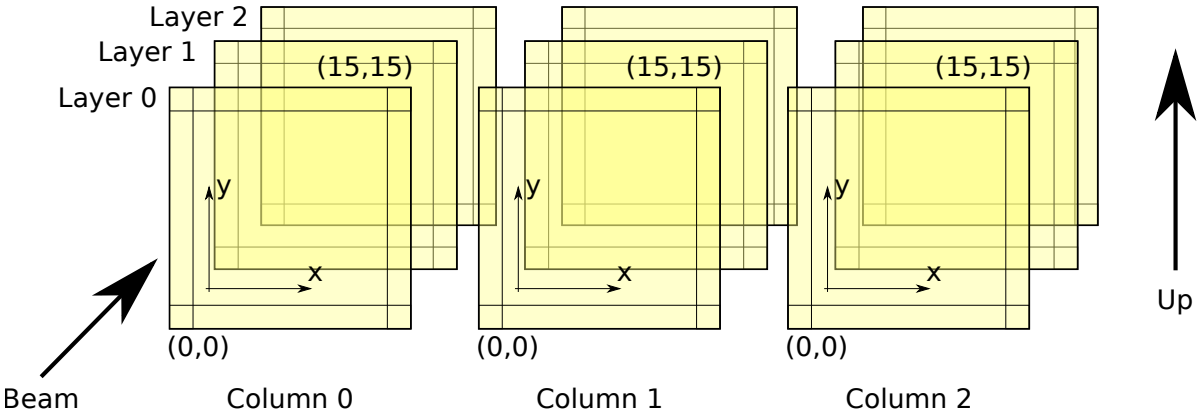

Figure 2.7: Layout of the active stopper detector. (For compatibility with the analysis software, a numbering convention starting at 0 is used, like in the C programming language.)

2.5 Active stopper

The experiment described in this thesis uses the setup in *stopped-beam* mode, meaning that the nuclei of interest are studied after they have come to rest inside a suitable stopper. After implantation in the stopper, the unstable nuclei eventually decay (in the case of neutron-deficient nuclei, usually by β^+ decay). To be able to study the particle decay products as well, an active stopper is used.

The β-lifetime of our exotic nuclei is much larger than the time between the two nuclei hitting the stopper (seconds vs. milliseconds). This means that, if a β decay takes place, the parent nucleus is unknown. The problem is solved by using a segmented silicon detector as the stopper (active stopper). This allows for *implantation-decay correlation*. Remember that, at implantation time, the nucleus being implanted in known (from the FRS particle identification). If we remember the implantation position, the parent nucleus in a subsequent decay at the same position is known. For the technique to work, the implantation rate *in a given silicon pixel* must be less than the β lifetime.

Our active stopper consists of double-sided silicon strip detectors (DSSSDs). In these detectors, both sides are segmented in strips, with the strips on one side being orthogonal to those on the other side. If there is a single event in a given time window, this arrangment allows the determination of an x and a y coordinate, effectively giving a pixelated detector (but with far less channels to read out). The drawback versus an actual pixelated detector is, of course, that an ambiguity results for two or more events in the time window and the positions can no longer be uniquely determined. Our detectors have 16 strips per side, yielding effectively 256 pixels per detector.

The geometric arrangement of the detectors in shown in fig. 2.7. There are a total of 9 DSSSDs, arranged in 3 layers of 3 detectors each. The size of each detector is 5x5cm, with a thickness of 1mm.

2.6 RISING germanium array

2.6.1 γ ray detection with high-purity germanium (HPGe) detectors

In this section, the physics of γ detection using HPGe detectors will be briefly described. These detectors are essentially semiconductor diodes operated in reverse direction, with the voltage chosen high enough that the entire detector volume is depleted. Current can only flow if electron-hole pairs are generated in the depleted region. The energy from γ quanta being absorbed in the detector will ideally go completely to the production of electron-hole pairs. As the energy required to generate a single electron-hole pair is constant, the absorption of a γ quantum in the detector will generate a current pulse whose integral (i.e. total charge) is proportional to the energy of the γ quantum.

Of course, the idealized picture is not entirely correct. The energy from the γ quantum can go either to the creation of electron-hole pairs or to lattice vibrations (phonons). This is a statistical effect, so the number of electron-hole pairs created from a γ quantum of a given energy will vary, creating noise. In addition, inevitable impurities in the crystal create energy levels inside the band gap. These can lead to electron-hole pairs recombining or not arriving at the detector electrodes inside the collection time window (trapping). A third noise source is the inevitable noise created in the electronic circuits required to register the current pulse.

There are three mechanisms by which γ radiation interacts with matter: photo effect, Compton effect and pair production. In the photo effect, the γ quantum is completely absorbed and its entire energy is transmitted to an electron (which then creates electron-hole pairs). In the Compton effect, the γ quantum is scattered by an electron and only transmits part of its energy. Pair production refers to the creation of an electron-positron pair from the γ quantum. For this effect to be possible, the γ energy has to be at least the rest mass of the electron and the positron ($2 \cdot m_e = 1022$ keV). (Note that pair production from a single γ quantum cannot happen in a vacuum due to the conservation of momentum. In the detector, however, an atom from the detector material can take the momentum.)

In practice, two or all three of the effects mentioned can happen during the absorption of a single γ quantum. The γ might, for example, first produce an electron-positron pair. The kinetic energy of the electron and the positron creates electron-hole pairs. The positron will eventually annihilate with an electron from the detector material, producing (typically) two new γ quanta with an energy of 511 keV each. These may then undergo Compton scattering until they are finally fully absorbed by the photo effect. The timescale on which such a sequence of events happens is so short that the detector electronics cannot resolve it (it may, however, be able to resolve the different positions where the events took place; see below).

Fig. 2.8 shows the schematic energy spectrum produced by monoenergetic γ radiation in the detector. (We assume that the energy of the radiation is above the pair production threshold.) The rightmost peak is the full-energy peak (sometimes called

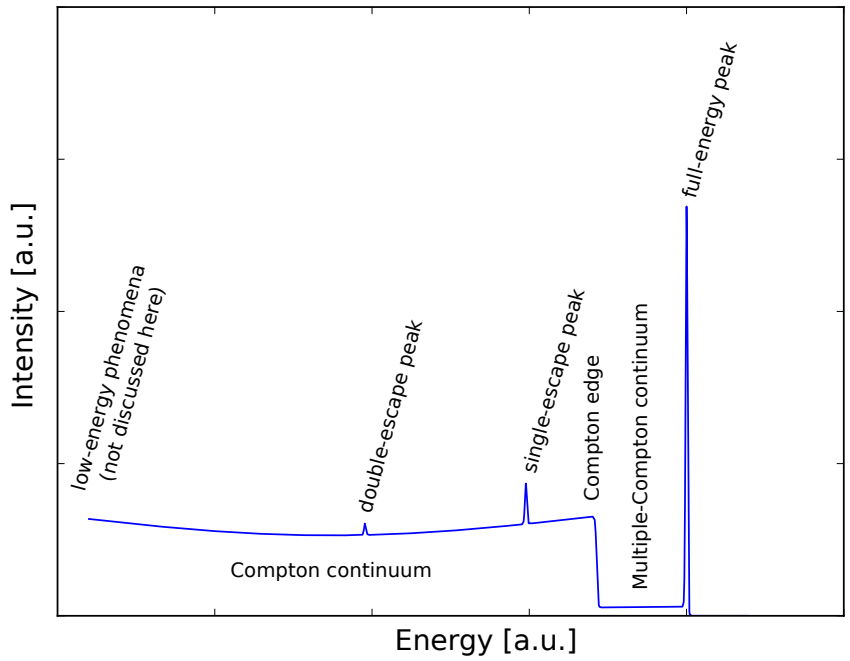

Figure 2.8: Schematic energy spectrum for the interaction of monoenergetic γ radiation with a germanium detector. γ energy assumed to be above the pair production threshold. (See text for explanation.)

the photopeak), corresponding to events where the full energy of the γ quantum was absorbed in the detector. 511 keV below it is the single-escape peak. It corresponds to events where pair production took place and one of the annihilation γ quanta escaped the detector without further interaction, while the rest of the original γ energy was completely absorbed. Likewise, the double-escape peak 1022 keV below the full-energy peak corresponds to events where both annihilation quanta escaped the detector. The continuum corresponds to γ quanta that left the detector again after undergoing Compton scattering and depositing part of their energy.

Consider the scattering of a γ quantum on an electron initially at rest. Conservation of four-momentum implies a connection between the initial γ energy E_γ, the final γ energy E'_γ and the scattering angle θ:

$$\frac{1}{E'_\gamma} - \frac{1}{E_\gamma} = \frac{1}{m_e c^2}(1 - \cos\theta) \tag{2.5}$$

The energy difference $E_\gamma - E'_\gamma$ goes into kinetic energy of the electron and finally into creation of electron-hole pairs, which are then detected. Rearranging the equation gives an expression for this energy difference:

$$E_\gamma - E'_\gamma = E_\gamma \left(1 - \frac{1}{1 + \frac{E_\gamma}{m_e c^2}(1 - \cos\theta)}\right) \tag{2.6}$$

From the equation, it is apparent that the γ quantum cannot transmit its entire energy in a single Compton scattering event. This gives rise to the Compton edge at an energy

$$E_c = E_\gamma \left(1 - \frac{1}{1 + 2\frac{E_\gamma}{m_e c^2}} \right) \tag{2.7}$$

Obviously, this analysis is valid only for a single Compton scattering event. As there is a small probability that the γ quantum undergoes multiple Compton scatterings before leaving the detector again, the gap between the Compton edge and the full-energy peak is filled by a smaller multiple-Compton continuum.

The probability for Compton scattering is dependant on the scattering angle θ, and thus on the energy transmitted. The Compton continuum is therefore not flat, but slightly curved. In lowest order of quantum electrodynamics, the angle-dependent Compton scattering probability is given by the Klein-Nishina formula [8]. The derivation is rather involved, so it will not be discussed further.

Software packages exist which can simulate the HPGe detector response to γ rays with given energies using Monte-Carlo techniques. GEANT is one example ([9], [10], [11]).

In actual measurements, where γ rays with several discrete energies are to be detected, the complex detector response of germanium detectors causes some problems. The Compton background is the most severe. Given finite statistics, the Compton contiuum will be subject to Poisson (counting) noise. The noise in the Compton continuum from a high-intensity γ ray may completely swamp the full-energy peak of a lower-energy, lower-intensity γ ray. As such, it is highly desirable to reduce the Compton continuum. The traditional way of doing this is to surround the germanium detector with anti-Compton shields. These shields are scintillators made from bismuth germanate (BGO). Due to the high Z of the scintillators, a γ ray entering them is highly likely to be detected. Unfortunately, the energy resolution of the scintillators is rather poor. They can therefore only be used as a veto, meaning that events where the scintillator saw something are thrown away. With anti-Compton shields, the Compton background can be significantly reduced. It cannot be completely eliminated, however, because the side of the Ge detector looking at the γ source must stay open, and there is a certain probability of Compton scattering under an angle of almost 180°.

A highly sophisticated modern alternative is used in γ arrays such as AGATA [12]. These arrays surround the γ source with essentially a hollow sphere of detector material. This makes it highly likely that a Compton scattered γ is eventually absorbed in another detector, and its total energy can be reconstructed by summing the measurements in the different detectors. A complication arises because typically, multiple γ rays are emitted from the source simultaneously. To disentangle the events from the various original γ rays, highly segmented, position sensitive detectors and maximum-likelihood methods are used.

2.6.2 Analysis of HPGe data

In an actual experiment, there is typically no interest in the details of the HPGe detector response, but in the (discrete) energies and the intensities of the original γ rays. This is normally done by peak fitting. Usually, only the full-energy peak is considered. The shape of the full-energy peak is nearly Gaussian under ideal circumstances. A common source of deviations from that shape is neutron damage, where the crystal structure of the detector material has been damaged by neutrons. This results in a low-energy tail in the peak shape. Precise modelling of the tail is difficult, so empirical descriptions are used, several of which have been proposed over the years.

As mentioned already, the full-energy peak sits atop the Compton continuum from higher-energy γ rays. Again, precise modelling of the Compton continuum is difficult. It is therefore approximated by an empirical formula, e.g. a polynomial, in the vicinity of the peak of interest. In practice, one manually chooses two peak-free regions left and right of the peak of interest and fits the background description to these regions. In the next step, the chosen peak description is fitted to the actual peak, with the background substracted. If two peaks partly overlap, they can be separated by fitting the sum of two peak descriptions.

The method described here has a number of drawbacks. In peaks with tails and high statistics, it is normally found that even the best parameters for the empirical shape deviate from the actual data in a statistically significant manner. The accuracy of peak position and integral obtained from the empirical description is therefore questionable. Also, the position and integral error calculated by the fitter is then mostly meaningless. In practice, the errors are usually estimated rather than obtained as results of the fitting process.

The second drawback of the method is that the identification of the peaks, and the selection of the peak-free regions used for background fitting, are a completely manual process. In cases where the number of spectra to be analyzed is large, or there are many peaks in each spectrum, this quickly become a laborious, dull, and error-prone task. Apart from that, the results obtained now depend on (partly) subjective choices made by the person analyzing the data, which makes a rigorous error analysis even more difficult.

In the experiment described in this thesis, the number of peaks of interest was fortunately small. An exception is the energy calibration of the detectors, which requires fitting some ten peaks in about 100 spectra. In that case, however, one has additional information about the expected peaks present in the spectrum and their positions (because the energy calibration can be assumed to be nearly linear). This allows to tolerate a certain number of false positives/false negatives from a less-than-perfect heuristic for peak finding. Still, some detectors with significantly worse peak widths required manual intervention. The automatic Ge energy calibration developed during this work is described in further detail in section 3.3.

After the peak positions and integrals have been determined, we need to convert them

to energies and (relative) intensities. For converting the peak positions, we need an energy calibration of the detector. As was already mentioned, the charge pulse generated in the detector is roughly proportional to the energy deposited (which is equal to the energy of the γ quantum in case of the full-energy peak). We thus need to determine the constant of proportionality between ADC (analog-to-digital converter) channels and γ energies. This is done by using a γ source with known energies. In practice, the relation between ADC channels and energies turns out to also include an offset and (small) non-linear terms. The relation between ADC channels c and energies $E(c)$ is described by a polynomial,

$$E(c) = \sum_{i=0}^{N} a_i c^i$$

with the order N typically three or less, and the expectation that the higher-order terms $a_2c^2, \ldots$ be small.

For converting full-energy peak integrals to (relative) intensities, we need an efficiency calibration, i.e. we need to know how likely a γ quantum of a certain energy is to be fully absorbed in the detector. Given the complexity of the interaction between γ radiation and the detector described above, a simple relation for this energy dependance is not expected. In fact, it turns out to be sufficiently complex that an analytical description is normally not attempted. (Note, however, that Monte Carlo simulations, as mentioned above, can describe the relation fairly well.) In practice, the calibration data is fitted with an empirical formula having a large number of parameters (up to seven).

The popular RadWare [13] package uses a function of the type

$$\epsilon(E_\gamma) = \exp\left(\left((A + B*x + C*x*x)^{-G} + (D + E*y + F*y*y)^{-G}\right)^{-1/G}\right) \quad (2.8)$$

where $x = \log(E_\gamma/E_1)$ and $y = \log(E_\gamma/E_2)$, and $E_1 = 100\,\mathrm{keV}$ and $E_2 = 1\,\mathrm{MeV}$ are fixed.

Another empirical formula was first proposed by I. Wiedenhöver [14]

$$\epsilon(E_\gamma) = A\exp\left(-B\ln(E_\gamma - C + D\exp(-EE_\gamma))\right) \quad (2.9)$$

Non-linear fitting has severe problems with local minima and sensitivity to starting parameters. It might therefore be objected that, if an empirical formula is fitted anyway, the non-linear fit is best avoided. A better idea may be to fit a polynomial to the log(energy)/log(efficiency) plot, as discussed in [15]. (Note that fitting a polynomial is a linear fit.)

2.6.3 RISING

The Rising (Rare Isotope Spectroscopic INvestigation at GSI) array consisted of 105 non-segmented HPGe detectors (it has since been decommissioned). Seven detectors

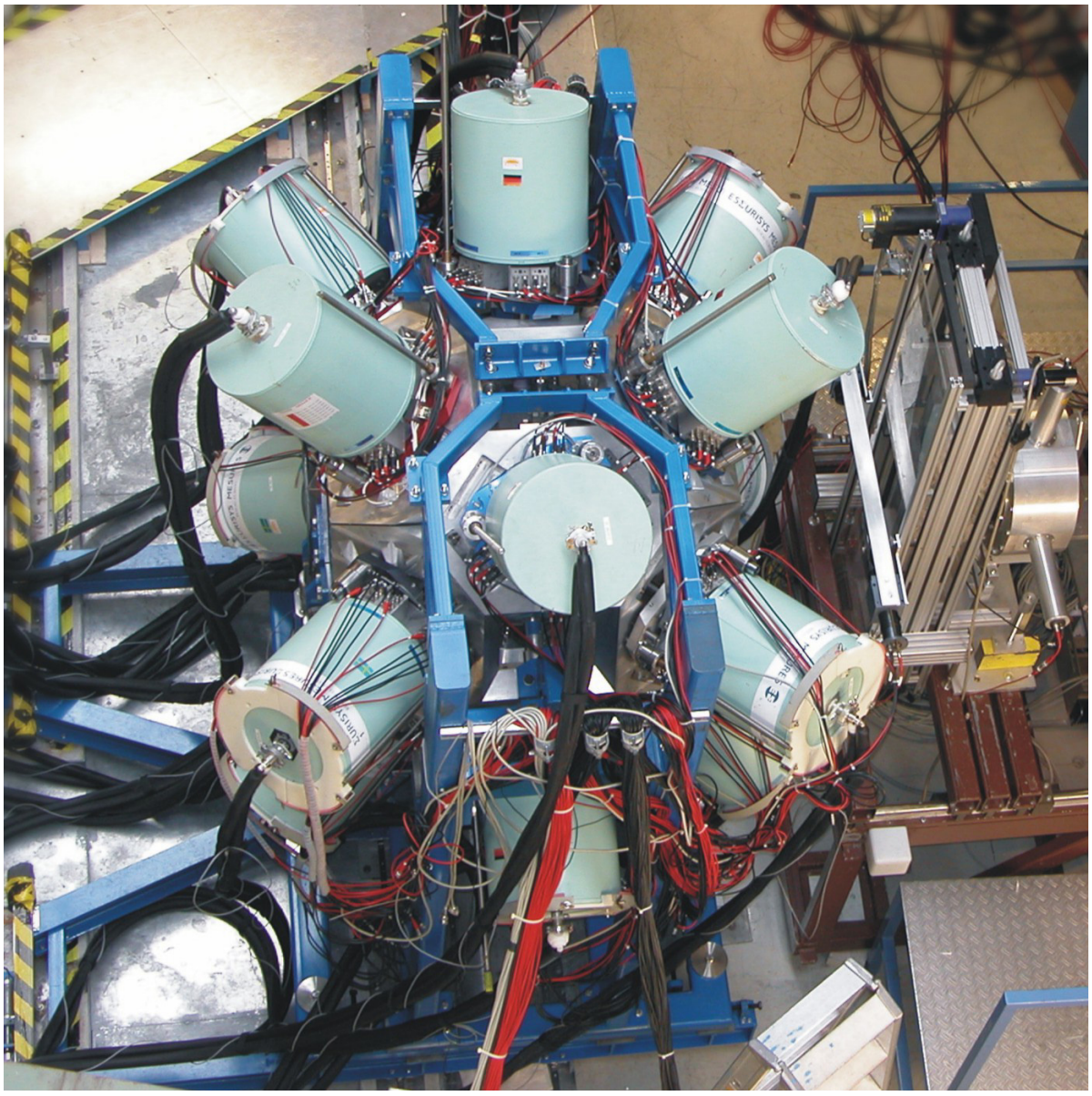

Figure 2.9: Photograph of the RISING setup (Jerzy Grębosz, Instytut Fizyki Jądrowej, Krakow).

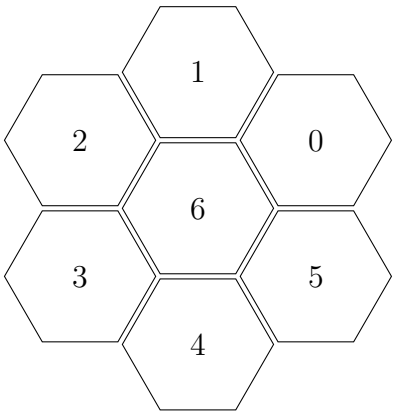

Figure 2.10: Arrangement of detectors in a EUROBALL cluster.

form a EUROBALL cluster [16], for a total of 15 clusters in the array. The detectors in a cluster are packed close together in a common cryostat (see fig. 2.10).

As mentioned, the exotic nuclei in the experiment described in this thesis decay in the active stopper, i.e. at rest. The decay γ radiation is thus emitted isotropically. The detectors are distributed evenly around the stopper (the so-called *stopped beam* configuration of the array). Fig. 2.9 shows a photograph of the setup. The photopeak efficiency, i.e. the fraction of γ quanta emitted at the stopper which are fully absorbed and detected in a detector of the array is estimated at around 10% at 1.3 MeV. (Note that the efficiency is highly dependent on the energy of the γ quanta.) Because of technical problems, only 99 of the 105 detectors could be used for this experiment.

The clusters can be equipped with anti-Compton shields, this, however, is not done for RISING. The only anti-Compton measure used is add-back, i.e. the addition of simultaneous energy depositions in neighbouring detectors in a cluster. This is described in more detail in section 3.1.6.

The output signal of every germanium detector needs to be processed to accurately determine the amount of charge generated for a given event. Previously, this was done using analog electronics (the shaping or main amplifier). Today, this processing is increasingly done digitally. The signal from the detector preamplifier is fed into a sampling ADC (analog-to-digital converter). The shaping is then done in software, using a combination of an FPGA (field-programmable gate array) and a DSP (digital signal processor). This digital processing is actually essential to achieve the position sensitivity in arrays such as AGATA (pulse shape analysis). In non-position sensitive detectors, it is merely convenient and cheaper.

The RISING array uses XIA DGF (digital gamma finder) modules [17] to perform the digital processing. These modules largely imitate the function of the earlier analog electronics. They detect charge pulses in the detector, digitally determine the amount of charge, and store it together with a timestamp. Additionally, they support external gates, which make the storage of an event dependent on certain conditions (whether

quasi-simulataneous events were seen by other detectors, for example). This helps to keep the data rate manageably low.

Details on the RISING array can be found in [18].

2.7 Data acquistion and trigger system

The data acquisition system is based on the notion of events. There are two main types of events: implantation and decay events. An implantation event corresponds to the arrival of a nucleus in the active stopper; in a decay event, a nucleus in the active stopper undergoes particle decay.

After each event, the relevant data from the detectors is read out and stored. It should be noted that an event can contain several sub-events. If, for example, an excited nucleus is implanted in the stopper and decays via a cascade, several γ quanta could be detected. The timing information for these sub-events is generally relative to the event trigger. High-resolution relative timing information is only available for sub-events within the same event, but a 1 kHz scaler that is read out at each event provides low-resolution timing across events.

The event-based notion of the data acquisition system extends even to the XIA modules. These modules have a FIFO (first-in first-out) buffer from which the accepted γ events can be read, together with a timestamp, so, in principle, they could be read out asynchronously. For compatibility with the rest of the data acquisition system, however, they are read out once per event. The event trigger is fed to a special channel in one XIA module, so that the internal timestamps can be synchronized to the event timing.

In addition to the XIA modules internal timestamp (40 MHz clock), there are two TDC (time-to-digital converter) based Ge timing systems. The long-range TDCs are based on special chips developed at CERN. Each module (CAEN v767) provides 128 channels with multihit capability and 800 ps LSB resolution (LSB = least significant bit, i.e., for this device, a change in the value by one corresponds to 800 ps). In addition, there are short-range TDC modules with approx. 300 ps LSB resolution. The timing system for the Si strips uses the same modules.

An implantation event takes place when a particle traverses the FRS and is stopped in the active stopper. Such an event is triggered by a scintillator in front of the stopper (Sci41 or Sci42). The main data from such an event are the particle identification information, possible radiation emitted directly after the implantation, and an implantation position from the active stopper.

A decay event is triggered by the active stopper. The active stopper registers a position for later correlation and the decay energy. In addition, if the decay ends in an excited state in the daughter nucleus, the RISING array registers γ energies and times from the subsequent de-excitation.

3 Data analysis

3.1 Software: R2D2

3.1.1 Introduction

The software package used for the analysis of the data is called R2D2. It is based on the ROOT data analysis framework [19] developed at CERN. R2D2 was initially developed for the analysis of the first RISING stopped beam experiment (Feb. 2006, ^{107}Ag beam) and then substantially upgraded and extended for the analysis of the experiment described in this thesis.

For this analysis, R2D2 provided the following services:

- Unpacking of the listmode data
- Application of energy and time calibration (for all detectors where it is needed)
- Germanium cluster add-back
- Reconstruction of implantation positions from silicon data
- Implantation-decay correlation

All of these will be described in more detail below.

3.1.2 Organisation

R2D2 is designed to be modular, so that other experiments with potentially different setups or requirements can easily reuse the relevant parts of it. To achieve this modularity, the concept of actions operating on the data stream is used. The idea comes from the analysis software used by the ALADIN collaboration at GSI, developed under the leadership of Walter Müller.

The concept is illustrated in fig. 3.1. We assume that the data comes in events, i.e. groups of detector readings that lie close together in time. The unpacker reads one full event from the listmode data stream. For efficiency reasons, we use data containers that are allocated once and get re-filled (i.e. overwritten) at each event. Each action class takes one or several data containers as input and fills one or several data containers with its output. Action class input data that does not change for each event (e.g. coefficients of calibration polynomials) is called configuration and stored in configuration classes.

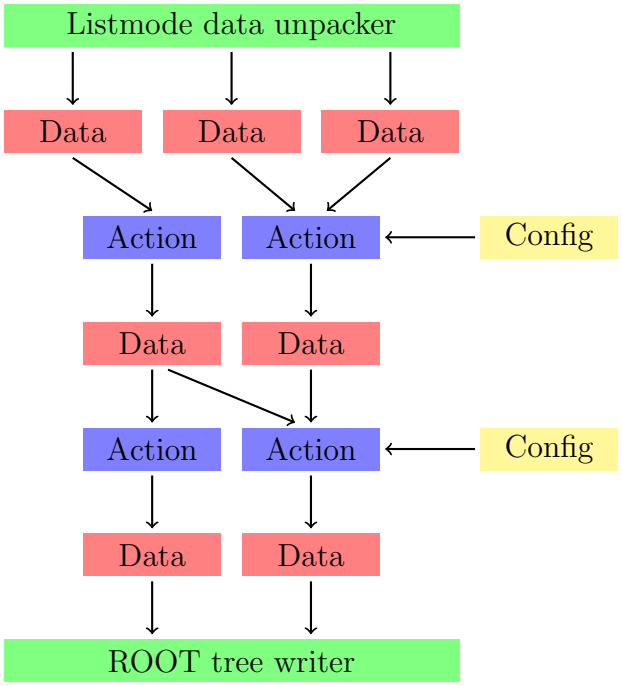

Figure 3.1: Illustration of the R2D2 data flow (see text).

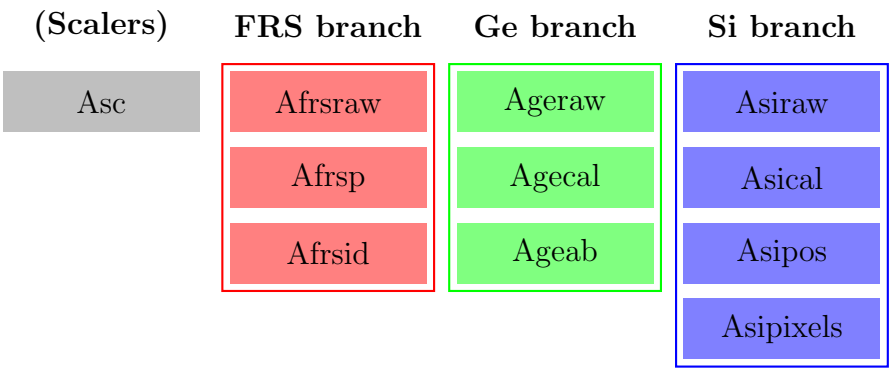

Figure 3.2: Branches (detector groups) in the R2D2 software.

At the end of the action chains, the processed data is stored in a ROOT tree, again on an event by event basis. Note that R2D2 does not handle histogramming of data from different events, except for debugging. There is a separate software, called C3PO, to generate the final histograms.

3.1.3 Unpacker

The first task in R2D2 is to extract the data from the listmode data stream. The data stream essentially consists of raw data as received from the various electronic modules, with very little processing applied to them. The unpacker needs experiment-specific lookup tables to determine which VME bus addresses correspond to which devices, and device-specific code to convert raw register values into ADC/TDC readings. At the end of the unpacking state, the data consists of concrete ADC/TDC readings corresponding to concrete detectors.

There are three main groups of detectors (called branches): the germanium branch (the RISING array), the silicon branch (the active stopper), and the FRS branch. The first two branches are homogeneous, i.e. they consist of a large number of detectors which are all alike. The third branch consists of many different types of detectors. In addition, there are a number of scalers (counters) which are processed (fig. 3.2).

3.1.4 Calibration

In the next step, the raw ADC/TDC readings need to be converted to physical quantities, i.e. deposited energy and time (difference). This is done by applying a calibration function, $E(c)$ or $T(c)$, where E or T are physical energy or time, and c is a raw ADC/TDC channel. The functions are usually linear, $E(c) = a_1 c + a_0$. They are determined by measuring data with known characteristics. The calibration process is described in more detail in section 3.3 (germanium detectors) and section 3.4 (silicon detectors).

A slight subtlety is illustrated in fig. 3.3. Consider a histogram of the energies of all events. Every ADC channel will, after the calibration, correspond to a certain energy and thus fall in a certain energy bin. Typically, the number of ADC channels corresponding to a certain energy bin will not be constant, but vary from energy bin to energy bin. This will introduce a variation of the bin contents in the energy histogram, even if the initial number of events per ADC channel was constant (fig. 3.3 (a) and (b)). The problem is solved by a technique called *dithering*. A random number from the range (-0.5, 0.5] is added to each ADC reading before application of the calibration function. Note that this does not destroy any information; the original ADC channel can be exactly recovered by rounding. However, the values are now "spread out" over the width of the channel and, after calibration, evenly distributed over the possible energy bins. The result, as shown in fig. 3.3 (c), is that data with a flat distribution over ADC channels now results in an energy histogram that is also flat (except for Poission noise).

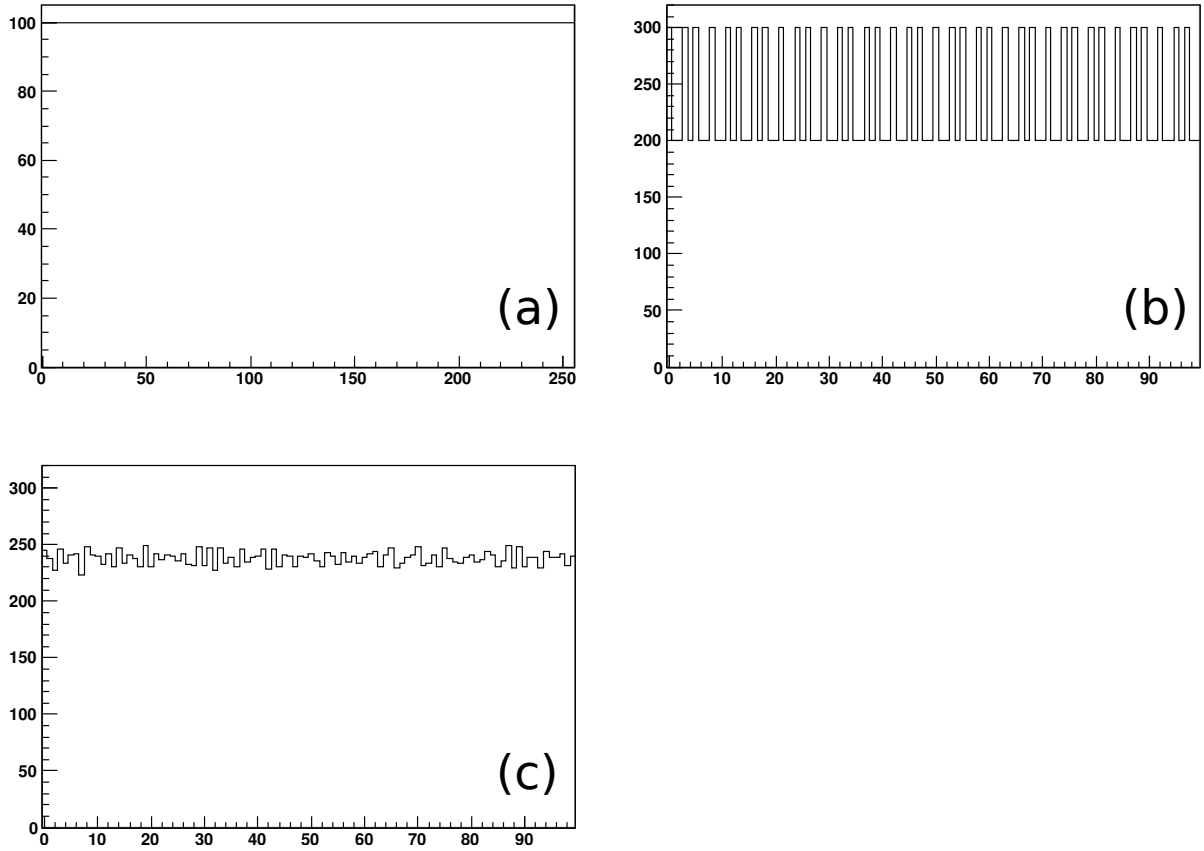

Figure 3.3: Demonstration of dithering: (a) simulated raw ADC spectrum, 256 bins, 100 counts per bin (b) result of "calibrating" the histogram with $E = 0.42 \cdot c$ and re-binning with 100 bins: semi-regular structure appears (c) the same operation with dithering: the structure is reduced in amplitude and no longer regular.

3.1.5 Particle identification

The next major step in the data processing is to turn the information from the FRS detectors into a particle identification. As noted before, particle identification is only possible for implantation events; for decay events, implantation-decay correlation, as described below, will have to be used.

In order to fully identify the nuclei, two quantities have to be determined: A/q (mass over charge) and Z (nuclear charge). Determination of A/q works similarly to the magnetic sorting in the FRS, as described in section 2.3, and makes use of the formula

$$B\rho = \frac{m_0 c}{e} \frac{\beta}{\sqrt{1-\beta^2}} \frac{A}{q} \tag{3.1}$$

m_0 (nucleon mass), c and e are simply constants. The magnetic field B in the magnets can be measured using Hall probes or Nuclear Magnetic Resonance techniques; also, it is expected to be mostly constant during the experiment. This leaves $\beta := v/c$ and the curvature ρ to be determined.

The curvature ρ follows from measuring the position of the particle as it passes through the S2 and S4 areas. As the particle identification is essential for the experiment, several independent position measurements are made, using scintillators and time projection chambers (TPCs).

Determining the beam particle velocity $\beta = v/c$ requires knowledge of the path taken, i.e. the curvature ρ, and the time-of-flight. The latter can be measured with high accuracy by a pair of scintillators. Again, several measurements are taken for redundancy.

The determination of the nuclear charge Z makes use of multi-sampling ionization chambers (MUSICs). As described in section 2.4.4, the MUSIC detectors measure the ionization of gas by the beam particles. By the Bethe formula, the energy deposited will depend on the beam particle charge q, the beam particle velocity β, and the gas particle density. The gas inside the MUSIC is at ambient pressure and temperature, which are measured during the experiment and used to calculate the gas particle density. β is also known (see above), allowing the charge q of the beam particles to be determined. It should be noted that q is not equal to the nuclear charge Z, because the beam particle picks up and loses electrons from and to the gas. However, the path through the MUSIC detector is long enough to cover many such pick-ups and losses, giving a definite relation between q and Z. After calibration, Z can thus be obtained.

The final result of these measurements is, on a particle-by-particle basis, knowledge of A/q and Z. (See 2d histogram in fig. 4.1.) This allows us to put *gates* on certain regions in the A/q vs. Z histogram and examine prompt γ rays from the nucleus of interest.

3.1.6 Germanium add-back

A common problem with germanium detectors is the occurrence of events in which a γ photon undergoes Compton scattering in the detector and subsequently leaves the

detector again. For these events, only a varying fraction of the γ energy is deposited in the detector, giving rise to background known as the Compton continuum.

As described in section 2.6.1, the germanium detectors in the RISING spectrometer are arranged in clusters of 7 detectors each. This leads to a substantial probability of a Compton scattered photon being fully absorbed in another detector. In such a case, the original γ energy could be recovered by adding the energy signals from the two detectors. Unfortunately, there is no way to distinguish these type of events from two γ quanta arriving at the two detectors in coincidence. In the latter case, add-back will destroy useful information and produce spurious sum peaks. Therefore, we have to use heuristics to make the best use of add-back, while minimizing its unwanted side effects.

The first, obvious heuristic is to only employ add-back if the detectors hit are direct neighbors. While it is possible for a Compton-scattered γ quantum to pass through a detector without interaction, it is very improbable. The second heuristic is to employ add-back only if the sum energy is below a certain value.

While add-back does recover additional statistics, particularly for low-energy events, it also creates structures in the spectra that one needs to be aware of during analysis, like the sum peaks mentioned above or the "jump" caused by the energy-sum heuristic.

3.1.7 Implantation/decay correlation

In order to examine (particle-)decay modes and decay radiation of nuclei implanted into and decaying in the stopper, we need to be able to identify the parent nuclei. As mentioned above, this is made possible by the active stopper, a double-sided silicon strip detector which allows us to determine the position of particle implantations and decays. We note that the energy deposition varies widely between implantation (hundreds of MeV) and decay (few MeV) events. In order to be able to measure the decay energies precisely, the active stopper uses preamplifiers with a response curve that starts linearly, then levels off logarithmically (shown schematically in fig. 3.4). A precise energy calibration (as described in section 3.4 below) is only done in the linear region. In the logarithmic region, gain matching is employed: the primary beam is fed through to the stopper, creating a sharp energy peak in each detector strip. The calibration consists of choosing a gain for each strip such that the peaks line up.

Let us assume that the implantation rate per pixel is low compared to the lifetime of the nuclei. The identification of the parent for a decay in a given pixel can then be accomplished by finding the last implantation event for the given pixel and using the particle identification from that event to determine the kind of nucleus.

Fig. 3.5 shows a typical implantation event. In the figure, the readings from the detector strips are shown to the left and to the top of each detector; the beam enters from the top. (See fig. 2.7 for the active stopper layout.)

As can been seen, the implantation causes multiple strips to register a signal. In order to determine the implantation position more precisely, we take the strips above a certain

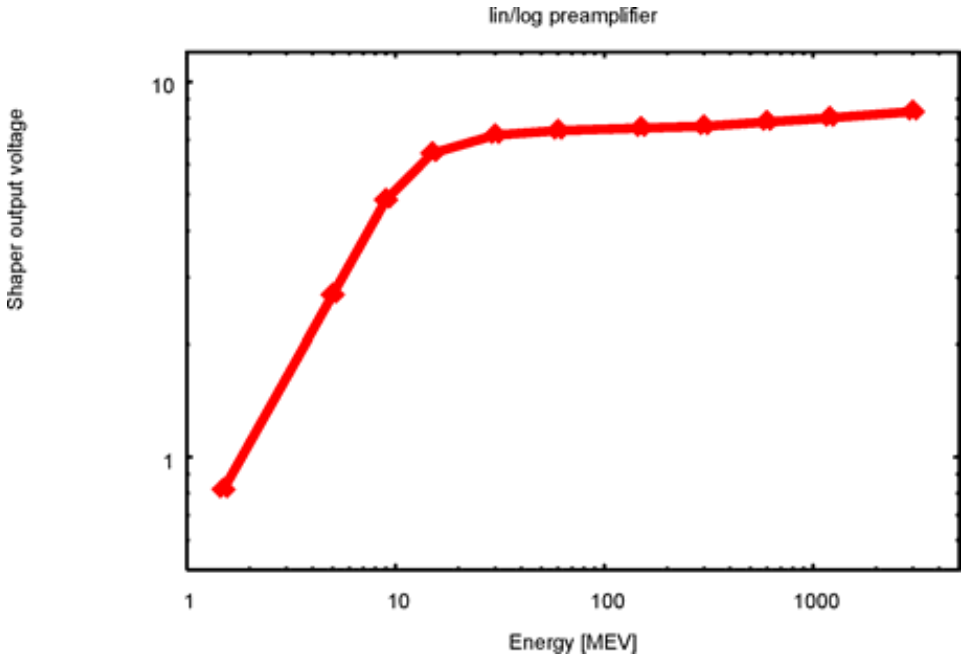

Figure 3.4: Schematic response curve of MPR-16-log Si preamplifier (taken from the manual [20]).

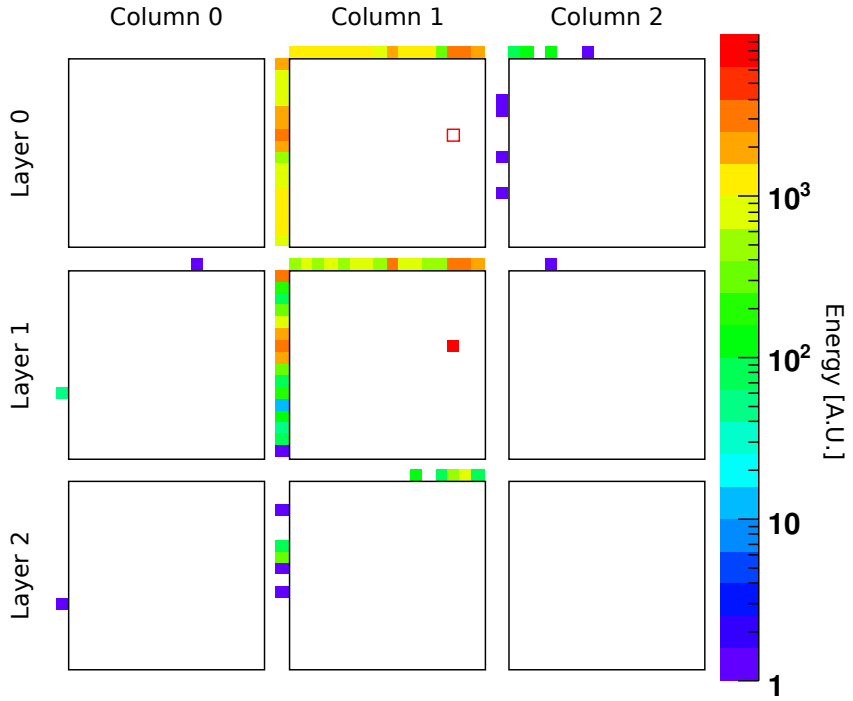

Figure 3.5: Typical implantation event (see text for explanation).

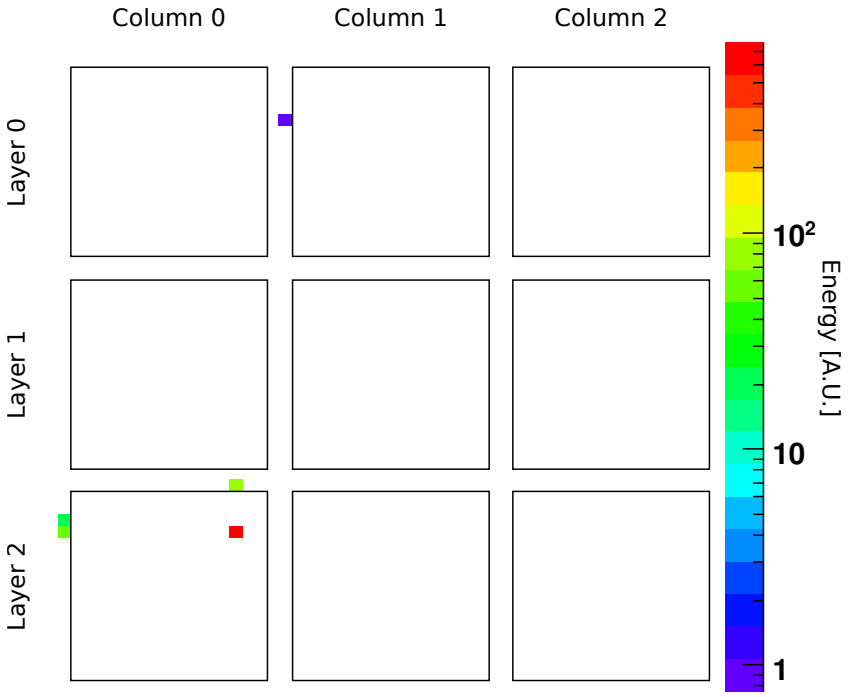

Figure 3.6: Decay event.

energy threshold and group them into clusters, then use the center of gravity of each cluster as the implantation position.

Obviously, implantations in the middle and end layers (layers 1 and 2) will generate *shoot-through* events in the preceeding layers, which need to be ignored. The algorithm simply deletes clusters which lie approximately in front of a cluster in a deeper layer. In fig. 3.5, the filled red box indicates the implantation position as determined by the algorithm; the hollow red box corresponds to a shoot-through event which was ignored.

Fig. 3.6 shows a decay event. (The figure is oriented in the same way as fig.3.5.) As can be seen, the decay event deposits less energy and involves less detector strips, making determination of its position easier. (The very low energy seen in the middle top detector is most likely due to electronic noise.) We distinguish between implantation and decay events by the trigger type, as discussed in section 2.7.

Finally, implantation and decay events need to be matched up for implantation-decay correlation. We keep, for each pixel, a record of the most recent implantation event and the associated particle identification. If a decay event happens in that pixel, we write the particle identification to the data stream. This allows, in later analysis, to gate on the decay of a certain nucleus.

It should be noted that implantation-decay correlation is far from perfect. For the "busy" pixels in the stopper, the average time between implantations is not necessarily small compared to the decay time. This means that more than one "active" nucleus

rests inside a given one of these pixels, and thus the assumption that the most recently implanted one is the parent responsible for a decay is no longer valid. This problem can be solved by ignoring decay events in those busy pixels. This, however, reduces statistics, so some trade-off needs to be made.

The second problem is that, as seen in fig.3.5, the energy deposit from an implantation event is rather spread out. It is therefore unrealistic to expect the determination of the implantation event to be accurate to one detector pixel. If the position of the implanted nucleus is determined incorrectly, implantation-decay correlation must fail. One might try to solve this problem by searching, for a given decay event, for the most recent implantation in a certain neighbourhood, but this would aggravate the first problem. Therefore, a tradeoff must again be made.

Lastly, not all decay events are as clean as the one shown in fig. 3.6, so determining the position of a given decay is not always easy either. As before, this problem can be reduced by filtering, but at the expense of statistics.

In summary, we must conclude that implantation/decay correlation is not completely reliable. This is not always as problematic as it sounds; in many cases, γ energies in the daughter nuclei are known from other experiments, and one can use e.g. γ-γ-correlation to get clean spectra.

3.2 Software: HDTV

As was discussed in the last chapter, R2D2 transforms listmode files into ROOT trees, but these trees still contain single events — histogramming, except for a limited number of debugging histograms, is outside the scope of R2D2.

The analysis of an experiment will usually require histograms. The content of these histograms, and the gates applied to them, will usually be highly experiment-specific. Thus, the task is left to an experiment-specific middleware. For the S352 experiment, of which this thesis is a part, the middleware was called c3po.

After histograms have been produced, the steps required to extract experimental values are again similar for most exotic beam experiments (and nuclear physics experiments in general). In principle, all these steps can be carried out directly using the ROOT toolkit [19] (which underlies R2D2 and C3PO). ROOT, however, was designed for particle physics, not nuclear physics. While all required analysis can, of course, be done in ROOT, it is often more cumbersome than it needs to be. Therefore, a new frontend for ROOT was developed to make common analysis steps in nuclear physics easier: HDTV [21].

The HDTV project was started during my Diploma thesis [22] and used to analyze data from stable beam experiments at the Cologne Tandem accelerator. The program was inspired by an older program used at the Cologne Institute for Nuclear Physics, tv [23], but shares no code with it. During this PhD thesis, HDTV was significantly extended and improved, in particular with respect to 2d histograms ("matrices") and

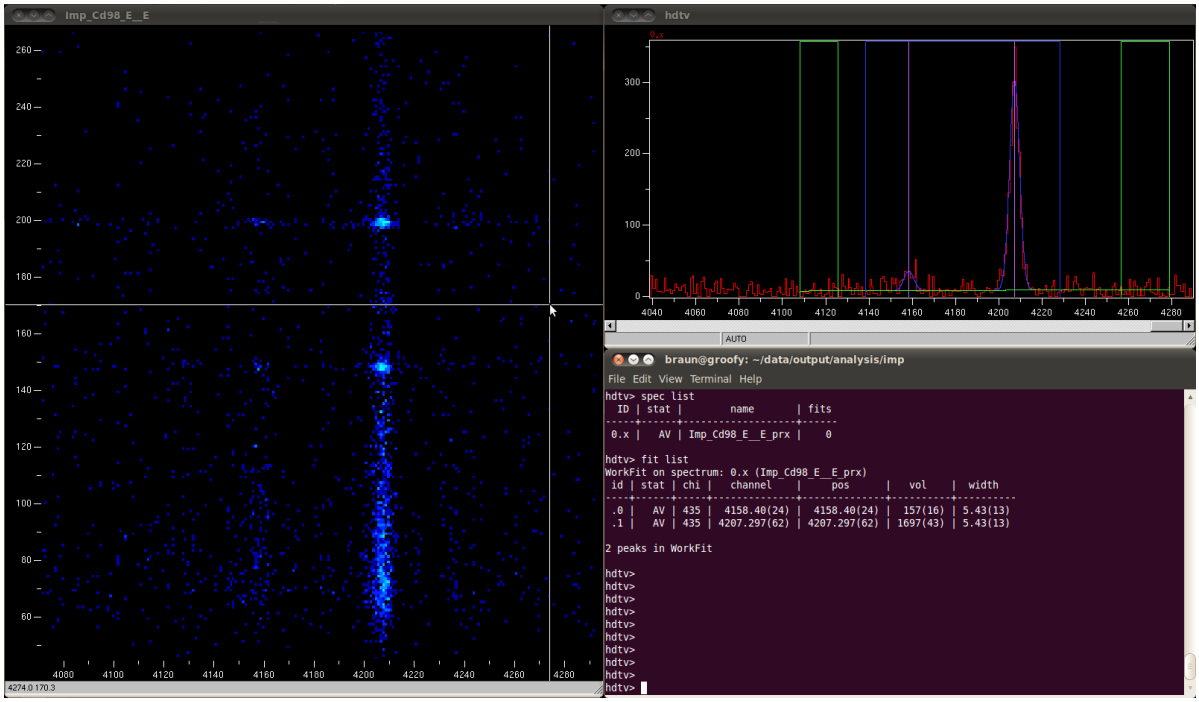

Figure 3.7: Screenshot showing HDTV being used for analysis of $\gamma\gamma$ correlation data.

ROOT integration.

Some of the features of HDTV are:

- **Smooth zooming and panning.** Histograms in nuclear physics usually have a rather high number of bins and need to be inspected at high resolution. HDTV lets the user zoom and pan (move around) in a histogram effortlessly, both for 1d and 2d histograms.

- **Peak fitting.** In nuclear physics, it is common to choose the fitting ranges for peaks and background manually, from visual inspection of a histogram. The standard ROOT fitter requires the range to be read off and entered numerically, while, in HDTV, the user can easily select the range using the mouse. In addition, HDTV has sophisticated management facilities for fits, recognizing that dozens of them may be required in a given histogram.

- **2d projections.** ("cutting") Just like for peak fitting, it is common in nuclear physics to choose ranges for projection of 2d histograms onto some axis by visual inspection. HDTV allows this and also has sophisticated facilities for management of these "cuts", as, for example in $\gamma\gamma$ correlation analysis, many of them are needed.

Eu source	
121.78	^{152}Sm $2^+ \rightarrow 0^+$
244.69	^{152}Sm $4^+ \rightarrow 2^+$
344.28	^{152}Gd $2^+ \rightarrow 0^+$
778.90	^{152}Gd $3^- \rightarrow 2^+$
964.13	^{152}Sm $2_3^+ \rightarrow 2^+$
1085.91	^{152}Sm $2_3^+ \rightarrow 0^+$
1112.12	^{152}Sm $3^+ \rightarrow 2^+$
1408.01	^{152}Sm $2^- \rightarrow 2^+$

Mixed source	
80.9990	^{133}Cs $\frac{5}{2}^+ \rightarrow \frac{7}{2}^+$
122.0607	^{57}Fe $\frac{5}{2}^- \rightarrow \frac{3}{2}^-$
302.8580	^{133}Cs $\frac{3}{2}^+ \rightarrow \frac{5}{2}^+$
356.0140	^{133}Cs $\frac{1}{2}^+ \rightarrow \frac{5}{2}^+$
511.006	Positron annihilation
661.657	^{137}Ba $\frac{11}{2}^- \rightarrow \frac{3}{2}+$
846.7720	^{56}Fe $2^+ \rightarrow 0^+$
1238.2820	^{56}Fe $4^+ \rightarrow 2^+$
1771.3510	^{56}Fe $3_2^+ \rightarrow 4^+$
2015.1810	^{56}Fe $4_3^+ \rightarrow 4^+$
2034.7550	^{56}Fe $3_4^+ \rightarrow 4^+$
2598.4580	^{56}Fe $3^+ \rightarrow 2^+$
3253.4160	^{56}Fe $4_3^+ \rightarrow 2^+$

Table 3.1: γ rays used for germanium detector calibration

In conclusion, the combination of R2D2, HDTV and an experiment-specific middleware is a powerful toolchain for the analysis of exotic beam experiments. HDTV is already used by many users both inside and outside the Cologne Institute for Nuclear Physics, for the analysis of both exotic and stable beam experiments.

3.3 Calibration of the RISING array

3.3.1 Calibration sources

To calibrate the germanium detectors, two sources were used: a ^{152}Eu source and a mixed source, containing ^{56}Co, ^{57}Co, ^{137}Cs and ^{133}Ba. The calibration used γ rays from 122 keV to 1408 keV for the Eu source and from 81 keV to 3253 keV for the mixed source. For the energy calibration, the source was placed at an arbitrary position inside the array, whereas for the efficiency calibration, it was placed in the middle of the active stopper (Layer 1/Column 1 in fig. 2.7).

3.3.2 Automatic calibration

As there were 105 detectors to be calibrated, I developed an automatic calibration script. The script works in four stages (simplified):

- The first stage utilizes the ROOT peak finder (`TSpectrum::Search`) to find peaks in the spectrum.

- As the ROOT peak finder only returns the peak position with a precision of one bin, the positions are subsequently refined by non-linear fitting of the spectrum in a region around the tentative peak. We use a Gaussian peak shape with constant background. If the fit regions of two or more tentative peaks overlap, they are fitted together. If the fit goes wrong, as measured by the chisquare and by the resulting value for the peak width, the peak is rejected. This is needed because the ROOT peak finder sometimes misidentifies structures in the background as peaks.

- In the next step, we need to associate some peaks with known energies. To that end, we assume that the calibration will be almost linear. We then choose two of the peaks found before, assume that they correspond to two given energy values, and generate a candidate calibration. Using this calibration, we calculate the expected channels for all literature energies and check how close each of them is to the nearest peak found. The sum

$$\sum_{\text{peaks}} \left(c_{\text{expected}} - c_{\text{found}}\right)^2$$

  then serves as a measure for the quality of the candidate calibration. In this way, we generate linear candidate calibrations for all possible choices of two peaks, and choose the calibration with the highest value for the quality. Possible, in this context, means that there must be at least as many peaks between the two chosen ones as there are energies between the two reference energies.

- After a linear calibration has been chosen, we use it to match all literature energies to found peaks. We can then fit a calibration of a higher degree, if desired.

In reality, there are a number of caveats. First, the ROOT peak finder needs a relatively good value for the expected peak width (sigma). This is normally not a problem, as the typical resolution of Germanium detectors does not vary too widely, but means that detectors with unusually bad resolution require manual identification and special treatment. Even with the correct settings, however, it does occasionally happen that peaks are missed, either because the ROOT peak finder misses them or because they cannot be fitted properly. To account for this, we modify the sum above to exclude the worst matches. This also means that more combinations of peaks corresponding to the reference energies are now possible.

A related issue is the choice of the two reference energies which serve for the generation of the initial calibration candidates. It is clear that they must correspond to peaks that are very unlikely to be missed; otherwise, the algorithm must go wrong. It is also desirable to choose them such that there are a number of energies between them. This is because there are pathological candidate calibrations where the reference energies map to peaks that are very close. All other energies will then map to one of these peaks, and the resulting sum of squared differences will be fairly small. There are a number of ways to avoid this, e.g. somehow disallowing multiple literature energies to map to the

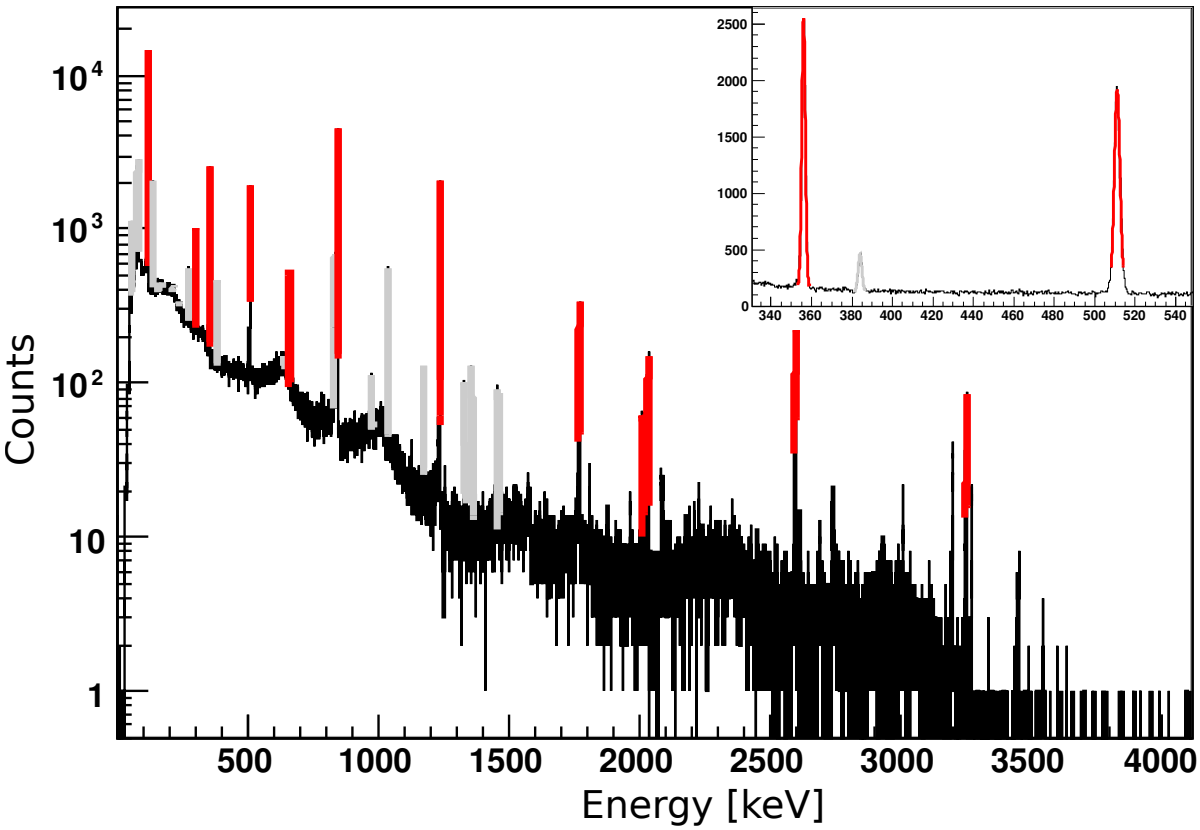

Figure 3.8: Typical energy calibration spectrum from a RISING detector (detector id 3.3), mixed source (inset shows enlarged region). Peaks used for the calibration are marked in red.

same peaks. However, we found it easiest to choose reference energies with a number of energies between them, so that the peaks corresponding to the reference energies cannot come too close together.

Fig. 3.8 shows a typical energy calibration spectrum from a RISING detector, and the fit used to extract the peak positions.

3.3.3 Technical challenges: the power supply problem

During the experiment, we experienced problems with the power supply for the germanium detector preamplifiers. The power supply would go into a bad state (with one of the supply voltages missing) regularly. Switching it off and on again cured the problem, but only temporarily, and as the power supply was inside the experimental cave, it was in the bad state during most of the experiment. However, a calibration run exists where the power supply is known to have been in the good state all the time. Thus, the influence of the bad state can be investigated.

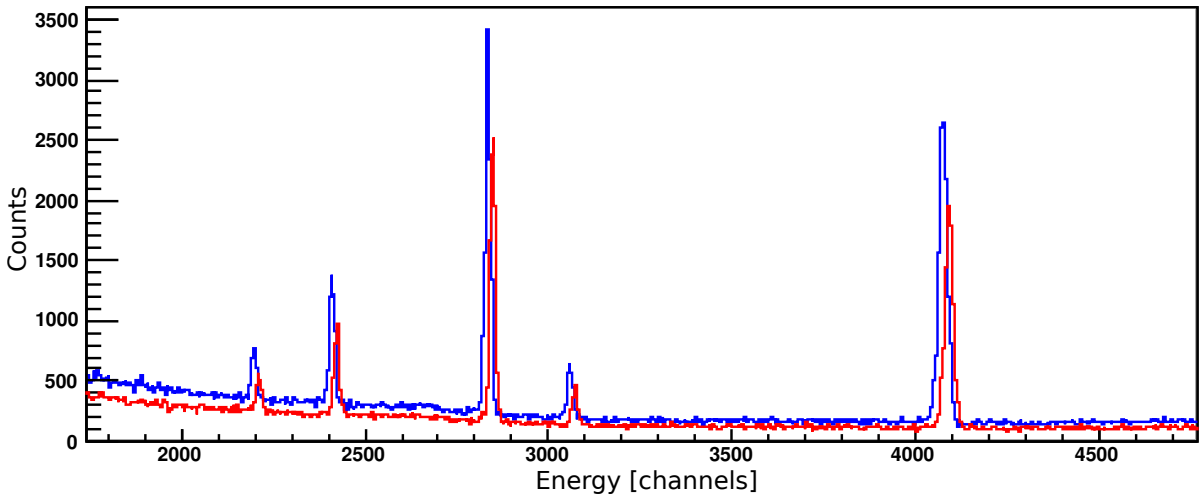

Figure 3.9: Comparison between calibration spectrum obtained in "good" (red) and "bad" (blue) preamp state for an example detector (detector id 3.3).

Fig. 3.9 shows a comparison between the mixed source calibration spectra in the "good" and the "bad" state. The most apparent effect seems to be a shift, which would be easy to compensate by a calibration. However, of much larger importance is the increased non-linearity, an effect not noted during on-line monitoring. It is seen in fig. 3.10 for an example detector. Fig. 3.11 shows the overall effect, giving the χ^2 from a linear calibration fit, histogrammed for all 99 detectors.

The non-linearity of the energy calibration is of particular concern for the ^{98}Cd part of the analysis, which focused on the properties of a newly-discovered γ transition at 4158 keV. As mentioned above, the highest energy used for the calibration is 3253 keV, meaning that some extrapolation is required. As we do not know the functional form of the non-linearity, we cannot reliably estimate the error it causes, however, a crude estimate can be obtained by comparing the differences between a linear and a third-order polynomial calibration at the energy of interest.

Fig. 3.12 shows this comparison. To obtain the values shown, we used the linear calibration to transform the energy of 4200 keV into a channel number, and the third-order calibration to transform it back. The difference between the energy thus obtained and the original energy of 4200 keV is then histogrammed. We argue that the mean of the histogram represents the effect of the non-linearity that can be compensated by using a third-order calibration for the data analysis, while the rms of the histogram represents the energy uncertainty that it causes. This means that an error of about 1 keV needs to be added to the "baseline" energy error for the newly discovered transition.

We can independently verify that this error estimate is reasonable by considering single- and double-electron escape in the detectors. These effect give rise to replicas of any γ peak occurring at a known energy below the actual peak. For the 4207 keV

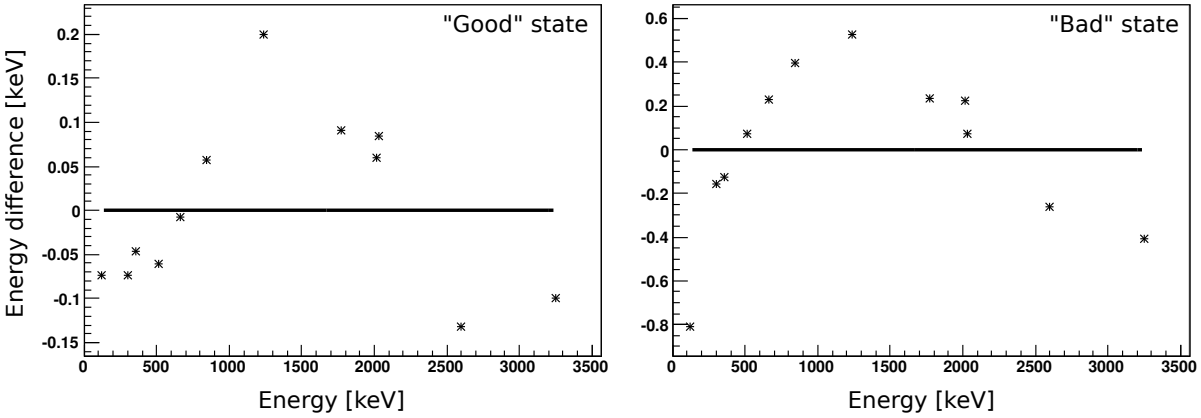

Figure 3.10: Residual from linear calibration fit for an example detector (detector id 3.3). Note different y scale.

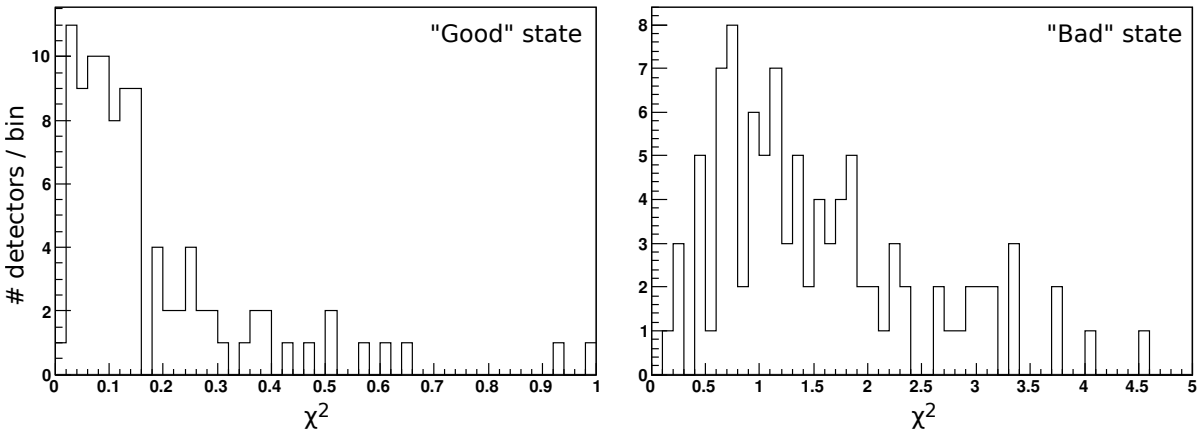

Figure 3.11: χ^2 histogrammed for all 99 detectors in a linear calibration fit, compared between "good" and "bad" states. Note different x scale.

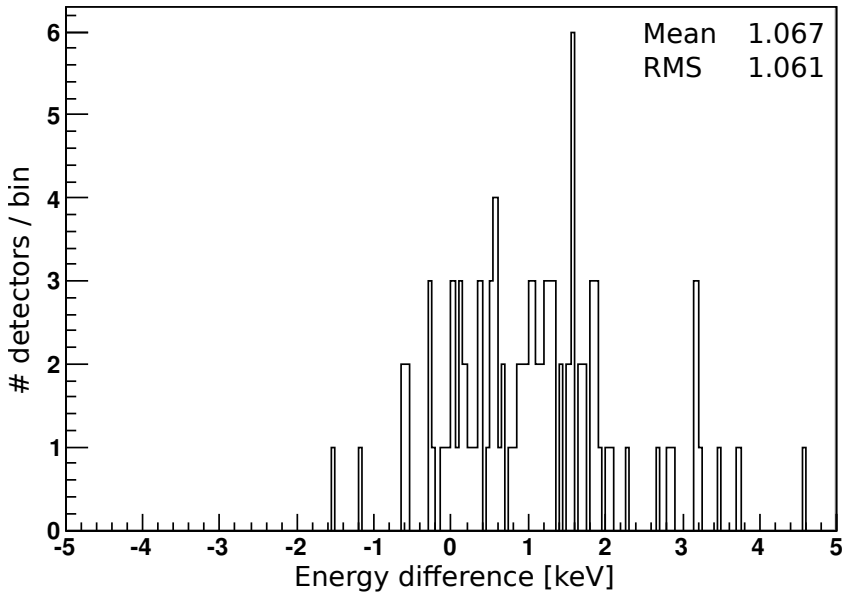

Figure 3.12: Energy difference (at 4200 keV) between linear and third-order calibration, for all detectors (see text for detailed explanation).

transition, we find

	Energy	Difference
Full-energy	4207.1 keV	
Single-escape	3696.1 keV	511.0 keV
Double-escape	3184.3 keV	$2 \cdot 511.4$ keV

Note that the double-escape peak is just about inside the region covered by the calibration (see table 3.1). Comparing the energy differences to the known electron mass of 511.00 keV, we see that our estimate of the error from extrapolating the calibration into the region of interest appears reasonable.

3.4 Calibration of the active stopper

3.4.1 Direct calibration

The most direct way to calibrate the silicon detectors is to use electrons of a known energy. To that end, we used a ^{207}Bi source. As shown in fig. 3.13, the electron capture decay of ^{207}Bi populates excited states in ^{207}Pb, and their decay releases conversion electrons from the atom. The energy of the conversion electron depends on the atomic shell from where it originates. In practice, most electrons come from either the K or the L shell, giving a doublet of peaks with known energies for each converted transition.

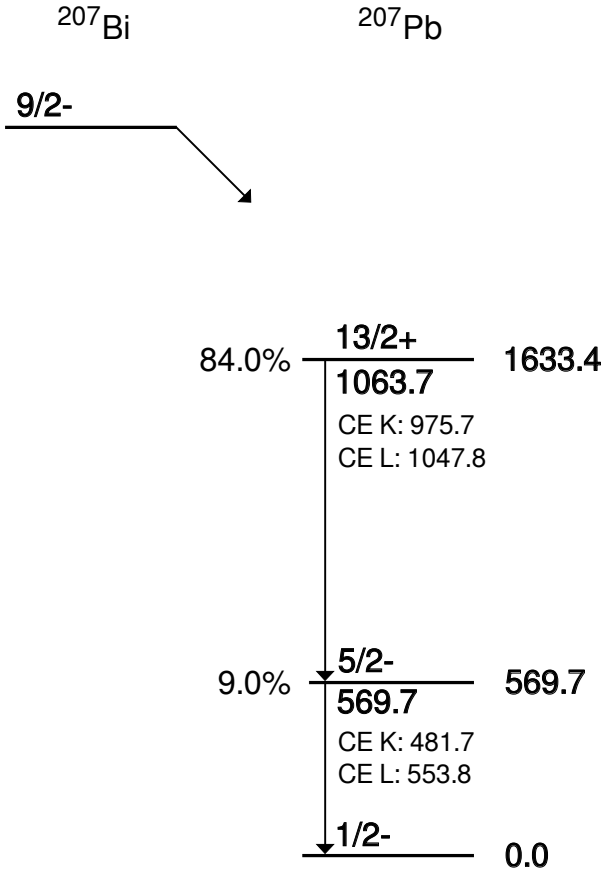

Figure 3.13: Partial decay scheme for ^{207}Bi (from [24], all energies in keV).

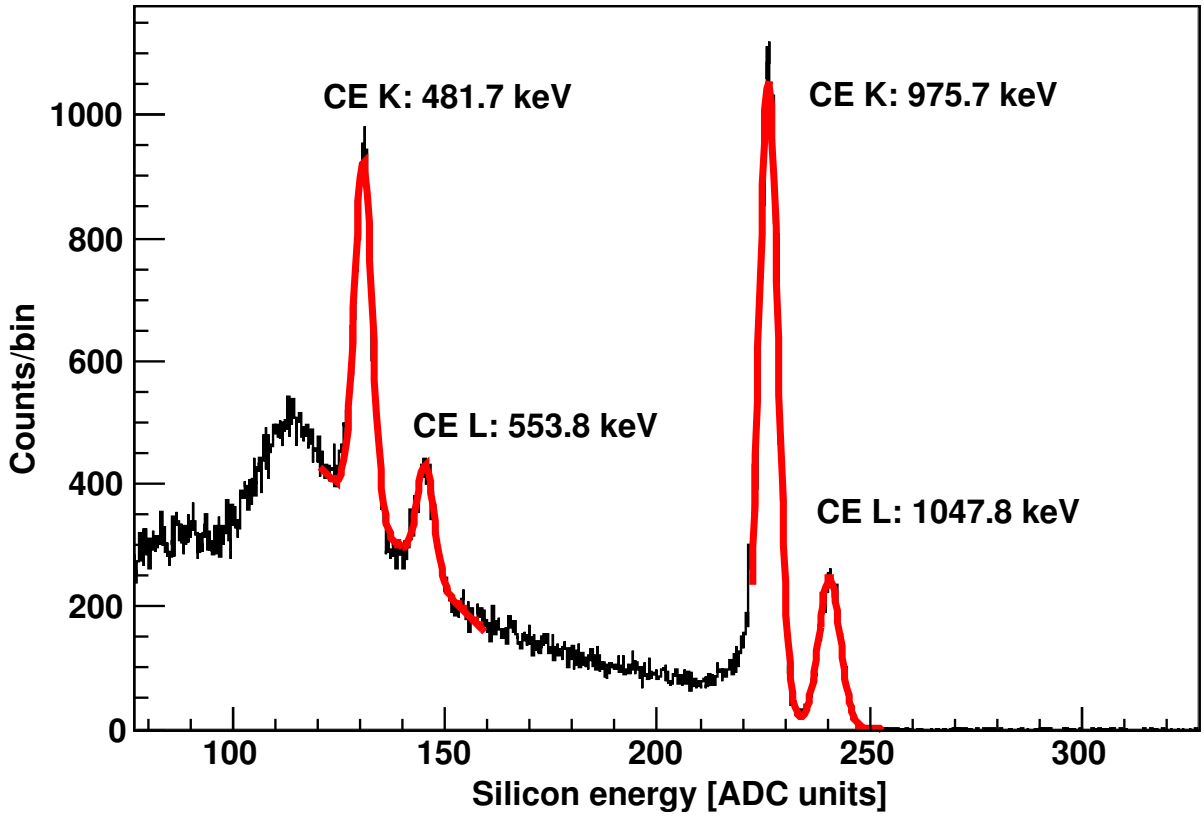

Figure 3.14: Typical spectrum used for the low-range energy calibration of the active stopper.

Fig. 3.14 shows a typical calibration spectrum thus obtained. The four peaks used for the calibration are clearly visible. As there were $9 \cdot 2 \cdot 16 = 288$ channels to calibrate, I developed a simple ROOT script to perform the calibration semi-automatically.

Note that to calibrate the innermost layer (layer 1 in fig. 2.7) with this method, either the front or the back layer has to be dismounted.

3.4.2 Compton scattering calibration

An alternative method of calibrating the silicon detectors, suggested by Thomas Faestermann [25], relies on Compton scattering. The idea is to use a γ source and look at the (rare) events where a γ quantum undergoes Compton scattering in the silicon detector and is afterwards fully absorbed in one of the germanium detectors. For these events, the sum of the energies deposited in the germanium and the silicon detectors is equal to the energy of the γ quantum. As the total energy of the γ quantum is known and the energy deposited in the germanium detector can be measured (after the germanium calibration), the energy deposited in the silicon detector can be calculated. This allows us to calibrate the energy response of the silicon detectors.

The major advantage of this method is that it can calibrate all silicon detectors at once, without needing to dismount any of them. This is because the absorption probability of a γ quantum in a single layer of silicon (thickness: 1 mm) is low and absorptions therefore occur in all layers with similar probability.

We used a ^{22}Na source for calibration. The source emits γ radiation at 1274.5 keV, plus positron annihilation radiation at 511 keV. Fig. 3.15 shows a typical calibration spectrum. The two-dimensional histogram plots germanium vs. silicon energy, with germanium energy already calibrated. The events of interest lie on diagonal lines, with one line for each γ energy emitted by the source. The horizontal lines correspond to full absorption of a γ quantum in the germanium array, with a coincident γ undergoing Compton scattering in the silicon detector. They are of no interest for the calibration.

For Compton scattering, we have

$$E_{\mathrm{ge}} + E_{\mathrm{si}} = E_\gamma \tag{3.2}$$

Assuming a linear energy calibration for the silicon detector, i.e. $E_{\mathrm{si}} = p_0 + p_1 C_{\mathrm{si}}$, we get

$$E_{\mathrm{ge}} + p_0 + p_1 C_{\mathrm{si}} = E_\gamma \tag{3.3}$$

$$E_{\mathrm{ge}} = -p_1 C_{\mathrm{si}} + E_\gamma - p_0 \tag{3.4}$$

Thus, the diagonal lines have slope $-p_1$ and y-intercept $E_\gamma - p_0$, allowing the calibration coefficients p_0 and p_1 to be extracted.

The remaining challange is to determine slope and y-intercept from the data. Standard least-square fitting methods fail, because most of the events in the histogram are outliers. A method which was found to work well takes a candidate line and sums all histogram

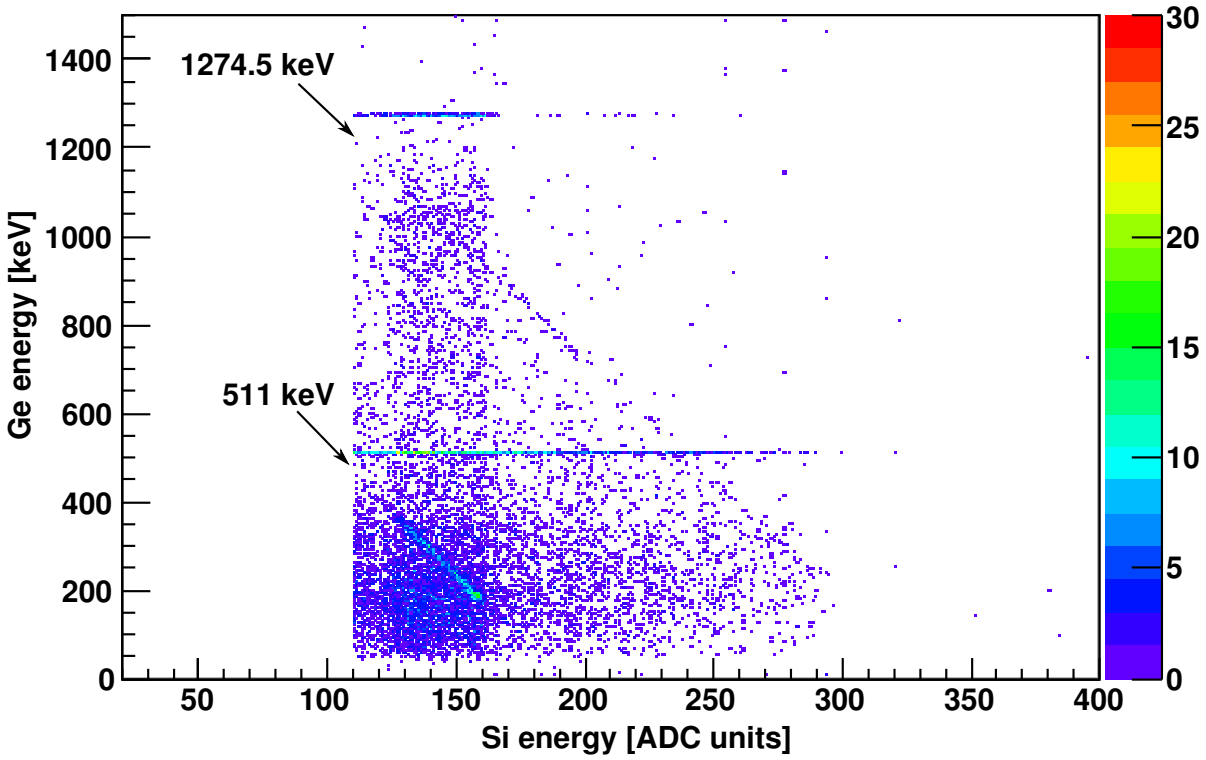

Figure 3.15: Two-dimensional histogram of germanium energy (calibrated) vs. silicon energy (uncalibrated). The diagonal lines allow for calibration of the silicon energy (see text).

bins within a certain distance of the line. After trying all possible lines, the one which gives the highest sum is taken. To exclude the horizontal lines, limits must be set on the permissible slope and y-intercept values; however, the limits can be rather coarse. It also proved advantageous to parameterize the lines with respect to a point inside the histogram rather than the origin; that point should be chosen such that it lies near the expected Compton line. Fig. 3.16 illustrates the whole calibration procedure.

3.5 Transition probabilities

We define the reduced transition probability by (eq. (2.91) in [26])

$$B(\lambda, j_i \to j_f) = \sum_{\mu, m_f} |\langle j_f m_f | \mathcal{M}(\lambda, \mu) | j_i m_i \rangle|^2 \tag{3.5}$$

where $\mathcal{M}(\lambda, \mu)$ is, for electric radiation, (eq. (2.87) in [26])

$$\mathcal{M}(E\lambda, \mu) = e r^\lambda Y^\star_{\lambda,\mu} \tag{3.6}$$

It is customary to give $B(E\lambda, \mu)$ in units of $e^2\mathrm{fm}^{2\lambda}$.

The transition probability (units: time^{-1}) T is given by (eq. (2.90) in [26][1])

$$T(\lambda; j_i \to j_f) = \frac{8\pi(\lambda+1)}{\lambda((2\lambda+1)!!)^2} \frac{1}{4\pi\epsilon_0} \frac{1}{\hbar} \left(\frac{\omega}{c}\right)^{2\lambda+1} B(\lambda, j_i \to j_f) \tag{3.7}$$

For $B(E\lambda, j_i \to j_f)$, and substituting $\omega = E/\hbar$, we get

$$\begin{aligned} T(E\lambda; j_i \to j_f) &= \frac{8\pi(\lambda+1)}{\lambda((2\lambda+1)!!)^2} \frac{1}{4\pi\epsilon_0} \frac{1}{\hbar} \left(\frac{E}{\hbar c}\right)^{2\lambda+1} B(E\lambda, j_i \to j_f) && (3.8) \\ &= k_{E\lambda} E^{2\lambda+1} B(E\lambda, j_i \to j_f) && (3.9) \end{aligned}$$

Table 3.2 gives the numerical value of the prefactor for various λ.

Table 3.2: Values of $k_{E\lambda}$ (from eq. 3.9) for various λ

$E\lambda$		$k(E\lambda)$
k_{E1}	$1.59 \cdot 10^{15}$	$\mathrm{s}^{-1}/(\mathrm{MeV}^3 e^2 \mathrm{fm}^2)$
k_{E2}	$1.23 \cdot 10^{9}$	$\mathrm{s}^{-1}/(\mathrm{MeV}^5 e^2 \mathrm{fm}^4)$
k_{E3}	$5.71 \cdot 10^{2}$	$\mathrm{s}^{-1}/(\mathrm{MeV}^7 e^2 \mathrm{fm}^6)$
k_{E4}	$1.70 \cdot 10^{-4}$	$\mathrm{s}^{-1}/(\mathrm{MeV}^9 e^2 \mathrm{fm}^8)$

A rough estimate of $B(E\lambda)$ can be obtained from the *Weisskopf estimate*. It is given by (eq. (2.103a) in [26])

$$B^W(E\lambda) = \frac{1}{4\pi} \left(\frac{3}{\lambda+3}\right)^2 e^2 R_0^{2\lambda} \tag{3.10}$$

[1] Note that [26] uses units where $\frac{1}{4\pi\epsilon_0} \equiv 1$, so this factor does not appear there.

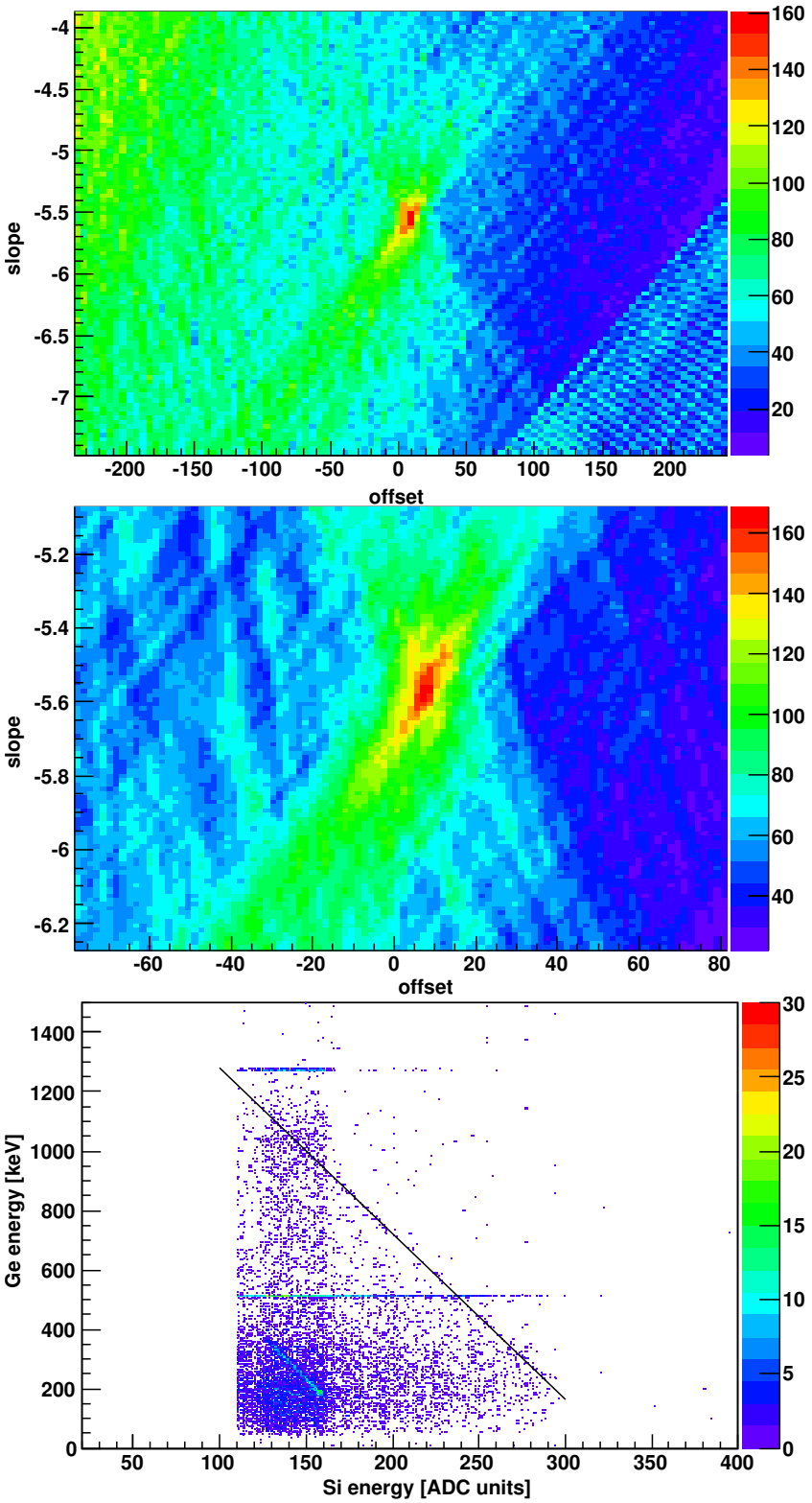

Figure 3.16: Demonstration of the Compton line-finder: (a) Scan of the histogram in fig. 3.15. For each (slope, y-intercept) pair, the sum of bin contents near the candidate line is shown. (b) Zoom, showing the sharpness of the peak. This allows the line parameters to be extracted with high precision. (c) Resulting line superimposed on the histogram.

where R_0 is the nuclear radius. Further setting

$$R_0 = 1.2\text{fm} \cdot A^{1/3} \tag{3.11}$$

we get (eq. (2.103b) in [26])

$$B^W(E\lambda) = \frac{1}{4\pi}\left(\frac{3}{\lambda+3}\right)^2 (1.2)^{2\lambda} A^{2\lambda/3} \tag{3.12}$$

in units of $e^2\text{fm}^{2\lambda}$.

The dimensionless quantity

$$b = \frac{B(E\lambda)}{B^W(E\lambda)} \tag{3.13}$$

is called the reduced transition probability in Weisskopf units and given the "unit symbol" W.u. .

If there are multiple transitions which depopulate a given level, their transition probabilities add up. Of particular interest for us is the case where de-excitation via γ rays competes with de-excition via internal conversion. We define the internal conversion coefficient

$$\alpha = \frac{T_e}{T_\gamma} \tag{3.14}$$

where T_e is the transition probability for de-excitations via conversion electron emission, and T_γ is the transition probability for de-excitations via γ ray emission. The total transition probability is given by

$$T_{\text{tot}} = T_e + T_\gamma \tag{3.15}$$

Thus, if the total transition probability and the internal conversion coefficient are known, one can calculate the γ transition probability via

$$T_\gamma = \frac{T_{\text{tot}}}{1+\alpha} \tag{3.16}$$

3.6 Halflife determination

For the lifetime of an excited state, an exponential decay starting at $t = 0$ is assumed. The probability density for a decay at time t is then

$$f(t) = \lambda\,\theta(t)\,e^{-\lambda t} \tag{3.17}$$

where

$$\theta(t) = \begin{cases} 0 & : \quad t < 0 \\ 1 & : \quad t \geq 0 \end{cases} \tag{3.18}$$

is the Heaviside step function.

The moments of this probability density are

$$\int_{-\infty}^{\infty} \mathrm{d}t\ f(t) = 1 \tag{3.19}$$

$$\int_{-\infty}^{\infty} \mathrm{d}t\ t \cdot f(t) = \frac{1}{\lambda} \tag{3.20}$$

The first equation reflects the obvious fact that the excited state needs to decay somewhen, whereas the second equation states that the mean lifetime τ is given by

$$\tau = \frac{1}{\lambda} \tag{3.21}$$

We can also consider the probability $F(T)$ that the state has decayed at time T. This is given by

$$F(T) = \int_{-\infty}^{T} \mathrm{d}t\ f(t) = 1 - e^{-\lambda T} \tag{3.22}$$

The half-life $t_{1/2}$ is defined by $F(t_{1/2}) = \frac{1}{2}$ and thus related to τ and λ via

$$t_{1/2} = \frac{\ln(2)}{\lambda} = \ln(2)\tau \tag{3.23}$$

Of course, in a typical experiment, many occurrences of the decay of some excited state are observed, so $f(t)$ must be properly normalized. If the timing resolution of the detector is small compared to the mean lifetime τ, τ can simply be extracted by fitting an exponential to the decay time histogram (possibly with an additive constant to model the background). If, however, the mean lifetime is smaller than or roughly equal to the detector timing resolution, this method can no longer be used.

Let $g(t)$ be the prompt response of the detector, i.e. the probability density that an event that occurred at time 0 is registered at time t. We assume that $g(t)$ is normalized. The observed decay probability density is then given by the convolution of the true decay probability density and the prompt detector response (see fig. 3.17), i.e.

$$c(t) = \int_{-\infty}^{\infty} \mathrm{d}t'\ f(t')\, g(t - t') \tag{3.24}$$

The zeroth moment of c,

$$\begin{aligned} \int_{-\infty}^{\infty} \mathrm{d}t\ c(t) &= \int_{-\infty}^{\infty} \mathrm{d}t \int_{-\infty}^{\infty} \mathrm{d}t'\ f(t')\, g(t - t') \\ &= \left(\int_{-\infty}^{\infty} \mathrm{d}t\ f(t)\right) \cdot \left(\int_{-\infty}^{\infty} \mathrm{d}t\ g(t)\right) = 1 \end{aligned} \tag{3.25}$$

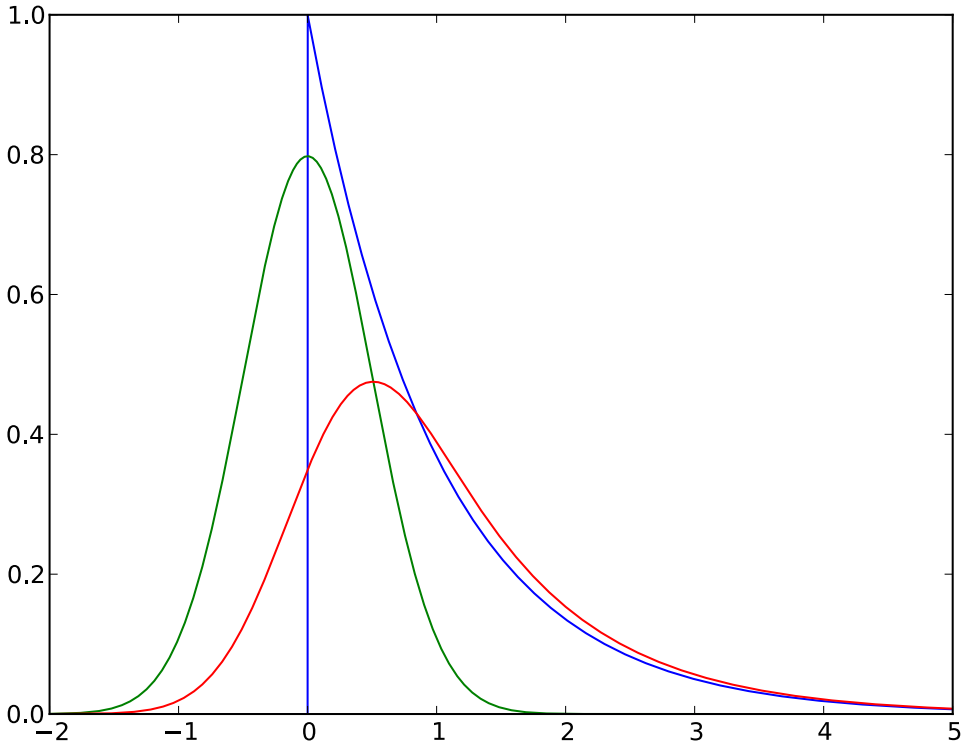

Figure 3.17:]
The decay curve (blue) is convolved with the detector response (green) to produce the observed decay curve (red).

is equal to one as expected; every decay is detected, even with the delay. The first moment is just the sum of the first moments of $f(t)$ and $g(t)$ (assuming they are normalized).

$$\begin{aligned}\int_{-\infty}^{\infty} \mathrm{d}t\; t \cdot c(t) &= \int_{-\infty}^{\infty} \mathrm{d}t \int_{-\infty}^{\infty} \mathrm{d}t'\; t\, f(t')\, g(t-t') \\ &= \int_{-\infty}^{\infty} \mathrm{d}t\; t f(t) \cdot \int_{-\infty}^{\infty} \mathrm{d}t\; g(t) + \int_{-\infty}^{\infty} \mathrm{d}t\; f(t) \cdot \int_{-\infty}^{\infty} \mathrm{d}t\; t g(t) \\ &= \int_{-\infty}^{\infty} \mathrm{d}t\; t f(t) + \int_{-\infty}^{\infty} \mathrm{d}t\; t g(t)\end{aligned} \tag{3.26}$$

This observation forms the basis of the *centroid shift method*. If we can measure the first moments of $g(t)$ and $c(t)$, we can calculate the first moment of $f(t)$, which, if $f(t)$ is of the exponential form given above, directly yields the mean lifetime.

4 Experimental results

4.1 Particle identification

As discussed in section 3.1.5, particle identitication (PID) forms the first step in the analysis. By combining measurements from the FRS detectors in suitable ways, we can determine A/q (mass over charge) and Z (nuclear charge) on an event-by-event basis, allowing to identify each nucleus individually. Fig. 4.1 shows the resulting histogram. By gating, i.e. selecting only events identified as a given particle, we can electronically select certain isotopes for further analysis.

After the particle identification step, the common analysis effort ends. Data pertaining to the different isotopes were analyzed by different groups. In this work, I discuss ^{98}Cd and ^{98}Ag. In total, approximately $3.9 \cdot 10^5$ ^{98}Cd and $4.0 \cdot 10^4$ ^{98}Ag nuclei were observed during 192 h of beam on target.

4.2 ^{98}Cd

4.2.1 γ transitions

Using the particle identification described above, it is possible to examine γ rays emitted shortly after implantation of a ^{98}Cd nucleus in the active stopper. Fig. 4.2 shows a histogram of γ energies observed at a given time after the implantation. The most prominent feature is the *prompt flash*, caused by bremsstrahlung as the particles hit the stopper and the scintillator before it.

Fig. 4.3 shows a projection of fig. 4.2 on the energy axis, allowing us to determine the energy of the transitions via fitting of a Gaussian plus background.

Earlier studies of ^{98}Cd ([27], [28]) found five transitions and deduced a level scheme of the nucleus as shown in Fig. 4.6. All these transitions could be confirmed in our experiment (table 4.1). The errors given in the table are only statistical (fitting) errors, which are very low. Of course, the total error is dominated by the systematic error due to uncertainties in the detector energy calibration. Following the discussion in sect. 3.3.3, a total error of about 1 keV seems reasonable.

Note that the good correspondence between the energies in [28] and the energies in this work provides further support for the claim that our estimate of the total error is reasonable.

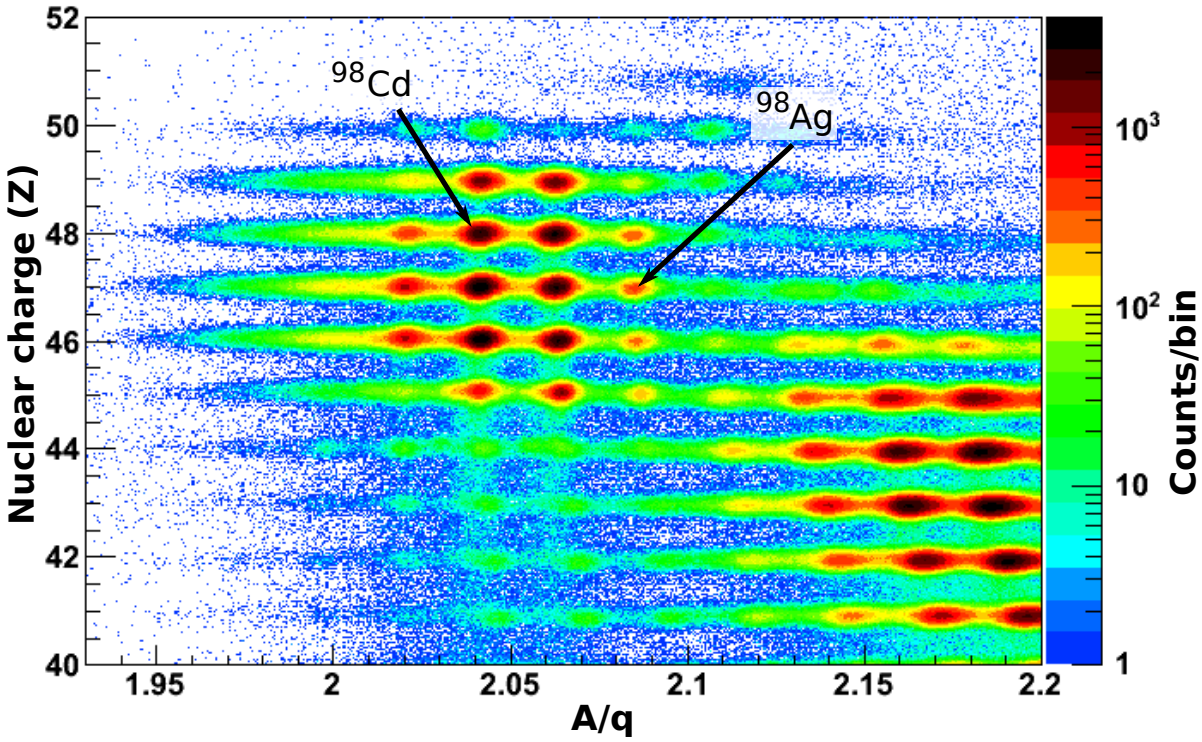

Figure 4.1: Particle identification.

Table 4.1: γ transitions in ^{98}Cd. The errors given are statistical (fitting) errors, the systematic error due to uncertainties in the calibration is much larger (approx. 1 keV, see text). The 49 keV transition was not observed directly; the energy given is the difference between the 4207 keV and the 4158 keV transitions (see text).

This work	[28]	Assigned transition
48.64(39)	—	$(12^+)\rightarrow(10^+)$
148.339(19)	147	$(8^+)\rightarrow(6^+)$
199.175(14)	198	$(6^+)\rightarrow(4^+)$
688.069(18)	688	$(4^+)\rightarrow(2^+)$
1395.260(25)	1395	$(2^+)\rightarrow 0^+$
4207.10(11)	4207	$(12^+)\rightarrow(8^+)$
4158.46(37)	—	$(10^+)\rightarrow(8^+)$

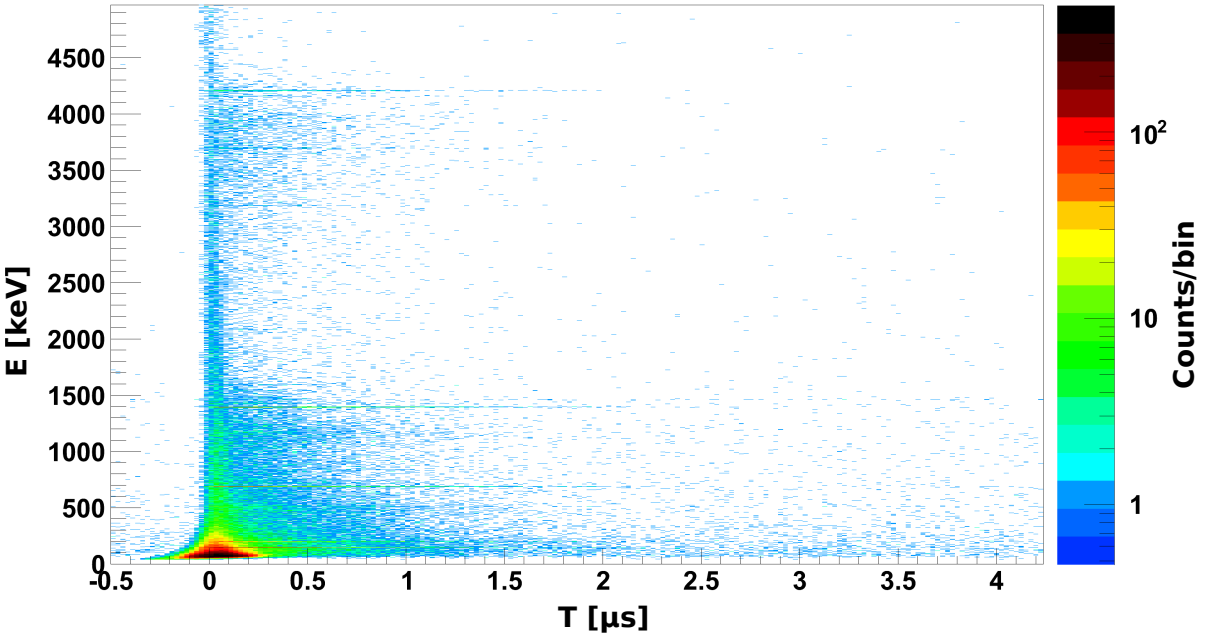

Figure 4.2: Histogram showing γ rays observed vs. time after implantation (gate on ^{98}Cd particle id).

4.2.2 Transition at 4158 keV

Besides the known transitions, a previously unknown transition at an energy of 4158 keV is visible in the data (see fig. 4.3 and table 4.1).

In order to clarify the position of the new transition in the ^{98}Cd level scheme, γ-γ coincidences were studied. Fig. 4.4 shows the prompt coincidence spectrum, gated on the new 4158 keV transition. The coincidence with the four lower transitions of the level scheme is clearly seen. We do not observe a coincidence with the 4207 keV transition, but we would hardly see it even if it was there, as the efficiency for $\gamma\gamma$ correlations at these energies gets too low. In addition, the 4207 keV transition was also found to be coincident with the four lower transitions, confirming the result from [28] (not shown).

Furthermore, the prompt time spectrum was investigated, which gives the time after implantation when a γ ray with a certain energy was seen. Fig. 4.5 shows the result for both the 4207 keV and the new 4158 keV transition. The fitted curve (an exponential decay) gives

E_γ [keV]	$t_{1/2}$ [μs]
4207	0.252(13)
4158	0.26(4)

As can be seen, the half-lifes are identical within the errors.

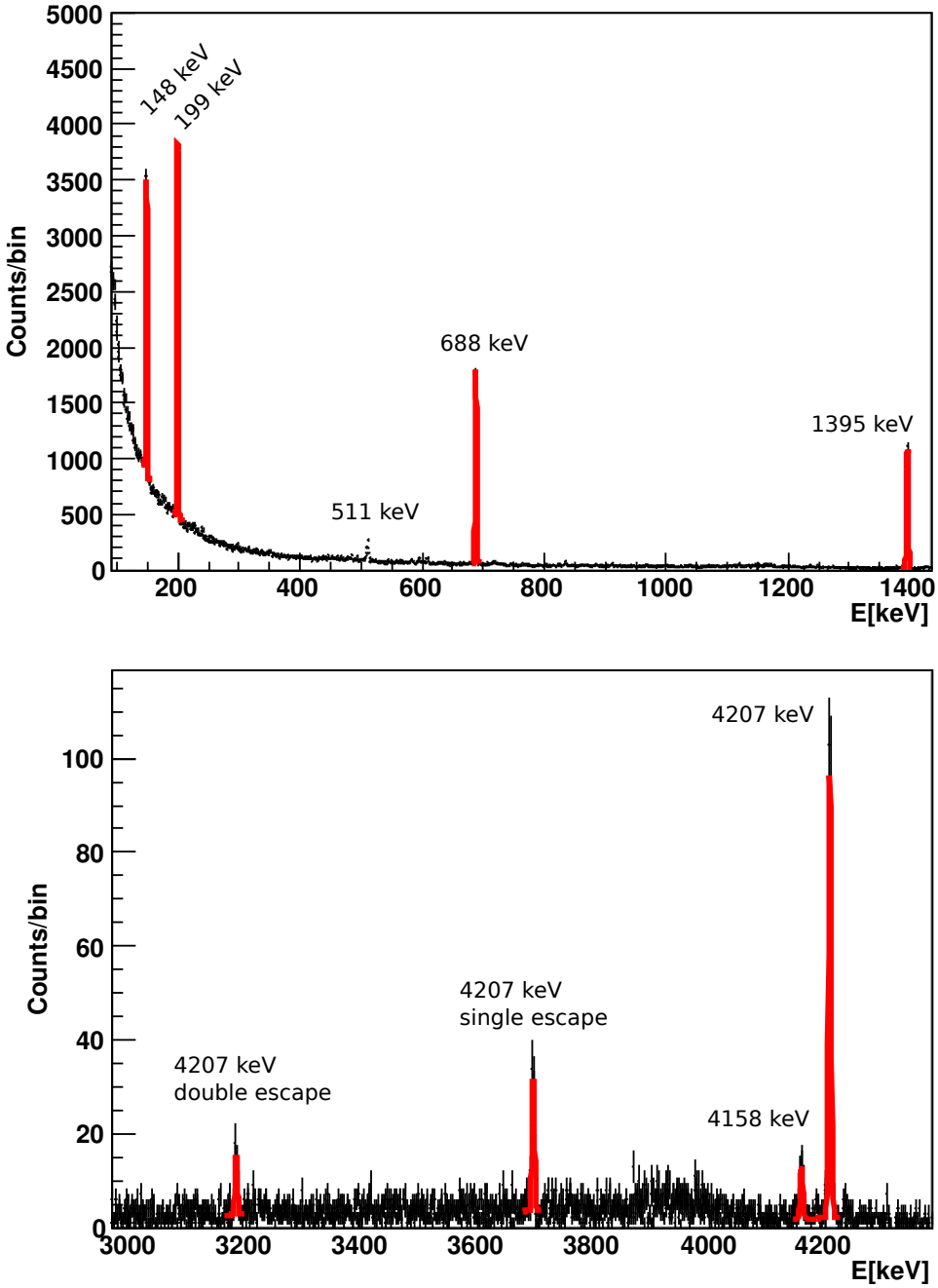

Figure 4.3: Sum spectrum (all Ge detectors, gate on ^{98}Cd particle id).

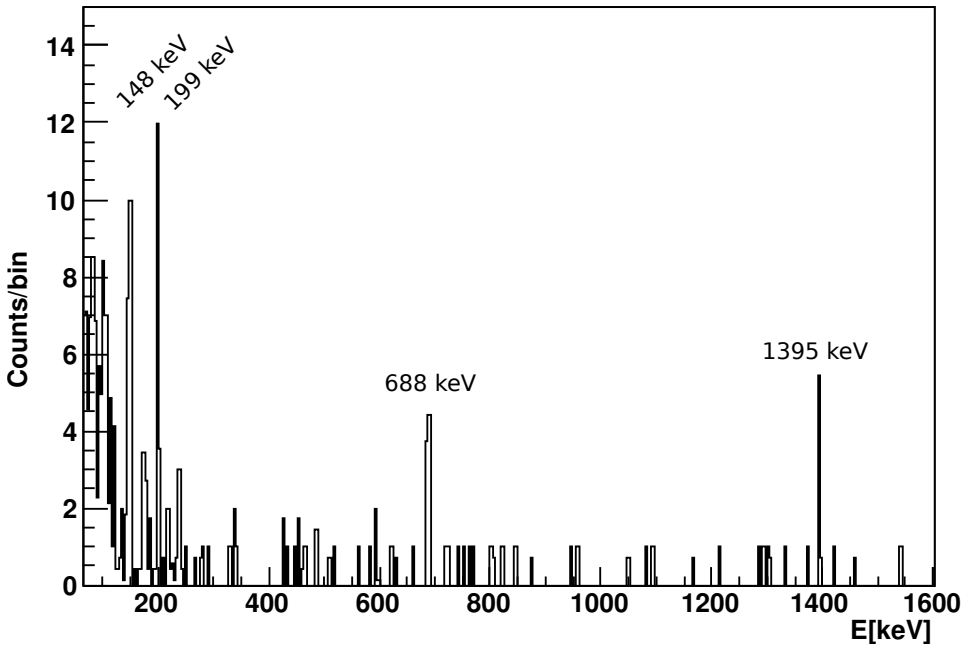

Figure 4.4: $\gamma\gamma$ coincidence spectrum (cut on 4158 keV, ^{98}Cd particle id).

Based on these observations, a position for the new 4158 keV transition in the ^{98}Cd level scheme needs to be found. Having the 4158 keV transition above or below the 4207 keV transition seems highly unlikely for nuclear structure reasons. The (0^+), (2^+), (4^+), (6^+) and (8^+) levels are interpreted as different couplings of the two valence protons (see section 5.2.2 for a detailed explanation). For higher spin states, a particle (proton or neutron) needs to be lifted across the shell gap to produce a particle-hole pair. This explains the large gap between the (8^+) and the (12^+) state, but cannot account for another gap of similar size.

In [28], the 4207 keV transition is assumed to be an E4 transition connecting a (12^+) and an (8^+) state, which explains the observed long lifetime (100s of ns). If the 4158 keV transition would be an E2 transition directly depopulating the (12^+) state, the lifetime should be much shorter, and the 4207 keV transition should be too strongly hindered to be observed at all. Thus, an intermediate (10^+) level is assumed to exist directly below the (12^+) state, which is in turn depopulated by the new 4158 keV transition to the (8^+) state. This proposal is shown in fig. 4.6.

In the proposed level scheme, the 4158 keV transition is parallel to the 4207 keV transition. This requires the existence of another new transition at 49 keV. Unfortunately, this transition could not be observed in our experiment, as the efficieny of the γ detectors at that energy is already too low, and a 49 keV E2 transition is highly converted (i.e. most transitions happen via the emission of conversion electrons, which could not be measured in our experiment) with a conversion coefficient $\alpha = 19.6(3)$ (see below).

This assumption gives rise to an interesting situation, where the upper level (6638 keV,

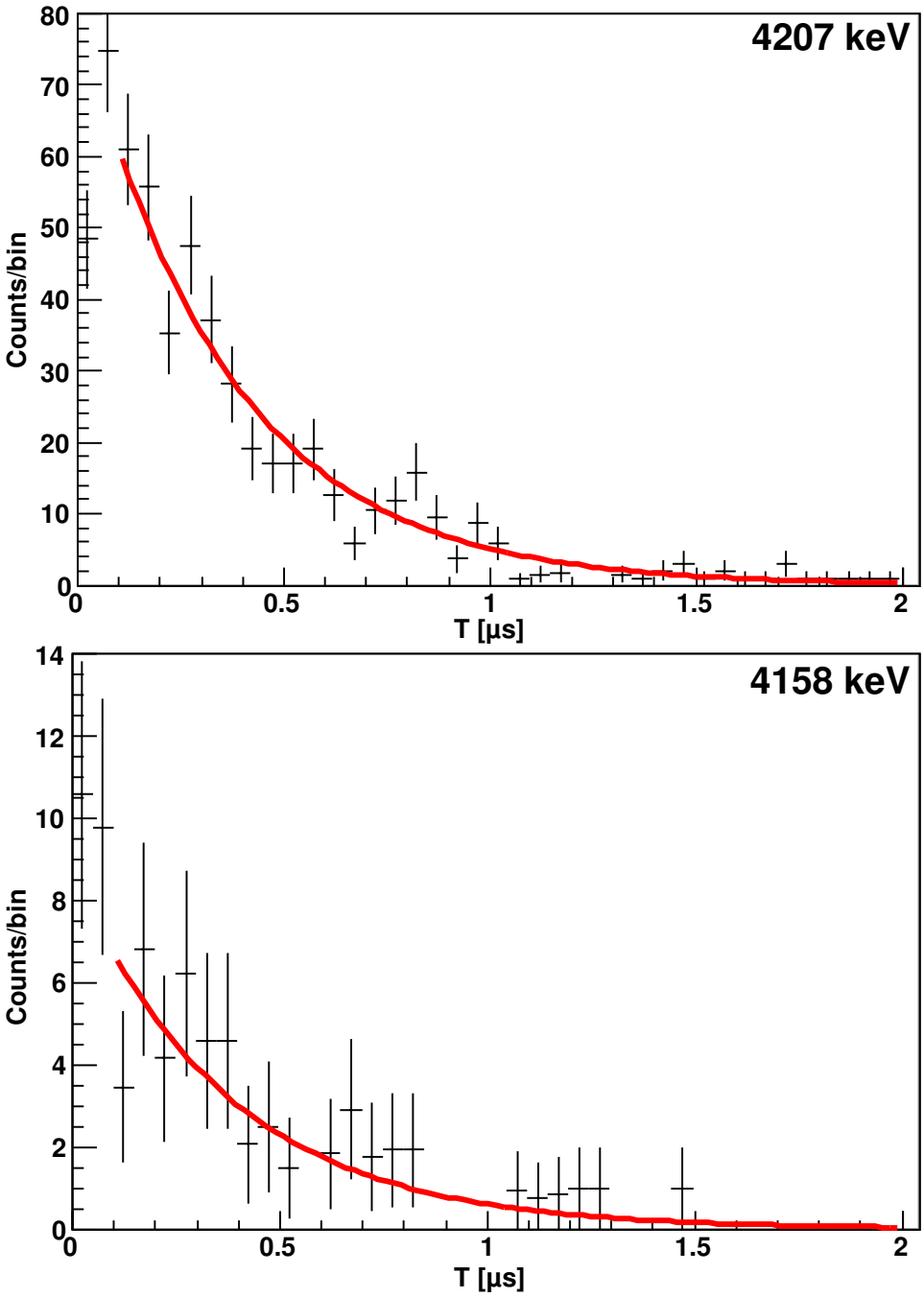

Figure 4.5: Decay of transition γ rays after ^{98}Cd implantation.

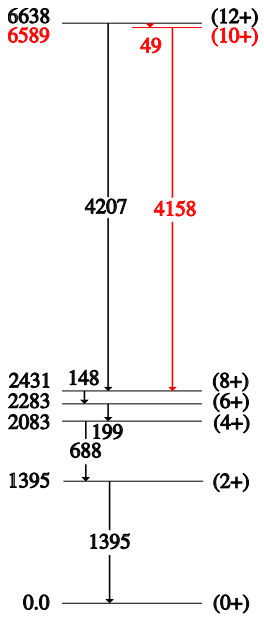

Figure 4.6: Level scheme for ^{98}Cd, as established in [28], and extension (shown in red) proposed to explain the results of the present experiment.

(12^+)) is depopulated by an E4 transition to the 2431 keV (8^+) level, as well as by an E2 transition to the intermediate level (6589 keV, (10^+)). Naively, the E4 transition would be expected to be strongly hindered compared to the E2 transition, but the transition energy is also much higher. As will be shown in the calculation below, these effects mostly cancel out. Of course, the 4158 keV E2 transition has a much higher transition rate, but this only means that all the initial population of the intermediate state has decayed by the time the nuclei reach the stopper. All population of the intermediate state must come from the upper state, so we really conclude the existence of the 49 keV transition via observation of the 4158 keV transition.

The assumption is able to explain the identical lifetimes for the 4207 keV and the 4158 keV transitions as well as the fact that they are both observed (i.e. have comparable intensities).

In the text that follows, the level scheme in fig. 4.6 will be assumed to be correct, in particular with respect to the 49 keV transition.

4.2.3 Intensity balance

We wish to determine the branching ratio of the two γ transitions depopulating the level at 6638 keV. Normalization of γ intensities would normally require an efficiency calibration to compensate for the fact that the efficiency of HPGe detectors is highly energy dependent. However, as the two transitions are very close together, we can assume that the efficiency is constant, considering the typical efficiency curve of a large

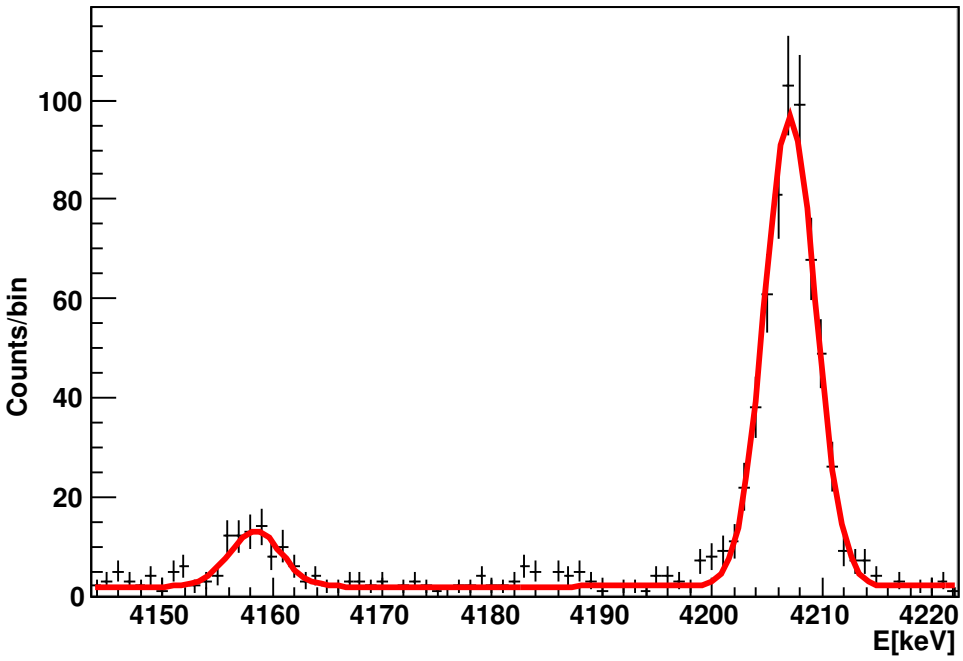

Figure 4.7: Fit used to determine the relative intensities of the 4207 keV and 4158 keV transitions. (Note that the fit is constrained to use the same width for both peaks.)

volume HPGe detector. The error of the branching ratio will still be dominated by the errors of the peak volumes.

Using the fit in figure 4.7, we find

E_γ [keV]	I_γ [counts]
4158	65.2(93)
4207	556(24)

which gives an intensity ratio

$$\frac{I_{4158}}{I_{4207}} = 0.117(17)$$

In the next step, $B(Ex)$ values for the 4207 keV and the 49 keV transitions must be determined. The situation is slightly more complex than usual (see fig. 4.8). Essentially, the upper state (tentative 12^+) is depopulated by two γ transitions to the (10^+) and (8^+) states, plus, due to the small energy difference to the intermediate (10^+) state, by conversion electrons. Both transitions to the (10^+) state (γ and conversion electrons) cannot be directly observed in our experiment.

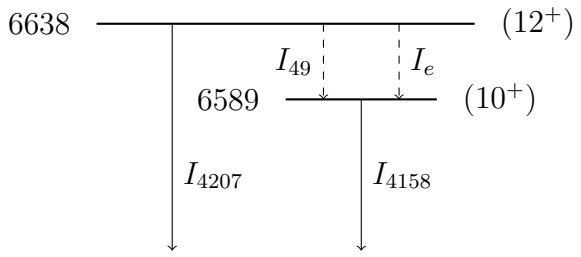

Figure 4.8: γ transitions and electronic conversion depopulating the excited state at 6638 keV in ^{98}Cd. Dashed transitions are not observed directly (see text for discussion).

The conversion coefficient for the 49 keV transition is given by BrIcc[1] [29] as

$$\alpha := \frac{T_e}{T_{49}} = 19.6(3) \tag{4.1}$$

(Note that the conversion coefficient is independent of the presence of further depopulating transitions, such as the 4207 keV transition).

Making the reasonable assumption that the intermediate state is depopulated only by the 4158 keV transition, we have the following relation between the partial transition probabilities T and the intensity ratio

$$\frac{T_{49} + T_e}{T_{4207}} = \frac{I_{49} + I_e}{I_{4207}} = \frac{I_{4158}}{I_{4207}} \tag{4.2}$$

In addition, the mean lifetime τ of the (12^+) state is given by

$$T_{4207} + T_{49} + T_{\mathrm{e}} =: T_{\mathrm{tot}} = \frac{1}{\tau} \tag{4.3}$$

where τ is related to the half-life $t_{1/2}$ by

$$\tau = \frac{t_{1/2}}{\log(2)} \tag{4.4}$$

These equations are solved to give

$$T_{4207} = \frac{T_{\mathrm{tot}}}{1 + \frac{I_{4158}}{I_{4207}}} \tag{4.5}$$

$$T_{49} = \frac{I_{4158}}{I_{4207}} \frac{1}{\alpha} T_{4207} \tag{4.6}$$

Numerically, using the value for $t_{1/2}$ obtained from the fit of the 4207 keV transition ($t_{1/2} = 0.252(13)$ μs), the following values for the partial transition probabilities are obtained:

[1] BrIccS v2.3 (9-Dec-2011), Z=48 (Cd, Cadmium), γ-energy: 48.64 keV, Data Sets: BrIccFO.

T_{4207}	$2.46(13) \cdot 10^6$ s^{-1}
T_{49}	$0.014(20) \cdot 10^6$ s^{-1}
T_e	$0.275 \cdot 10^6$ s^{-1}
T_{tot}	$2.75(14) \cdot 10^6$ s^{-1}

Using the equations from section 3.5,

$$\begin{aligned} &\text{4207 keV: B(E4; } 12^+ \rightarrow 8^+) = 3.51(19) \cdot 10^4\ e^2\text{fm}^8 = 2.74(15)\ \text{W.u.} \\ &\text{49 keV: B(E2; } 12^+ \rightarrow 10^+) \ = \quad 42.0(62) e^2\text{fm}^4 = 1.56(23)\ \text{W.u.} \end{aligned}$$

It needs to be stressed that the errors are purely statistical errors. The systematic errors are much larger. Significant sources of systematic error include the problems with the Germanium energy calibration and effects of the chosen fitting range on the result of the half-life fit. Trying to take the (estimated) systematic errors into account, the following is obtained:

$$\begin{aligned} &\text{4207 keV: B(E4; } 12^+ \rightarrow 8^+) = 3.5(11) \cdot 10^4\ e^2\text{fm}^8 = 2.7(9)\ \text{W.u.} \\ &\text{49 keV: B(E2; } 12^+ \rightarrow 10^+) \ = \quad 42(16) e^2\text{fm}^4 = 1.6(6)\ \text{W.u.} \end{aligned}$$

4.3 ^{98}Ag

The second nucleus of interest is ^{98}Ag, which can be studied in two ways: as a ^{98}Cd decay product, or as directly implanted. The first way will be discussed first: the decay of ^{98}Cd. This decay happens in the active stopper, so it can be detected. Implantation-decay correlation is used to select the decay of interest. γ rays produced after the decay can then be studied using the RISING array.

Table 4.2: γ transitions observed in ^{98}Ag. The errors given are statistical (fitting) errors, the systematic error due to uncertainties in the calibration is much larger (see text).

This work	[30]
62.15(12)	60.55(10)
108.394(50)	107.28(10)
347.673(38)	347.18(10)
1176.195(58)	1176.1(2)

4.3.1 γ transitions

In a previous study [30], a decay scheme of ^{98}Cd was established, as partially shown in fig. 4.9. For the present discussion, the low-lying transitions at 107 keV and 60.6 keV are of particular interest. In [30], their character and multipolarity could be established

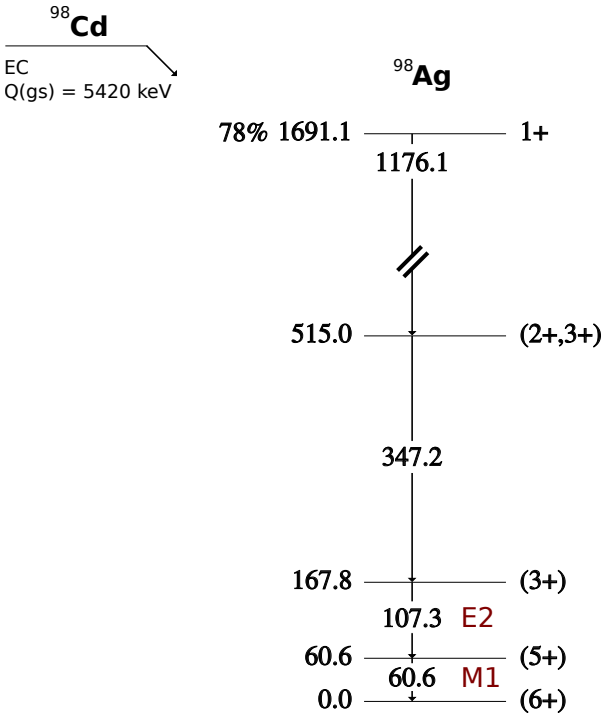

Figure 4.9: Level scheme for ^{98}Ag (from [24]).

via conversion electron spectroscopy, but the ordering could not be unambiguously be determined.

Fig. 4.10 shows the γ spectrum after a decay-implantation correlation gate on ^{98}Ag. We can further require coincidence with the 1176 keV transition. This results in the histogram shown in fig. 4.11, as expected from the level scheme in fig. 4.9.

In table 4.2, γ transitions observed in ^{98}Ag are listed. We note that the agreement with the published energies is significantly better for the two higher-energy transitions than for the low-energy ones. The most likely cause is again the Germanium preamplifier problem (ref. sect. 3.3.3), so the values in the literature are probably more accurate than the ones from this work. Therefore, in the text that follows, transitions will be referred to via the literature energies.

4.3.2 Lifetime of the 60.6 keV and 107 keV transitions

Next, we can also study the lifetimes of the transitions, using the β decay in the active stopper as a start and the germanium detector as a stop signal (fig. 4.12). We see that the 60.6 keV and 347 keV transitions have lifetimes comparable to the intrinsic resolution of the system, but the 107 keV transition has a longer lifetime. A non-linear least squares fit of an exponential decay plus constant background (fig. 4.13) gives

$$t_{1/2} = 0.142(13)\mu\text{s}$$

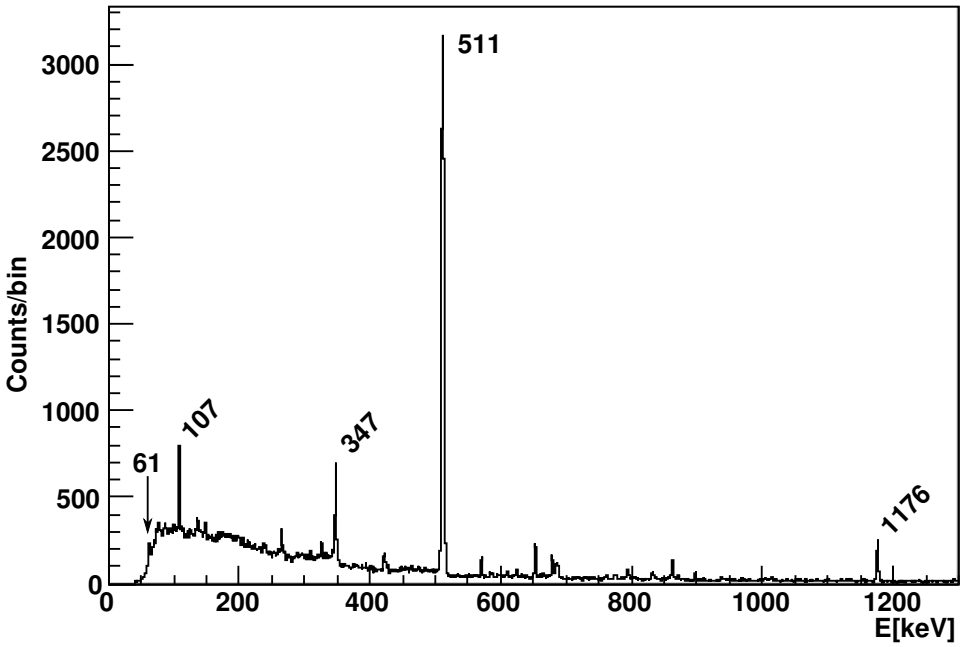

Figure 4.10: γ spectrum, gated on ^{98}Cd decay.

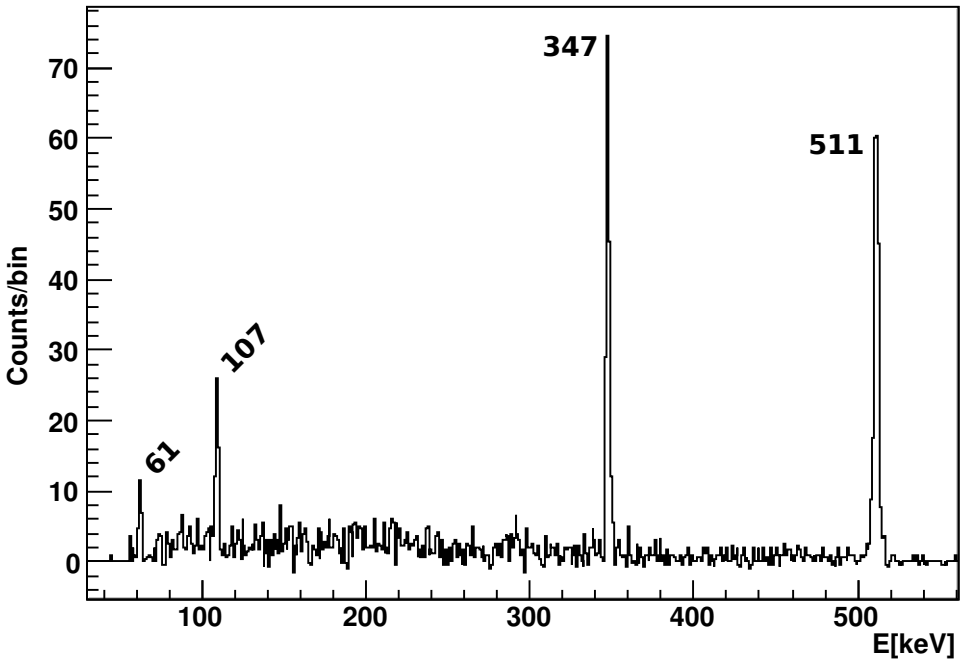

Figure 4.11: γ spectrum, gated on ^{98}Cd decay and 1176 keV γ coincidence.

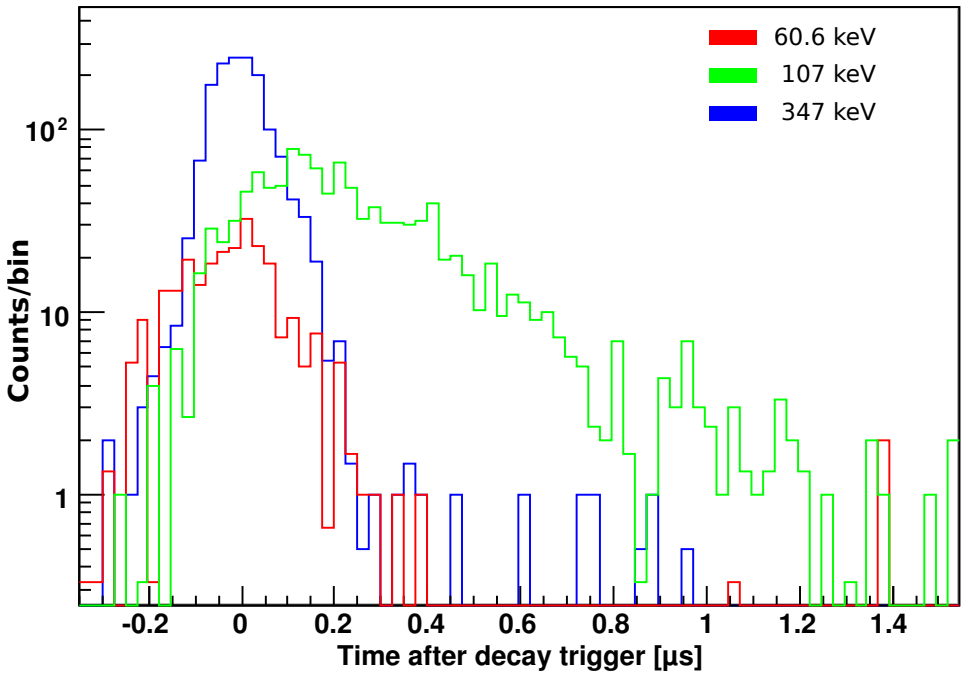

Figure 4.12: Time distributions for the three low-lying transitions in ^{98}Ag.

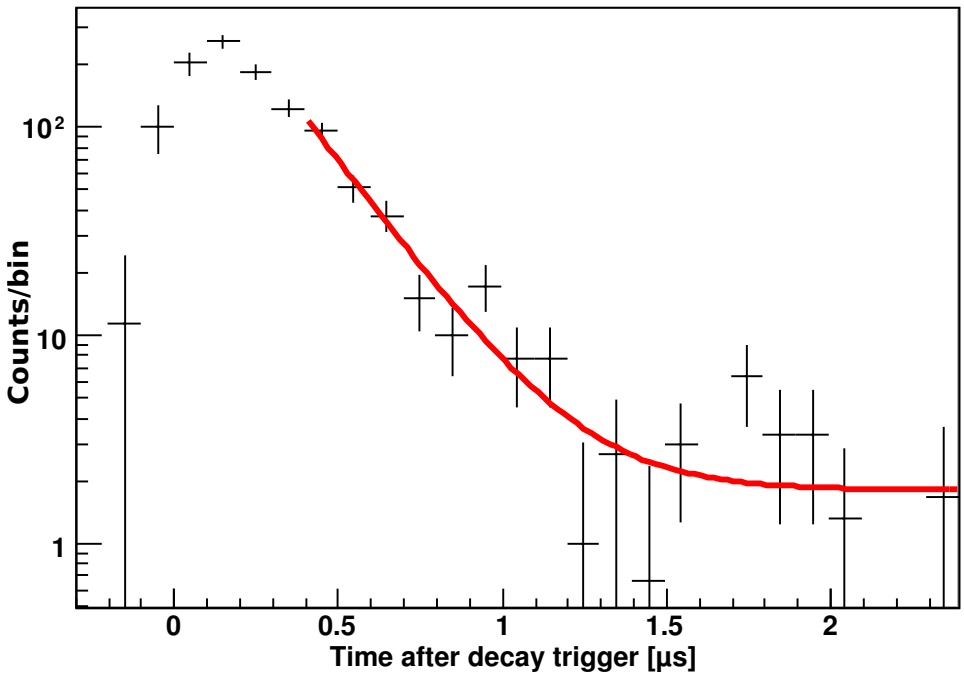

Figure 4.13: Exponential decay fit (plus constant background) used to determine the lifetime of the 107 keV transition in ^{98}Ag.

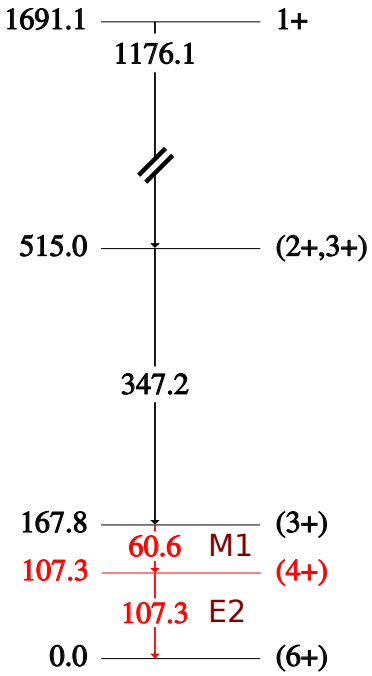

Figure 4.14: Level scheme of ^{98}Ag, proposed to explain the results of the present experiment.

The result is clearly incompatible with the level scheme in fig. 4.9. In that level scheme, the 107 keV transition feeds the first excited state, which then decays via the 60.6 keV transition to the ground state. Thus, every 107 keV transition should be followed by a 60.6 keV transition, and the lifetime of the 60.6 keV transition should be at least as long as that of the 107 keV transition. (The fact that both transitions take place partially via conversion electrons does not matter for the argument.)

The authors of [30] give good arguments for their determination of the multipole character of the transitions, which I will therefore assume to be correct. Thus, the level scheme shown in fig. 4.14 is proposed, which is compatible with the new lifetime result, but keeps the multipolarity of the transitions from [30].

We can also calculate the absolute transition strength of the 107 keV transition. Using our value for the half-life and a conversion coefficient $\alpha = 1.124(16)$ from [29], we obtain

$$B(E2; 4^+ \rightarrow 6^+) = 132(12)e^2\mathrm{fm}^2 = 4.91(45)\mathrm{W.u.}$$

4.3.3 Implantation of ^{98}Ag

As can be seen from the particle identification plot (fig. 4.1), ^{98}Ag is directly produced by the FRS as well. The measured lifetime of the 107 keV state would lead us to expect that at least a few of the nuclei arrive at the stopper in this excited state.

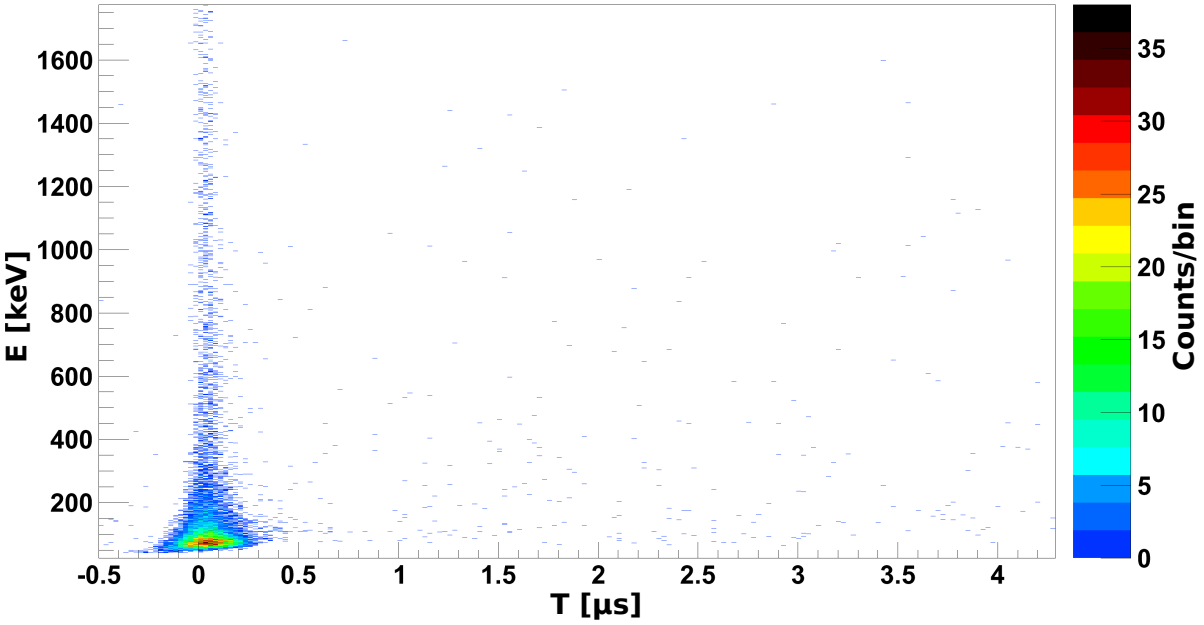

Figure 4.15: Histogram showing γ rays observed vs. time after implantation (gate on ^{98}Ag particle id).

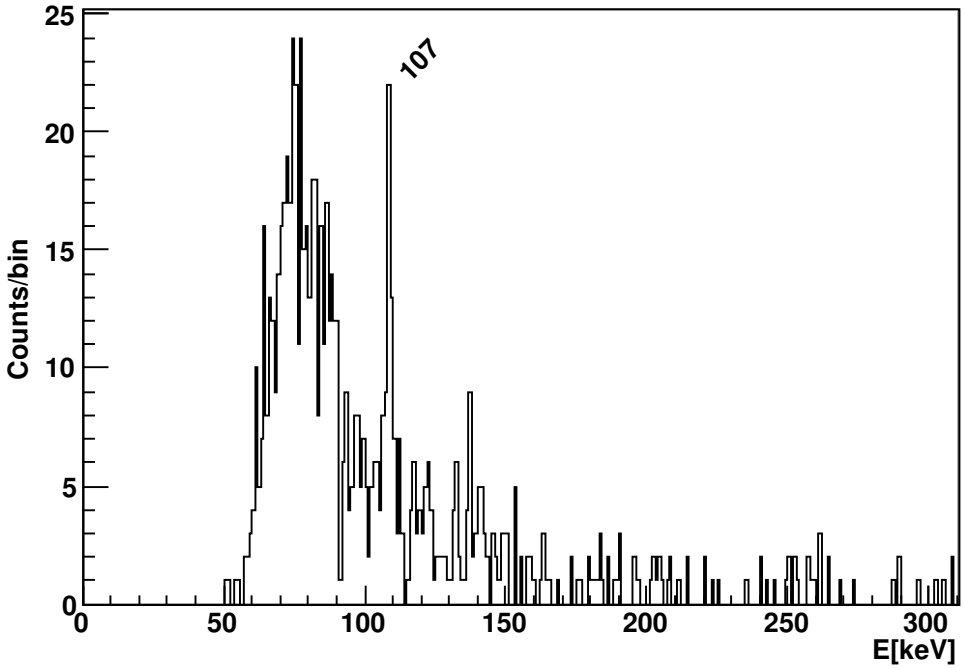

Figure 4.16: Sum spectrum for ^{98}Ag implantation (projection of fig. 4.15 on energy axis, region outside the flash).

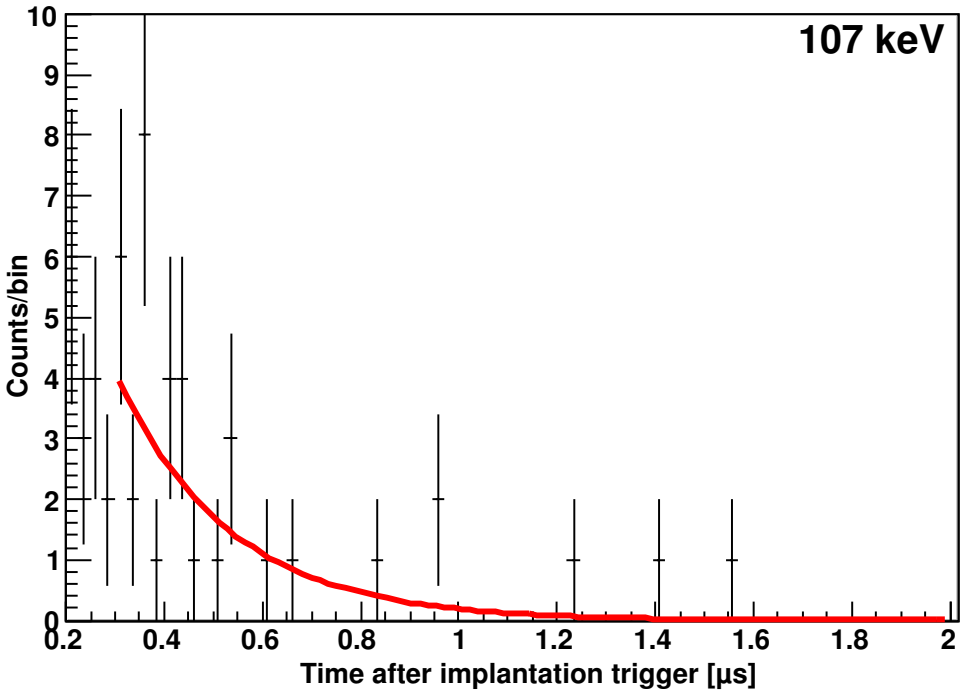

Figure 4.17: Exponential decay fit used to determine the lifetime of the 107 keV transition in ^{98}Ag implantation.

In fig. 4.15, a histogram showing γ energies vs. time after implantation is shown. Just as for ^{98}Cd (ref. fig. 4.2), the most prominent feature is the prompt flash. Projecting the region outside the flash onto the energy axis, the 107 keV transition can indeed be seen (fig. 4.16).

Using the implantation data to determine the lifetime of the 107 keV transition is challenging due to the fact that the width of the prompt flash is comparable to the lifetime. Substracting this background is hard due to the low statistics.

In fig. 4.17, an exponential decay was fitted in a region that lies mostly outside the flash. The fit gives a lifetime of

$$t_{1/2} = 0.158(26)\ \mu\text{s}$$

where the error given is purely the statistical (fitting) error. The systematic error from effects of the flash is expected to be substantial, in addition, the fit result was found to be highly dependant on the exact region used for the fit. Nevertheless, the result agrees with the decay result within the statistical error.

5 Discussion of results

5.1 Theoretical description of atomic nuclei

The atomic nucleus is a quantum-mechanical system consisting of a large, but not huge, number of constituents (nucleons). Such systems, sometimes called *few-body systems*, are known for being notoriously hard to handle theoretically: they are well beyond the abilities of methods that consider each constituent separately, while not being large enough to be generally suitable for a statistical approach.

We will illustrate these difficulties with a rough sketch of a numerical technique for the solution of quantum systems. Let us start with a single particle: its (stationary) Schrödinger equation is

$$H\psi = E\psi \tag{5.1}$$

with an unknown wave function ψ. One approach of numerically solving this equation is to start with an ansatz where the wave function is assumed to be of the form

$$\psi = \sum_i a_i \phi_i \tag{5.2}$$

with a suitably chosen, finite set of model states ϕ_i. This turns the infinite-dimensional Schrödinger equation into a finite-dimensional equation, where H is now a finite-dimensional matrix. Solving this equation means determining the eigenvectors and eigenstates of H, which can be done via a variety of well-understood (and reasonably fast) numerical methods.

We now assume that the set $\{\phi_i\}$ is a truncation of an infinite set that forms a basis of the Hilbert space. This means that, as we make the set $\{\phi_i\}$ larger and larger, equation 5.2 eventually approximates any wave function ψ arbitrarily well. But then, the eigenvectors and eigenstates of the finite dimensional equation will converge to the solution of the original equation 5.1, allowing us to solve it as accurately as we are willing to invest computational effort.

Let us now expand this scheme to many-particle systems. Let the single-particle states be a linear combination of some set $\{\alpha_i\}$. The set $\{\phi_i\}$ is formed by all possible (totally symmetric or totally antisymmetric, depending on the kind of particles described) combinations of the $\{\alpha_i\}$. The problem is that the size of $\{\phi_i\}$ now grows combinatorically with the number of particles involved and the size of $\{\alpha_i\}$. Of course, as the size of $\{\phi_i\}$ is the dimension of our matrix H, the numerical effort to determine its eigenvectors and eigenvalues becomes prohibitive very soon.

Modern computers allow performing calculations using a similar scheme, called the *no-core shell model*, on nuclei with ~ 10 nucleons. The combinatorical growth described thus makes it clear that such calculations for nuclei with ~ 100 nucleons, which form the focus of interest for this work, are infeasible now and in the forseeable future.

Of course, the problem has been the subject of a large body of research, and methods that attempt to deal with these difficulties have been developed. However, the main point still stands: the few-body problem in quantum mechanics is extremely challenging. This is perhaps best demonstrated by chemistry: medium-sized molecules have ~ 100 electrons. Despite being the driving force behind a multibillion dollar industry, chemistry is still based a lot on trial and error.

In a way, the situation in nuclear physics is even worse than in chemistry: at least, the interaction between two electrons is very well understood. In nuclear physics, the interaction between two nucleons arises from the interaction of its constituents, the quarks. The behaviour of quarks (quantum chromodynamics) is reasonably well understood on small length scales, but not on length scales of the order of the size of the nucleon. Thus, calling the above-mentioned no-core shell model calculations *ab initio* is not, strictly speaking, correct, because they still rely on an empirically parameterized nucleon-nucleon interaction. A true *ab initio* calculation would have to start at length scales well below the size of a nucleon, where the behaviour of quarks is well understood, and then simulate the nucleus as a system of quarks, using methods like lattice gauge theory. This approach is currently infeasible for even the smallest nuclei.

Given these formidable difficulties, it is perhaps not surprising that nuclear theory relies a lot on empirical *models*, rather than exact *theories*. A model of particular interest is the *shell model*, which will be discussed next.

5.2 The nuclear shell model

Our discussion of the nuclear shell model follows [31]. We start with the Hamiltonian

$$H = \sum t_i + \sum V_{ij} \tag{5.3}$$

where the index i runs over all nucleons, t_i is the kinetic energy of nucleon i, and V_{ij} is the interaction potential between nucleon i and nucleon j.

The kinetic energy of the nucleons is of the order of 25 MeV [32], whereas the mass of the nucleon is of the order of 938 MeV/c^2. Therefore, the non-relativistic description from above appears justified.

We can rewrite the Hamiltonian from above as

$$\begin{aligned} H &= H_0 + H_{\text{res}} \text{ , where} \\ H_0 &= \sum_i (t_i + U_i) \\ H_{\text{res}} &= \frac{1}{2} \sum_{ij} V_{ij} - \sum_i U_i \end{aligned} \tag{5.4}$$

where U_i is the energy of nucleon i in some potential. So far, this is an exact transformation, i.e. every problem that can be written in form of equation (5.3) can also be written in form of equation (5.4), regardless of how U_i is chosen. However, the hope is now that, by a suitable choice of U_i, we can make H_0 large and H_{res} small, so that the problem essentially becomes one of independent nucleons moving in a potential, with a small pertubation coming from the nucleon-nucleon interaction.

This situation is similar to atomic physics, where interacting electrons move in a potential generated by the central nucleus. In nuclear physics, however, the potential U_i is non-physical: there is no attractive "core" around which the nucleons move. Instead, each nucleon moves in a potential generated by the other nucleons.

From an experimental point of view, equation (5.3) is motivated by the fact that the mean free path for nucleons inside the nucleus is large compared to the nuclear radius [32].

5.2.1 Shell structure of atomic nuclei

A large body of experimental evidence, such as neutron separation energies or energies of the first excited state, suggests that atomic nuclei have *shell structure*. This is somewhat like the existence of noble gases in atomic physics: for certain numbers of nucleons, called the *magic numbers*, nuclei are unusually stable (against separation of a nucleon, or against excitation). However, unlike in atomic physics, there are two kinds of nucleons (protons and neutrons) that are considered independently. Therefore, we have nuclei which are magic with respect to their proton number, magic with respect to their neutron number, and nuclei with are magic with respect to both, the so-called *doubly-magic nuclei*.

To discuss these magic numbers theoretically, we make a dramatic simplification of equation (5.4) and let $H_{\text{res}} = 0$. We are then left with

$$H = \sum_i (t_i + U_i) \tag{5.5}$$

i.e. the motion of particles in a central potential. In this approach, we will simply assume a form for U_i; a commonly used empirical form would be the *Woods-Saxon* potential. We are going to use something even simpler, the spherical harmonic oscillator potential

$$U(r) = \frac{1}{2} m\omega^2 r^2 \tag{5.6}$$

where m is the nucleon mass and ω is a single empirical parameter. Equations 5.5 with 5.6 turn out to have an analytical solution, with energies given by

$$E_N = \hbar\omega \left(N + \frac{3}{2} \right) \tag{5.7}$$

where $N = 0, 1, 2, \ldots$ is the *major oscillator quantum number*. As usual in spherically symmetric problems, the N states are degenerate multiplets characterized by an

orbital quantum number $L = N, N-2, \ldots, 1$ or 0 and a *magnetic quantum number* $m = -l, \ldots, l$. Each (N, L) multiplet thus has $2L+1$ m-substates; the fact that the nucleons have an intrinsic spin of $1/2$ doubles that to $2(2L+1)$. The $N = 0, 1, 2, 3, 4 \ldots$ multiplets thus have $2, 6, 12, 20, 30, \ldots$ substates. Identifying the N-multiplets with the shells thus yields magic numbers of $2, 8, 20, 40, 70$, in disagreement with experiment.

To fix this problem, one assumes an interaction between the intrinsic spin of the nucleons and the orbital angular momentum (*spin-orbit coupling*). The details were originally worked out by Maria Goeppert-Mayer and J. Hans D. Jensen et al. in 1949 and 1950 ([33], [34], [35]), for which they shared the Nobel Prize in 1963.

The spin-orbit coupling couples the states in an $L > 0$ multiplet with the intrinsic spin $1/2$ of the nucleon to a $J = L - 1/2$ and a $J = L + 1/2$ multiplet. (For $L = 0$, we only get $J = 1/2$.) Adding a spin-orbit term to the Hamiltonian breaks the degeneracy between the two J-multiplets. In practice, one also adds a L^2 term to break the degeneracy between L multiplets with the same major oscillator quantum number.

It is common to define the *radial quantum number*

$$n = (N - L + 2)/2 \tag{5.8}$$

Furthermore, as in atomic physics, we use letters s, p, d, f, g, h, ...to denote $L = 0, 1, 2, 3, 4, 5, \ldots$. The radial quantum number n is written in front of it and the spin-orbit quantum number J behind it. Thus, for example, a $3p_{3/2}$ multiplet would have $n = 3$, $L = 1$ and $J = 3/2$.

In fig. 5.1, the result is depicted graphically. In the first column, the spherical harmonic oscillator states are shown, labeled with the major oscillator quantum number N. Next, an L^2 term is added to the Hamiltonian, causing the formerly degenerate L substates to split (second column). Finally, the spin-orbit coupling splits every L substate with $L > 0$ into two substates with $J = L + 1/2$ and $J = L - 1/2$ (third column).

Each of these substates is again a multiplet with $2J + 1$ (degenerate) magnetic substates, giving rise to the occupation numbers shown in the figure. Adding them up, we can indeed reproduce the experimentally observed magic numbers 2, 8, 20, 28, 40, 50, 82 and 126.

5.2.2 Surface delta interaction

So far, our model has been able to explain the shell structure of (spherical) atomic nuclei. However, if we want to go further and consider, for example, excited states, we have to come back to considering interaction between nucleons, and thus, to the computational complexity mentioned in the introduction.

The shell structure, however, suggests a way to radically decrease the number of contituent particles that need to be considered. We postulate that the dynamics of the nucleus essentially happens in the last shell that is not completely filled (the *valence nucleons*), while the shells below it form an *inert core*.

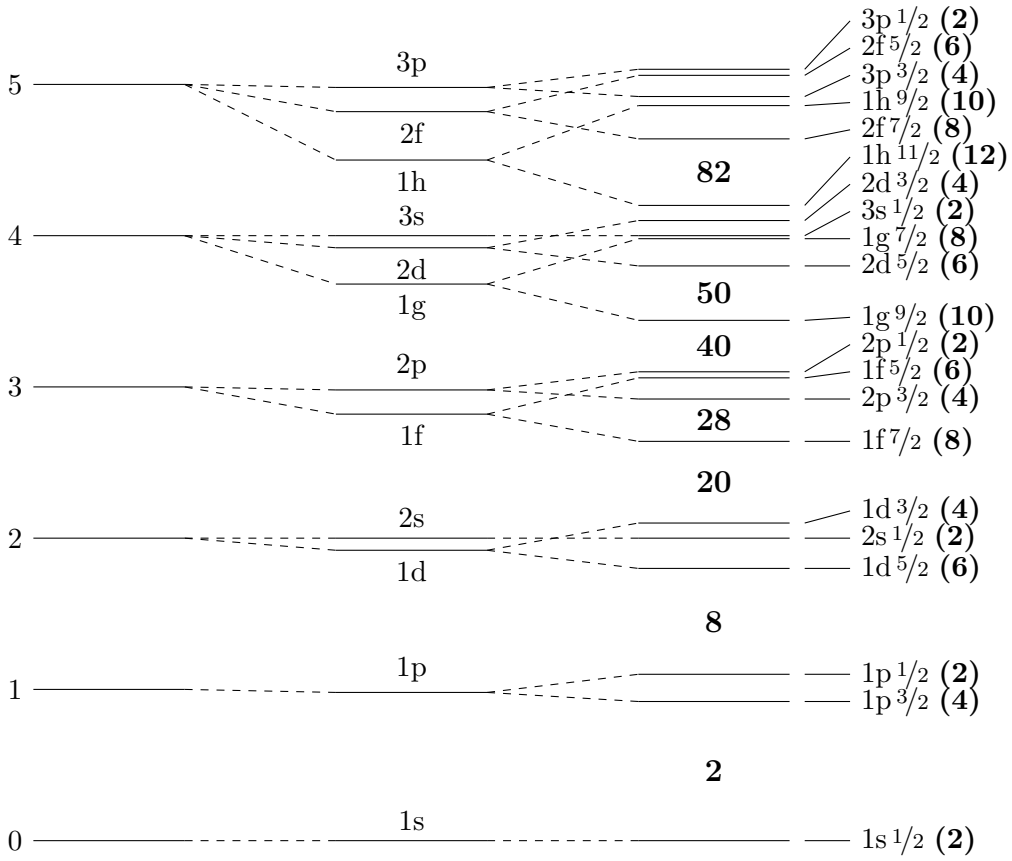

Figure 5.1: Single particle states in the shell model (see text for explanation). Figure redrawn from [36].

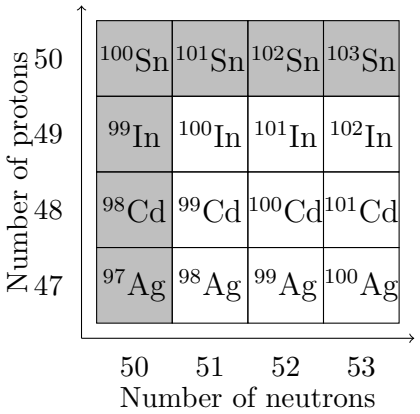

Figure 5.2: Neighborhood of the doubly-magic nucleus ^{100}Sn.

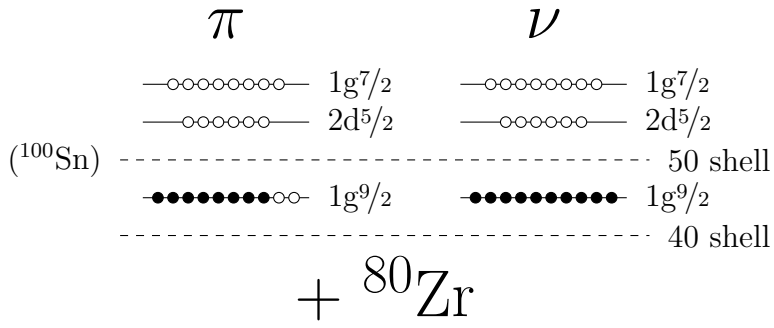

Figure 5.3: ^{98}Cd in the shell model: two proton holes and a ^{100}Sn core.

For nuclei that are only a few nucleons beyond being doubly-magic, this approach reduces the number of particles to something manageable. For nuclei that are a few nucleons short of being doubly-magic, we can consider the *holes* in the last shell as our particles, and again deal only with a manageable number of them.

Let us discuss this for our primary nucleus of interest, ^{98}Cd, which has $N = 50$ neutrons and $Z = 48$ protons. The doubly-magic tin isotope ^{100}Sn with 50 protons and 50 neutrons serves as our inert core. In this model, ^{98}Cd consists of two proton-holes in the $1g_{9/2}$ shell (fig. 5.3). From standard angular momentum coupling rules, we know that these can couple to spins of 0, 2, 4, 6 and 8.

States with higher spin require lifting an additional proton or neutron across the shell gap to create an additional nucleon/hole pair. This simple picture explains the qualitiative structure of the yrast band of ^{98}Cd quite well: we have rather low-lying J = 0, 2, 4, 6 and 8 states, then a large gap, and above it the J = 10, 12, ... states.

We will now try to make these arguments quantitative. For the J = 0, 2, 4, 6, 8 states, we are essentially considering the dynamics of the two proton holes. We are most interested in the energy difference between these states, as this is what we observe experimentally when we excite the nucleus and it de-excites again. For the interaction between the two holes, we assume a very simple potential

$$V(r_1, r_2) = \delta(r_1 - r_2)\delta(|r_1| - R) \tag{5.9}$$

where R is the nuclear radius. This *surface delta interaction* is active only when the particles are both at the same position on the nuclear surface.

From a theoretical perspective, the surface delta interaction is an attractive choice because it allows an analytical calculation of the energy differences [31]. We get

$$\Delta E_{j^2,J} = \frac{F_0}{2}(2j+1)^2 \begin{pmatrix} j & j & J \\ 1/2 & -1/2 & 0 \end{pmatrix} \tag{5.10}$$

This expression still contains the unknown factor F_0. In order to arrive at predictions which we can compare to experiment, we will express energies in units of the difference

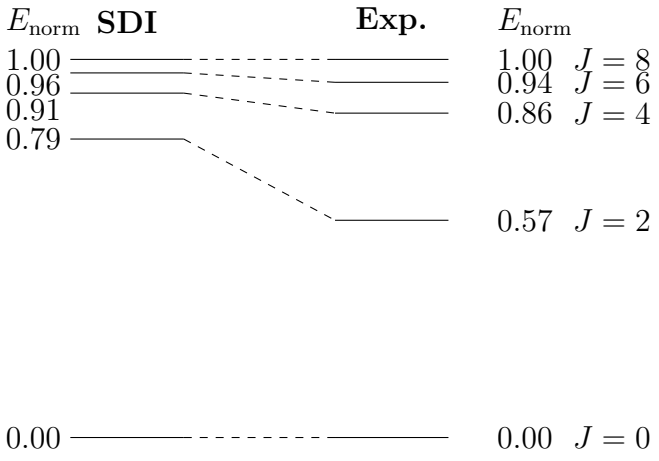

Figure 5.4: Surface delta interaction for ^{98}Cd: comparison between theory and experiment (energies normalized to $J = 8$ state).

between the $J = 8$ and the $J = 0$ state (i.e. we let $E_0 = 0$ and $E_8 = 1$). F_0 then cancels out.

Fig. 5.4 shows a comparison between the experimentally observed levels and the results of our model calculation. As expected for such a simple model, the agreement is rather poor, but at least the general structure (decreasing distance between states) is reproduced.

In order to try to improve the agreement between experiment and theory, and to describe the higher-lying states as well, we turn to full-blown shell model calculations. The change is twofold: first, we extend our *model space*, that is, in addition to the two proton holes (for ^{98}Cd), we consider additional nucleon particle-hole pairs. As mentioned above, such additional pairs are clearly needed to describe the states above the $J = 8$ state. However, they also have an effect on the lower states. Quantum mechanically, the physical states are written as a combination of the possible model states (compare equation 5.2). We expect that the major contribution to the $J = 0, 2, 4, 6, 8$ states will come from the two proton holes, but other model states (such as three holes plus a nucleon coupled to the respective J) will also play a minor role. Thus, the description of the lower states can also be expected to improve as the model space is made larger.

The second change is, obviously, to replace the rather schematic surface delta interaction with something more realistic. Naively, one might expect that the interaction between the valence nucleons is the same as that between free nucleons (which is accessible through lattice QCD or particle physics experiments). Unfortunately, this is not correct; the effect of the "inert" core is not merely to provide a central potential in with the valence nucleons move. Instead, it also changes the interaction between the valence nucleons from the free interaction to an *effective* interaction.

Calculating this effective interaction from the bare nucleon-nucleon interaction is es-

sentially equivalent to the no-core calculation, i.e. numerically intractable for moderately-sized nuclei. There are various approaches that try to calculate effective interactions from nucleon-nucleon scattering potentials (the "realistic" interactions). In other cases, the parameters of the interaction are fitted to best describe the data (the "empirical" interactions).

5.3 Shell model calculations for ^{98}Cd

Fig. 5.5 shows shell model predictions from the time before the experiment took place. At that time, the J = 0, 2, 4, 6, 8, 12 states were known, but the J = 10 state had not yet been discovered.

As we have discussed in section 4.2, the most likely interpretation of our experimental results is a (10^+) state directly below the (12^+) state. Both shell model calculations place the (10^+) state above the (12^+) state. In that case, however, the (10^+) state would decay to the (12^+) and the new transition at 4158 keV would not be observed. The (14^+) state in the column labeled GDS (large-scale shell model with GDS interaction) could only decay to the (8^+) via an E6 transition, so it cannot be used to explain the experimental results either. Thus, we need to consider whether theory can be modified as to correctly place the (10^+) state below the (12^+) state.

Based on our publication of preliminary experimental results, two ideas for such a modification have been proposed (fig. 5.6). The first idea [38] proposes a reversal of the $\nu d_{5/2}$ and $\nu g_{7/2}$ single particle states. The (12^+) state corresponds largely to a neutron lifted from the $\nu g_{9/2}$ shell to the $\nu d_{5/2}$ shell (ref. fig. 5.3), or, put differently, the dominant component is $\nu g_{9/2}^{-1} \nu d_{5/2}$. For the (10^+) state, the dominant component is $\nu g_{9/2}^{-1} \nu g_{7/2}$. Thus, a reversal of the energies of the $\nu d_{5/2}$ and the $\nu g_{7/2}$ single particle orbital could be expected to have the desired effect of bringing the (10^+) state below the (12^+) state.

The calculation presented in [38] and performed by A. Blazhev (fig. 5.6, column 3nph) makes use of the NuShell@MSU shell model code [39]. The model space

$$\pi\nu(f_{5/2}, p_{3/2}, p_{1/2}, g_{9/2}, g_{7/2}, d_{5/2}, s_{1/2}) + \nu(h_{11/2})$$

was truncated to allow $\pi(p_{1/2}, g_{9/2})^{10}$ and up to 3 neutron particle-hole $\nu g_{9/2}$ to $\nu d_{5/2}, g_{7/2}$ excitations. In the calculation, the $\nu d_{5/2}$ single particle orbital was 50 keV above the $\nu g_{7/2}$ single particle orbital, i.e. reversed with respect to the normal ordering. As shown in fig. 5.6, the calculation correctly reproduces the (10^+) state slightly below the (12^+) state, as well as the small energy difference between them. However, their absolute energies are too high, so further tuning is clearly needed.

A second idea [38] was explored in a calculation by H. Grawe (fig. 5.6, column pgdg). This calculation uses the m-scheme code OXBASH [40] and a

$$\pi\nu(f_{5/2}, p_{3/2}, p_{1/2}, g_{9/2}, g_{7/2}, d_{5/2}, s_{1/2})$$

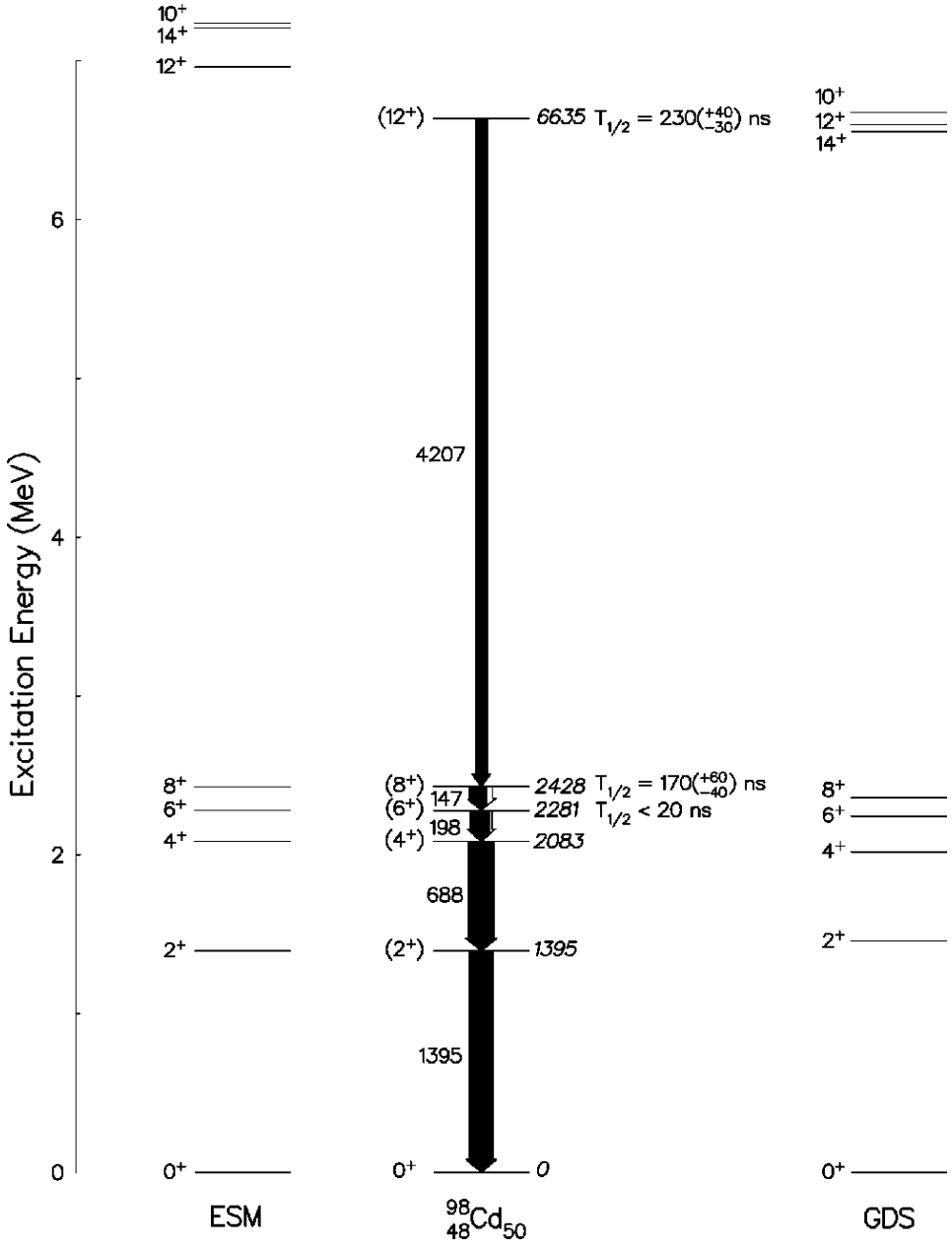

Figure 5.5: Two different shell model calculations of ^{98}Cd, made before the experimental discovery of the (10^+) state (from [37]).

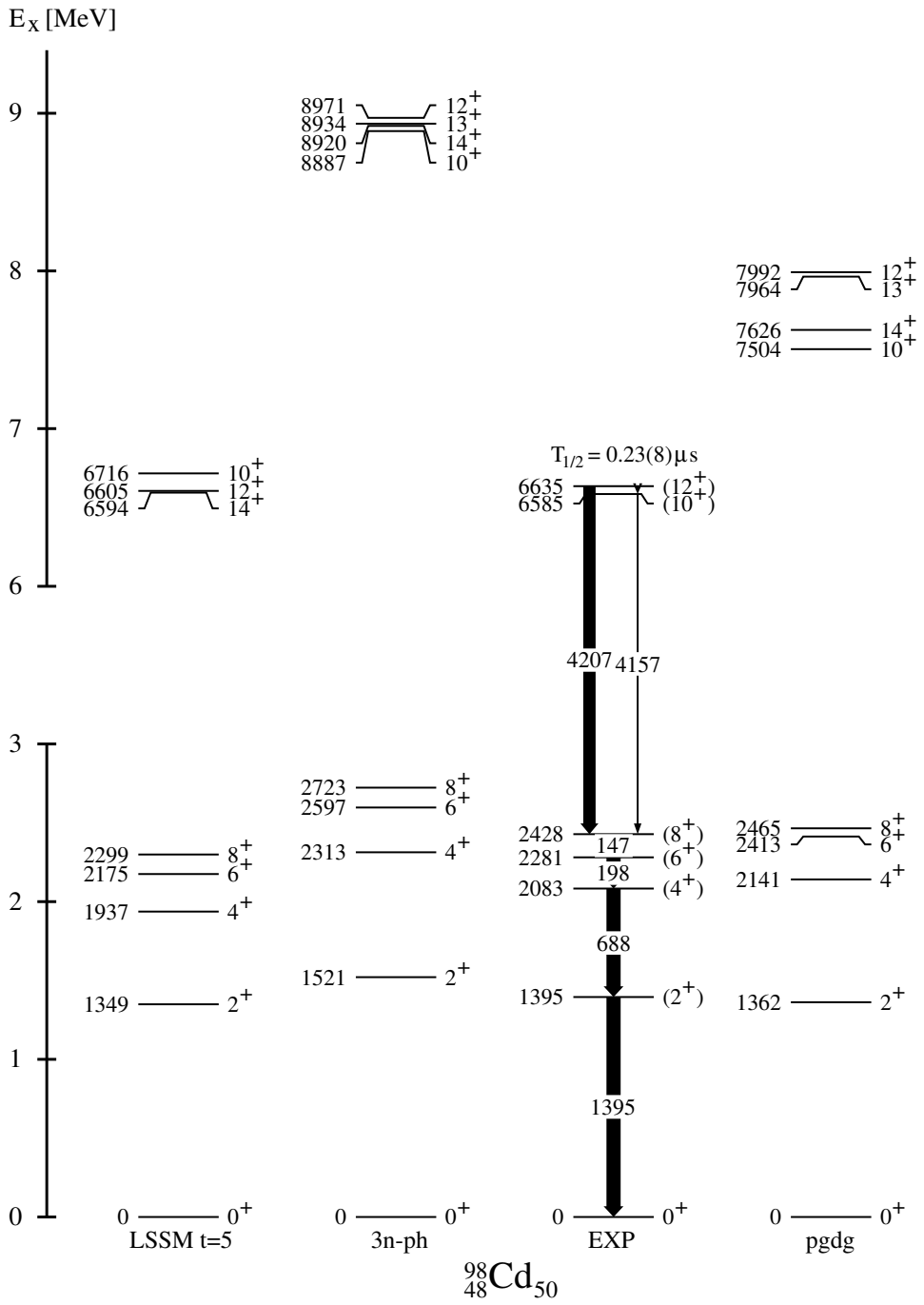

Figure 5.6: Three shell model calculations compared to experimental results (column EXP). The 3n-ph and the pgdg calculations, performed after the experiment, reproduce the correct level ordering (from [38]).

model space, truncated to excitations in $\pi(\mathrm{p}1/2, \mathrm{g}9/2)$ and 1p1h excitations in $\pi\mathrm{g}9/2^{-1}\pi\mathrm{d}5/2, \mathrm{g}7/2$ and $\nu\mathrm{g}9/2^{-1}\nu\mathrm{d}5/2, \mathrm{g}7/2$ across the $Z, N = 50$ shell gaps. The calculation assumes a normal ordering of the νd5/2 and the νg7/2 single particle orbitals, but tunes the proton-proton monopole part of the interaction to reproduce experimentally observed proton separation energies in ^{88}Sr, ^{90}Zr and ^{100}Sn. Again, this can reproduce the ordering of the (10^+) and (12^+) state, but their relative distance is a lot larger than what is observed in the experiment.

It is also illuminating to compare the situation in ^{98}Cd to that in ^{54}Fe. Both nuclei can be described as two proton holes in a doubly-magic, $N = Z$ core (^{100}Sn or ^{56}Ni); ^{98}Cd is one major shell higher. Fig. 5.7 shows the single particle energies in ^{56}Ni and ^{100}Sn. In fig. 5.8, the situations in ^{54}Fe and ^{98}Cd are compared. Note how the core-excited states are similar. Also, the competition between a low-energy E2 and a high-energy E4 transition crossing the shell gap is the same.

In conclusion, the new level in ^{98}Cd shows that there are still subtle effects in the structure around ^{100}Sn that are not understood. Although most of the other nuclei in the region around ^{100}Sn are well described, the core-excited states in ^{98}Cd still present a challenge to theory. The resulting improvement of the two-body matrix elements (TMBEs) and single-particle energies (SPEs) will make shell model predicitions for yet unobserved nuclear states more reliable, which may also be of importance for nuclear astrophysics.

5.4 Shell model calculations for ^{98}Ag

Fig. 5.9 shows a shell model calculation, performed by A. Blazhev [42], on ^{98}Ag using the SR88MHJM interaction. SR88MHJM [43] is a monopole-tuned variant of the SR88MHJ interaction, which is a realistic interaction derived from a CD-Bonn nucleon-nucleon scattering potential. The calculation used experimental SPEs (single particle energies) from ^{89}Y and ^{89}Sr.

As can be seen in the figure, the calculation reproduces the energies rather well. However, using the standard effective charges $e_\pi = 1.5e$ and $e_\nu = 0.5e$ gives $B(E2) = 1.69$ W.u. for the 107 keV transition, much smaller than the experimental result.

Tuning the effective charges, $e_\pi = 1.72e$ and $e_\nu = 1.44e$ [44] gives $B(E2) = 4.75$ W.u., in good agreement with the experimental result.

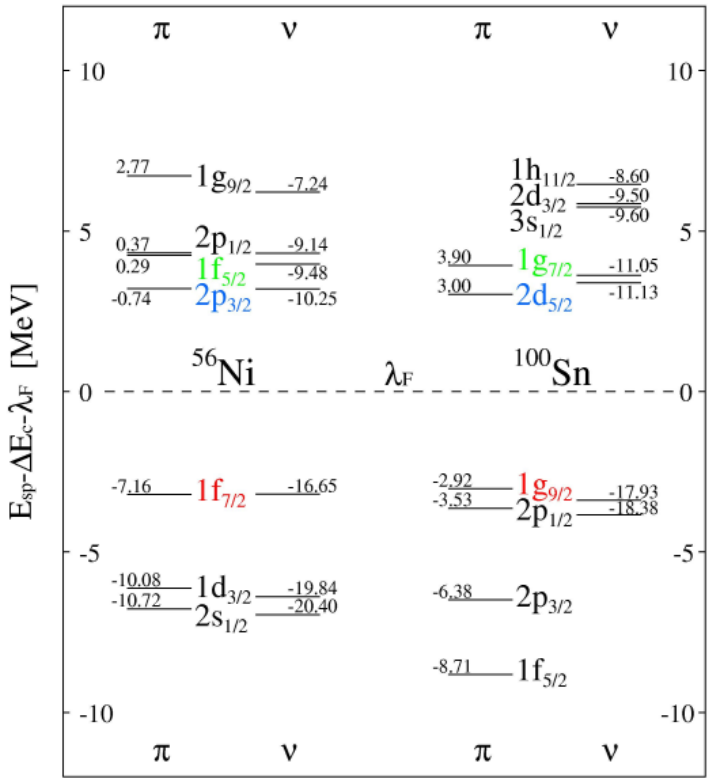

Figure 5.7: Single-particle energies in the doubly-magic, $N = Z$ nuclei ^{56}Ni and ^{100}Sn. From [41].

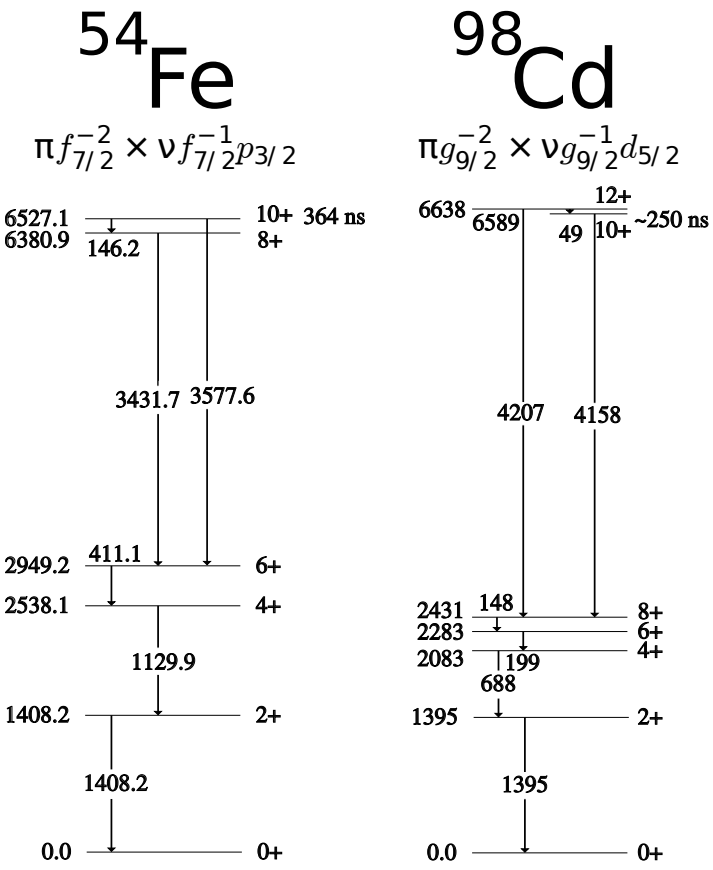

Figure 5.8: Comparison between ^{54}Fe and ^{98}Cd (see text).

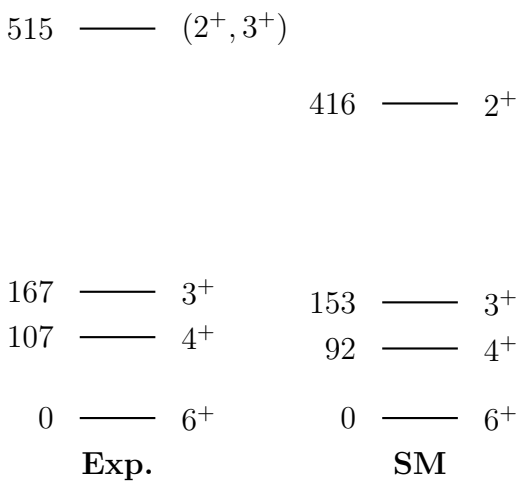

Figure 5.9: Shell model calculation (SM) on ^{98}Ag (from [42]) compared to experiment (Exp.).

6 Conclusion

In this thesis, I have presented new experimental results on the neutron-deficient nuclei ^{98}Cd and ^{98}Ag.

Given the complexity of a modern exotic beam experiment, the first stages of the analysis were necessarily a collaborative effort. For the analysis, we developed a software package, called R2D2. Special attention was paid to make the software reusable, so that further experiments using the GSI RISING or a similar setup can profit from our effort. In particular, the modular structure should make it easy to replace some parts (like the listmode data unpacker) and keep others.

As part of the software development effort, I researched and implemented algorithms to automatically extract calibration coefficients from known calibration histograms. While these still require a certain amount of hand-holding, they have the potential to eliminate a large amount of dull work for future experiments.

Finally, the HDTV project [21], which was started during my Diploma thesis, received further attention. In particular, interoperability with ROOT was improved, and the module for dealing with matrices (2d histograms) received attention. Compared to ROOTs built-in histogram viewer, HDTV was designed with nuclear physics and γ spectroscopy in mind. Therefore, the combination of R2D2, C3PO (or another experiment-specific middle layer), and HDTV is a powerful toolchain for the analysis of exotic-beam experiments.

In ^{98}Cd, a new transition was discovered, pointing to a new excited state with a tentative spin/parity of (10^+). As discussed, existing shell model calculations were incompatible with the experimental observation. The observation has already attracted interest from theory. Two ideas have been proposed [38] to explain the experimental observation: a reversal of the $\nu d^5/_2$ and the $\nu g^7/_2$ single particle orbitals, or an increased proton strength. Right now, the two proposed explanations are tentative, and further work will be required to work out the details and tune the shell model calculations to the point that the experiment can accurately be reproduced.

For ^{98}Ag, the measurement of the lifetime of the lowest transition enabled its $B(E2)$ value to be calculated for the first time. Shell model calculations can reproduce the level energies, while reproducing the $B(E2)$ value allows adjusting the effective nucleon charges e_π and e_ν.

In both cases, once the theoretical studies are finalized, new insights into nuclear structure in the ^{100}Sn region can be expected.

Bibliography

[1] C. B. Hinke et al. Superallowed gamow-teller decay of the doubly magic nucleus ^{100}Sn. *Nature*, 486:341 – 345, 2012.

[2] GSI LINAC department. `http://www-inj.gsi.de/`.

[3] B. Franczak. SIS18 parameter list. `http://www.gsi.de/beschleuniger/sis18/pdf/sis18_parameterliste.pdf`.

[4] Heavy-Ion-Synchrotron SIS18. `http://www.gsi.de/beschleuniger/sis18/sis_e.html`.

[5] F. Hinterberger. *Physik der Teilchenbeschleuniger und Ionenoptik* . Springer, 1997.

[6] H. Geissel et al. The GSI projectile fragment separator (FRS): a versatile magnetic system for relativistic heavy ions . *NIM B*, 70:286 – 297, 1992.

[7] GSI/FRS technical team. Setup of the S2 and S4 areas of the FRS for the S352 experiment. private communication.

[8] O. Klein and T. Nishina. Über die Streuung von Strahlung durch freie Elektronen nach der neuen relativistischen Quantendynamik von Dirac. *Z. Phys. A*, 52(11):853–868, 1929.

[9] Geant 4. `http://geant4.cern.ch/`.

[10] S. Agostinelli et al. Geant4 - a simulation toolkit. *NIM A*, 506(3):250 – 303, 2003.

[11] J. Allison et al. Geant4 developments and applications. *IEEE Trans. Nuclear Science*, 53(1):270 – 278.

[12] D. Bazzacco et al. AGATA technical proposal. `http://www-win.gsi.de/agata/Publications/Agata_pub-proposal.pdf`.

[13] D. Radford. RadWare. `http://radware.phy.ornl.gov/`.

[14] I. Wiedenhöver. *Vollständige Gamma-Spektroskopie des Kerns ^{127}Xe.* PhD thesis, Institut für Kernphysik, Köln, Germany, 1995.

[15] T. Belgya. Spline and polynomial models of the efficiency function for ge gamma-ray detectors in a wide energy range. *Radioanalytical and Nuclear Chemistry*, 265:175–179, 2005.

[16] J. Eberth et al. Development of a composite Ge detector for EUROBALL. *Prog. Part. Nucl. Phys.*, 28(0):495 – 504, 1992.

[17] XIA LLC. XIA DGF-4C. `http://www.xia.com/DGF-4C.html`.

[18] S. Pietri et al. Recent results in fragmentation isomer spectroscopy with RISING. *NIM B*, 261:1079 – 1083, 2007.

[19] The ROOT data analysis framework. `http://root.cern.ch/`.

[20] mesytec GmbH & Co. KG. MPR-16-LOG manual. `http://www.mesytec.com/datasheets/MPR16_LOG.pdf`.

[21] N. Braun, T. Kotthaus, and R. Schulze. HDTV - Nuclear Spectrum Analysis Tool. `http://www.ikp.uni-koeln.de/projects/hdtv/`.

[22] N. Braun. Study of collectivity in ^{88}Zr with the Horus spectrometer, 2008. Diploma thesis, Institut für Kernphysik, Köln, Germany.

[23] J. Theuerkauf, S. Esser, S. Krink, M. Luig, N. Nicolay, O. Stuch, and H. Wolters. Program tv. Institute for Nuclear Physics, Cologne.

[24] National Nuclear Data Center. `http://www.nndc.bnl.gov/`.

[25] T. Faestermann, Physik-Department E12, Technische Universität München. Calibration of silicon detectors via Compton scattering. private communication.

[26] H. Morinaga and T. Yamazaki. *In-beam gamma-ray spectroscopy*. North-Holland, 1976.

[27] M. Górska et al. $^{98}_{48}$Cd$_{50}$: The two-proton-hole spectrum in $^{100}_{50}$Sn$_{50}$. *PRL*, 79:2415 – 2418, 1997.

[28] A. A. Blazhev. *Nuclear structure in the region of the doubly-magic ^{100}Sn*. PhD thesis, University of Sofia, Bulgaria, 2005.

[29] T. Kibédi et al. Evaluation of theoretical conversion coefficients using BrIcc. *NIM A*, 589(2):202 – 229, 2008. `http://bricc.anu.edu.au/`.

[30] A. Płochocki et al. Gamow-Teller beta decay of the very neutron-deficient N=50 nuclide ^{98}Cd. *Zeitschrift für Physik A: Hadrons and Nuclei*, 342:43–51, 1992.

[31] Kris L. G. Heyde. *The Nuclear Shell Model*. Springer, 1994.

[32] A. Bohr and B. R. Mottelson. *Nuclear Structure*. W. A. Benjamin, 1969.

[33] M. Goeppert-Mayer. On Closed Shells in Nuclei. II. *Phys. Rev.*, 75:1969–1970, 1949.

[34] M. Goeppert-Mayer. Nuclear Configurations in the Spin-Orbit Coupling Model. II. Theoretical Considerations. *Phys. Rev.*, 78:22–23, 1950.

[35] Otto Haxel, J. Hans D. Jensen, and Hans E. Suess. On the "Magic Numbers" in Nuclear Structure. *Phys. Rev.*, 75:1766–1766, 1949.

[36] J. Jolie. *Nuclear Structure Physics*. unpublished.

[37] A. Blazhev et al. Observation of a core-excited e4 isomer in ^{98}Cd. *Phys. Rev. C*, 69:064304, 2004.

[38] A. Blazhev et al. High-energy excited states in ^{98}Cd. *JoP: Conf. Ser.*, 205(1):012035, 2010.

[39] B. A. Brown and W. D. M. Rae. *MSU-NSCL report*, 2007.

[40] B. A. Brown et al. *MSU-NSCL report*, (1289), 2004.

[41] H. Grawe and M. Lewitowicz. Shell structure of nuclei far from stability. *Nucl. Phys. A*, 693:116 – 132, 2001.

[42] A. Blazhev. Shell model calculation for ^{98}Ag. private communication.

[43] H. Grawe. The SR88MHJM interaction. private communication.

[44] D. Rudolph et al. Multiparticle-hole states of high spin in $N < 50$, $A \approx 90$ nuclei: 4. Systematics of level energies and electromagnetic properties. *Nucl. Phys. A*, 597:298 – 326, 1996.

List of Figures

Acknowledgement - Danksagung

Diese Arbeit wäre ohne die vielen Menschen, die mich unterstützt haben, nicht möglich gewesen. Ihnen allen gilt mein Dank. Insbesondere bedanke ich mich bei:

- Prof. Dr. Jan Jolie für die Vergabe des Themas,
- Dr. Andrey Blazhev für die Betreuung der Arbeit und der damit verbundenen Experimente,
- der Deutsche Telekom Stiftung die für finanzielle und nicht-finanzielle Unterstützung,
- der *Bonn-Cologne Graduate School* (BCGS) für die finanzielle und nicht-finanzielle Unterstützung,
- den Mitgliedern der Prüfungskommission, Prof. Dr. A. Schadschneider, Prof. Dr. J. Jolie, Prof. Dr. P. Reiter und Dr. S. Heinze, für ihre Zeit,
- Dr. Tanja Kotthaus, Dr. Désirée Radeck und Dr. Reinhold Braun für das Korrekturlesen der Arbeit,
- den Mitgliedern der S352-Kollaboration für die gute Zusammenarbeit während und nach dem Experiment,
- dem Team an der Gesellschaft für Schwerionenforschung (GSI) für die Unterstützung,
- meinen Kollegen am Institut für Kernphysik in Köln für die angenehme Arbeitsatmosphäre.

Nicht zuletzt gilt mein ganz besonderer Dank meinen Eltern und meiner Partnerin für die Unterstützung während des Studiums und dieser Zeit.

Erklärung

Ich versichere, dass ich die von mir vorgelegte Dissertation selbstständig angefertigt, die benutzten Quellen und Hilfsmittel vollständig angegeben und die Stellen der Arbeit – einschließlich Tabellen, Karten und Abbildungen –, die anderen Werken im Wortlaut oder dem Sinn nach entnommen sind, in jedem Einzelfall als Entlehnung kenntlich gemacht habe; dass diese Dissertation noch keiner anderen Fakultät oder Universität zur Prüfung vorgelegen hat; dass sie – abgesehen von unten angegebenen Teilpublikation – noch nicht veröffentlicht worden ist sowie, dass ich eine solche Veröffentlichung vor Abschluss des Promotionsverfahrens nicht vornehmen werde. Die Bestimmungen dieser Promotionsordnung sind mir bekannt. Die von mir vorgelegte Dissertation ist von Prof. Dr. J. Jolie betreut worden.

Köln, 29.10.2012 Norbert Braun

Teilveröffentlichungen:

A. Blazhev, N. Braun, *et al.*: High-energy excited states in ^{98}Cd. JoP: Conf. Ser. **205** (2010) 012035